University of Zurich[UZH]

# Towards automating avalanche forecasts: A kriging model to interpolate modelled snow instability in the Swiss Alps

GEO 511 Master's Thesis


**Author**
Katia Soland
01-715-622

**Supervised by**
Prof. Dr. Ross Purves
Dr. Frank Techel, SLF (techel@slf.ch)
Günter Schmudlach (schmudlach@gmx.ch)

**Faculty representative**
Prof. Dr. Ross Purves



25.09.2024
Department of Geography, University of Zurich

Department of Geography

**GEO 511 Master's Thesis**

# Towards automating avalanche forecasts: A kriging model to interpolate modelled snow instability in the Swiss Alps

Katia Soland

01-715-622

25 September 2024

Supervisors: Prof. Dr. Ross Purves
Dr. Frank Techel
Günter Schmudlach

# Acknowledgements

I want to express my sincere gratitude to my three supervisors, Prof. Dr. Ross Purves from the University of Zurich (UZH), Dr. Frank Techel from the Swiss Institute for Snow and Avalanche Research (SLF), and Günter Schmudlach from the platform skitourenguru.ch. Without their invaluable support and guidance, this thesis would not have been possible.

I thank Ross and Frank for helping me find a thesis topic that combines my fascination for snow and avalanches with my interest in Geographic Information Systems (GIS) and spatial analysis. Their feedback at every stage of the model building and testing process has been crucial, offering clarity and guiding the direction of further research. I am thankful to Günter for providing me with preprocessed and cleaned backcountry skiing data, without which I would not have been able to test my model. I appreciate that all three of them regularly enquired about how the Master's thesis was going and took the time to answer my questions.

I want to extend my thanks to my fellow students in the master's study room. Their support and camaraderie made a significant difference throughout this journey. They reminded me to take breaks and managed to lift my spirits or take my mind off things during our lunch breaks. Their motivation, understanding, and shared laughter made this process much more enjoyable.

A special thank you goes to my family and my friends outside university. Your words of encouragement and positive energy kept me grounded and focused. I am especially grateful to Nico, who generously dedicated time to proofread my thesis.

# Abstract

The Alps make up more than half of Switzerland's area. Covered in snow, this mountainous terrain is prone to avalanches, endangering people and infrastructure. However, forecasting avalanche danger in Switzerland remains a complex and time-consuming task that is heavily dependent on expert knowledge. To overcome this challenge, new modelling suites have been developed in operational avalanche forecasting in recent years. However, snowpack instability has been neither interpolated nor tested on a larger than regional scale so far.

This two-fold research gap is addressed as follows: The interpolation model developed in this thesis extends the existing modelling suite consisting of SNOWPACK, a physical model which simulates the snowpack at the location of an automated weather station (AWS), and an instability model. Based on a random forest classification, the latter predicts the maximum instability probability (between 0, stable, and 1, unstable) of the snowpack at the location of an AWS. The new interpolation model takes this modelled instability as input to predict the instability probability across a 1 km x 1 km grid covering the Swiss Alps, focusing on human-triggered dry-snow avalanches. The interpolation technique is based on kriging with external drift, incorporating elevation as a secondary variable.

The model was cross-validated and tested with external data. Predictions at the locations of avalanches were used to test high instability probabilities. In contrast, predictions at GPS points from backcountry activities served to test low instability probabilities. Results indicated that the interpolation model effectively captured major snowfall events and varying stabilisation rates according to aspect. It generally predicted high instabilities for avalanches and low instabilities for GPS points. By enhancing the spatial resolution of instability, this work contributes to automating the forecast process. However, some limitations were identified: The model requires sufficient input of automated weather stations (AWSs) for accurate predictions. Additionally, it performs optimally within the elevation range covered by the AWSs. Beyond this range, the model tends to overestimate the instability.

# Contents

# List of Figures

# List of Tables

# List of Abbreviations

**ARPD** Avalanche Risk Property Dataset

**AWS** automated weather station

**AWSs** automated weather stations

**BLUE** best linear unbiased estimate

**DEM** digital elevation model

**GPS** Global Positioning System

**IMIS** Intercantonal Measurement and Information System

***KDE*** kernel density estimation

***KED*** kriging with external drift

***knn*** $k$ nearest neighbours

***LOOCV*** leave-one-out cross-validation

**MeteoSwiss** Federal Office of Meteorology and Climatology

***MSE*** mean squared error

***ME*** mean error

***OK*** ordinary kriging

$\rho_{max}$ maximum instability probability

***RMSE*** root mean squared error

***SA*** slope angle

***SCM*** SAFRAN-Crocus-MEPRA

**SLF** Swiss Institute for Snow and Avalanche Research

**SMN** SwissMetNet

***TI*** terrain indicator

***UK*** universal kriging

# 1 Introduction

## 1.1 Motivation

The Alps make up 58% of the area of Switzerland – the major part compared to the Central Plateau (31%) and the Jura (11%) (Federal Department of Foreign Affairs FDFA, 2023). In winter, the Swiss Alps are an increasingly popular place for sports off the piste, such as snowshoeing, backcountry skiing and snowboarding. In 2020, 6.5% of the Swiss population practised one of these three activities, representing an increase of 2.6% compared to 2014 (Lamprecht et al., 2020). Covered in snow, however, this mountainous terrain is prone to avalanches, endangering people and infrastructure. According to a study by Badoux et al. (2016), in which they compared different natural hazard fatalities, "snow avalanches [...] clearly represent the deadliest natural hazard process in Switzerland" (p. 2764). Since the winter of 1936/37, an average of 24 people per year have died in avalanches in Switzerland (WSL Institute for Snow and Avalanche Research SLF, 2023d). Compared to other natural hazards, the spatial occurrence of avalanches is relatively predictable (WSL Institute for Snow and Avalanche Research SLF, 2023b). Yet, forecasting avalanche danger in Switzerland remains a challenge as it is mainly based on expert knowledge: Avalanche forecasters analyse snow and weather data, study weather predictions and integrate field observations to assess the instability of the snowpack over space and time and decide on an avalanche danger level (Mayer et al., 2023). This traditional method is complex, time-consuming and suffers from subjectivity (Van Herwijnen et al., 2023).
On these grounds, there has been varied research over many years on how to compensate for those drawbacks, e.g. by systematising and automating parts of the approach and increasing the spatial and temporal resolution of avalanche forecasts. In recent years, research has been enriched by more weather data, greater computing power, and machine learning methods (ibid.). New modelling suites have been developed and partly tested in operational avalanche forecasting (ibid.). This master's thesis contributes to automating the forecasting process by enhancing an existing modelling suite. Of the two existing models, the first simulates the snowpack at the location of automated weather stations (Lehning et al., 1999), which the second uses to predict the snow instability (Mayer et al., 2022). Based on the output of the instability model (ibid.), this master's thesis builds a model to interpolate snow instability data and tests it with avalanche observations and GPS tracks of backcountry skiers.

In the following, I will present an overview of the research done so far to systematise and automate the avalanche forecasting process. The focus is set on the models relevant to this thesis.

## 1.2 Research Context and State of the Art

"Avalanche hazard forecasting requires information about the past, current and future state of the snowpack" (Morin et al., 2020, p. 1). While the past and current state are evaluated based on measurements, field observations and snow profiles, the future state is mainly assessed on expert knowledge and experience, i.e. the ability to combine the current state with weather forecasts and snow transformation (ibid.). Since the 1980s, physical snowpack models have been developed to provide avalanche forecasters with information in addition to the meteorological data and field observations. These models simulate the snow stratigraphy and calculate new snow depths (Mayer et al., 2023; Morin et al., 2020). In the following section, the two most detailed and advanced snowpack models, Crocus and SNOWPACK, are discussed (Morin et al., 2020; Van Herwijnen et al., 2023). Simpler models such as SNOWGRID and seNorge will not be described here (Morin et al., 2020).

### 1.2.1 Crocus

Among the first ones to launch a snowpack model was the Centre d'Études de la Neige (CEN), which belongs to the French Meteorological Office (Brun et al., 1989). In the late 1980s, researchers at the CEN developed and tested their model named Crocus (ibid.), which "[...] proved itself sufficient to be considered now as a useful objective tool for operational avalanche forecasting" (p. 333). About ten years later, Crocus was enhanced to a model chain on a regional level: Durand et al. (1999, p. 469) proposed for the different French massifs a "[...] complete automatic system of three numerical models that simulate snow-cover stratigraphy and avalanche risks for operational regional avalanche forecasting." They named the chain after the initial letters of the three models that compose it: SAFRAN-Crocus-MEPRA (*SCM*). The first model, SAFRAN (Système d'Analyse Fournissant des Renseignements Adaptés à la Nivologie), selects the relevant meteorological ground observation data for the snowpack evolution and interpolates the prevailing conditions at different elevations (600-3600 m, etc.; by steps of 300 m), slope angles (flat, 20° and 40°) and slope aspects (N, E, SE, S, SW, S) (Durand et al., 1999). The parameters calculated by SAFRAN are fed to Crocus, a physical snowpack model that simulates the snowpack and its evolution. The last model in the chain, MEPRA (Modèle Expert d'Aide à la Prévision du Risque d'Avalanche), is an expert system that predicts the mechanical stability of the snowpack at each elevation step and aspect (ibid.).

French avalanche forecasters have found the *SCM* chain useful for their operational work (ibid.). However, each model and the whole chain have limitations, e.g. lack of meteorological data as most weather stations are located in ski resorts and only start measuring once the season begins. However, there can be snow before the start of the season (ibid.). Since simulated snow depths cannot be corrected with observations, the error at the start of the season increases systematically throughout the winter (ibid.). Yet, the main limitation mentioned by the authors, that it cannot simulate snow accumulation and erosion caused by wind (ibid.), was resolved in a newer version (Morin et al., 2020; Rousselot et al., 2010). In 2014, Crocus was replaced by the

model SURFEX/ISBA-Crocus, and the modelling suite was renamed S2M. The SURFEX/ISBA-Crocus model considers the energy and mass exchanges between different surface types and the atmosphere (Vionnet et al., 2012). Consequently, it can better simulate the snow stratigraphy at the beginning of the season and be used in moderate elevations where the snow cover is often discontinuous and therefore more influenced by energy flows between the ground and the snow (Lafaysse et al., 2013). The S2M modelling chain is still operational as of 2024 in France (National Centre for Meteorological Research, 2024).

### 1.2.2 SNOWPACK

Based on the experience with Crocus and other modelling developments, researchers at the Swiss Institute for Snow and Avalanche Research (SLF) in Davos designed the model SNOWPACK in the late 1990s (Lehning et al., 1999; Morin et al., 2020). SNOWPACK builds on physical principles similar to those of Crocus. Still, it differs in how the meteorological input data is used and how the output is post-processed and operationally used (Lehning et al., 1999; Morin et al., 2020). While the *SCM* calculates representative snow cover characteristics for a particular region in the French Alps, SNOWPACK uses the data of a network of automated weather stations (AWSs) (WSL Institute for Snow and Avalanche Research SLF, 2023c) and simulates "the real local snowpack" at the site of the AWS (Lehning et al., 1999, p. 147). The simulation is calculated for so-called virtual slopes (N, E, S, W) at a slope angle of 38° at the same elevation as the AWS. SNOWPACK is operationally used in Switzerland with the above-mentioned station-based approach in nowcast mode (Morin et al., 2020). The simulation can also be forced with the output of numerical weather prediction (NWP) models in forecast mode or with a combination of both, as it is done in Italy, Austria and Canada (ibid.).

However, physically based snowpack models like Crocus and SNOWPACK and their post-processed outputs are difficult to systematically validate because objective and reproducible field measurements of avalanche hazard and snowpack stability are missing (ibid.). Furthermore, the resolution of these snowpack models is relatively coarse compared to snow processes such as blowing snow (when wind raises snow particles into the air; World Meteorological Organization (WMO), 2017), preferential deposition (the spatial variation of snow deposition due to the underlying topography; Lehning et al., 2008) or the avalanche path (Morin et al., 2020; Rousselot et al., 2010). Therefore, they could not be integrated into automated operational forecasting (Pérez-Guillén et al., 2022; Van Herwijnen et al., 2023). To forecast avalanches differently, statistical models, some based on machine learning methods, were developed (Purves et al., 2003; Schirmer et al., 2009). However, only a few were used operationally due to inaccurate or missing input data or because they were only applicable on a regional scale (Van Herwijnen et al., 2023). In the last five to ten years, thanks to increased computing power, improved data availability and novel machine learning algorithms, new models or model integrations have emerged (Pérez-Guillén et al., 2022; Van Herwijnen et al., 2023). For example, SNOWPACK has been implemented into ALPINE3D, a spatial, three-dimensional snow cover and earth surface model to predict natural avalanche probability (Bellaire et al., 2018). The

output of SNOWPACK was used as input for a subsequent mechanical model to predict snow instability (Reuter et al., 2018) and for random forest models to predict the avalanche danger level (Maissen et al., 2024; Pérez-Guillén et al., 2022), snow instability (Mayer et al., 2022) and wet-avalanche probability (Hendrick et al., 2023). The output of the instability model by Mayer et al. (2022) was, in turn, used as input for a random forest model to predict dry-snow avalanches in the vicinity of AWSs (Mayer et al., 2023).

So far, the output of the aforementioned snow instability model (Mayer et al., 2022) has neither been interpolated nor validated on a larger than regional scale. Nevertheless, there are other interpolation approaches using observation or weather data: Reuter et al. (2016) predicted snow instability in the Steintälli basin above Davos by external drift kriging using information from vertical profiles. However, the model was only tested locally and underestimated snow cover properties (Reuter et al., 2016). Richter et al. (2021) interpolated meteorological data from the AWSs and modelled spatially distributed snow instability also in the region of Davos. However, the model lacks validation with field data. This thesis attempts to close the two-fold research gap: Interpolate and test at a larger than regional scale.

## 1.3 Research Gap

The interpolation model developed in this thesis is based on the random forest model by Mayer et al. (2022) that assesses snow instability. The model is referred to as *instability model* henceforward (see Figure 1.1). It takes as input the simulated snowpack, the output of the SNOWPACK

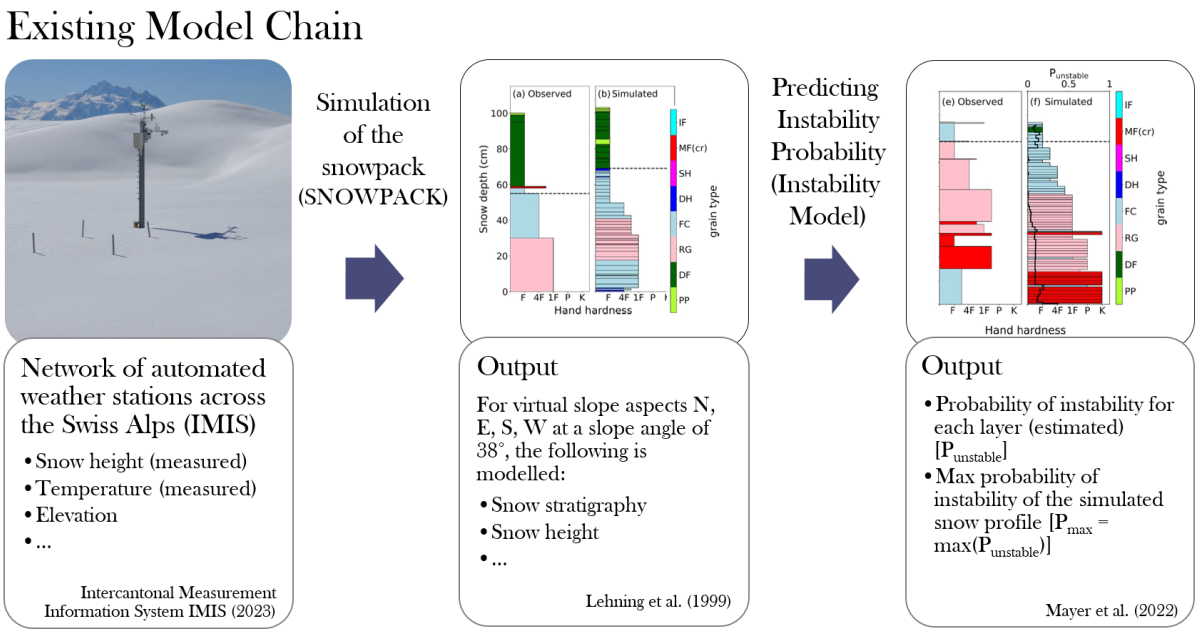


**Figure 1.1:** The existing model chain starts with the data of the automated weather stations that serve as input for the snowpack simulation model. The output of the latter is fed into an instability model that outputs, among others, the maximum probability of instability of a snowpack.

model, and calculates an instability probability for each layer of the snowpack (Mayer et al., 2022). Mayer et al. (2022) determine the instability probability based on the six features: Viscous deformation rate, critical cut length, skier penetration depth, sphericity of grains in the weak layer, mean of the ratio of density and grain size of the slab, and weak layer grain size. The model consists of 400 classification trees, which classify each layer as stable (0) or unstable (1) (ibid.). The resulting instability probability of each layer is the mean vote of all the trees (ibid.). Additionally, the instability model detects "[...] the weakest layer in the snowpack with one single index, the maximum probability of instability over all layers of the simulated snow profile" (ibid., p. 4607).

Since SNOWPACK simulates the snow cover at the location of the AWS, the output of the instability model is only valid for this point location: It predicts how stable the snowpack is at the location of the AWS, whereby a probability close to 0 stands for stable and one close to 1 for unstable (ibid.). However, there is no area-wide prediction of snow instability (Morin et al., 2020).

In this thesis, the spatial resolution of avalanche forecasts is increased by interpolating the predicted probability of instability at the location of the AWS. The aim is to enhance the modelling chain consisting of SNOWPACK and the instability model to predict the instability probability for any arbitrary point location on a 1 km x 1 km grid in the Swiss Alps. The interpolation output will be validated and tested, which is necessary if the model is to be integrated into the operational warning service. For the testing, external data such as avalanche observations and points from GPS tracks of backcountry skiing is used. Figure 1.2 shows the planned model extension.

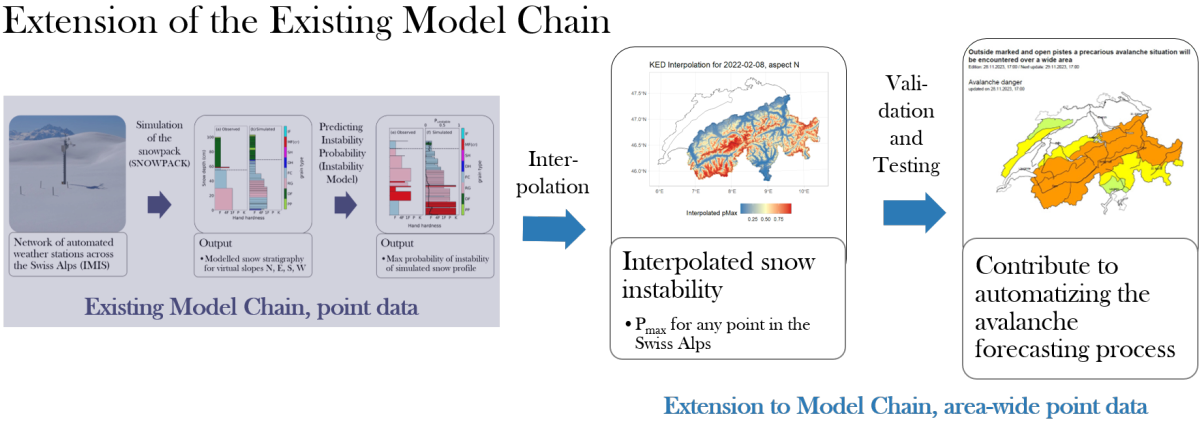


**Figure 1.2:** The model chain with the extension of the interpolation and testing that are part of this thesis.

### Research Questions

The two parts of the thesis, the model development including its validation and the testing of the model, are addressed with the following research questions:

**Part A: Design an interpolation model and validate its performance**

1. How can pointwise, predicted probabilities of instability be interpolated to cover greater areas? Which interpolation methods are suited for this task? What are the challenges and limitations?
2. How can the performance of the model be validated, and how does the model perform?

**Part B: Test the model with external data (avalanche observations, points of backcountry skiing GPS tracks)**

3. How does the model perform when tested with external data?
4. How suitable is the external data for testing high and low probabilities of snow instability?
5. What are the limitations of the testing data and the resulting implications?

## 1.4 Thesis Outline

The thesis is structured as follows: Chapter 2 defines important terms and assumptions. It summarises the process of avalanche formation and qualitatively describes the four winters on which this thesis is based. Chapter 3 describes the data used for the interpolation and testing. Chapter 4 deals with finding an optimal interpolation method and addresses the first two research questions. Chapter 5 presents and interprets the results of the interpolation, the validation and the testing, whereas Chapter 6 puts them into a broader context and discusses the implications. Chapters 5 and 6 also address the remaining research questions. Finally, Chapter 7 concludes and gives an outlook on potential further research and how the model could be integrated into the operational avalanche forecast process.

# 2 Background

This chapter characterises avalanches, explains their formation, and defines essential terms used in this thesis. The introduction to avalanches helps to understand the focus of this thesis, which lies on human-triggered dry-snow avalanches in the Swiss Alps. The chapter closes by describing the four winters from 2019/20 to 2022/23 since they compose the model's training and testing data.

## 2.1 Avalanches

"Snow avalanches can be placed into a suite of natural hazards [...] known as mountain-slope hazards" (McClung et al., 2022, p. 15). They are relatively small-scale compared to earthquakes or floods and restricted to mountainous terrain where the population density is generally lower than in urban or suburban areas (ibid.). Besides people, avalanches also affect the environment and industries such as transportation, construction, tourism and forestry (ibid.). Compared to other mountain-slope hazards such as rock or ice avalanches and landslides, avalanches are more frequent because snow is the weakest of the earth's surface materials (ibid.). Nevertheless, snow avalanches are rare (Schweizer, 2008).

### 2.1.1 Dry- vs. wet-snow Avalanches

Snow avalanches can be distinguished by their liquid water content as dry or wet (Harvey et al., 2019). The *Classification System for Liquid Water Content in Snow* by the International Association of Cryospheric Sciences (IACS) goes into further detail (Fierz et al., 2009): It consists of five classes (dry, moist, wet, very wet, soaked) according to the range of the water content (volume fraction in %). The distinction between dry and wet snow is crucial because it affects the formation mechanism for the corresponding avalanche type (Hendrick et al., 2023; McClung et al., 2022). Furthermore, the formation of wet-snow avalanches is less understood as field observations and measurements of liquid water content are often missing (Hendrick et al., 2023). The emphasis on dry-snow in this thesis stems from the upstream model, which predicts dry-snow instability (Mayer et al., 2022). Additionally, dry-snow avalanches are widespread: 82% of all avalanche accidents in Switzerland in the past 40 years resulting in injury or death were composed of dry-snow (Harvey et al., 2019).

### 2.1.2 Human-triggered vs. natural Avalanches

"In fact, most snow avalanches form by load that is added to the top of the snowpack when storms deposit snow or wind transports snow at the surface" (McClung et al., 2022, p. 17). If avalanches are triggered without human influence, e.g. by fresh-fallen snow, they are called

natural avalanches (WSL Institute for Snow and Avalanche Research SLF, 2024c). Most natural avalanches are triggered by snow loading (Schweizer, 2008). However, the additional load can also be artificial, e.g. winter sports enthusiasts, snowmobiles or avalanche blasting. In these cases, the avalanches are triggered by humans. The thesis concentrates on human-triggered avalanches due to the restrictions defined by the upstream model: "As the instability model [by Mayer et al. (2022)] was trained using stability tests related to human-triggered avalanches, its applicability to predict natural avalanches is not self-evident" (Mayer et al., 2023). The testing data was chosen accordingly: Both the GPS tracks and the observed avalanches were recorded by humans. For natural avalanches, other testing data would be needed, e.g. archived images of webcams filming natural avalanche terrain.

### 2.1.3 Avalanche Formation

Snow avalanches can further be classified according to their cohesion: "Loose-snow avalanches are characterized by low cohesion, while slab avalanches have enough cohesion to form the slab" (McClung et al., 2022, p. 75). Both types can be composed of dry or wet snow and can be triggered naturally or by humans. Human-triggered slab avalanches are more frequent and more dangerous than human-triggered loose-snow avalanches (ibid.): In the last 40 years in Switzerland, 95% of the avalanche accidents resulting in injury or death were slab avalanches (Harvey et al., 2019). In this thesis, slab and loose-snow avalanches are not distinguished.

However, it is important to understand how avalanches, especially slab avalanches, form in order to grasp the role of snow instability. Besides the additional load mentioned above, other conditions must be fulfilled for a slab avalanche to form: The range of the slope angle is between 25° and 55° (McClung et al., 2022), most often it is between 35° and 45° (Harvey et al., 2019). Furthermore, the layering of the snowpack is important. McClung et al. speak of a sandwich-like structure with "a weak layer in between thicker cohesive layers" (2022, p. 103). This unfavourable sandwich structure must have a spatial extent of at least 20 m x 20 m (ibid.). A fracture in the weak layer underneath the cohesive slab initiates the formation of an avalanche (ibid.). The fracture is not a simple shear fracture but rather a failure called "anti-crack" (Heierli et al., 2008; Schweizer et al., 2021). The weak layer collapses due to the combination of shear and pressure stress (Harvey et al., 2019). Consequently, the slab on top of it sinks and comes into contact with the bed surface (Schweizer et al., 2021). The energy thus released favours the crack propagation (Harvey et al., 2019). However, the slab avalanche is only released "If the gravitational pull on the detached snow slab is large enough to overcome friction – that is, the slope is steep enough (> 30 degrees)" (Schweizer et al., 2021, p. 387). In contrast, loose-snow avalanches are less dangerous than slab avalanches (McClung et al., 2022). They form under cold and calm conditions and start from a point, leaving a triangle-shaped avalanche path (ibid.).

Avalanches can be further classified, e.g. according to size and destructive power (Schweizer et al., 2021), but such properties are not considered in the model developed in this thesis.

## 2.2 Study Area

The study area is limited to the Swiss Alps as it is based on the network of automated weather stations (AWSs). It excludes the Jura, as there is neither enough training nor testing data available to create a meaningful interpolation model in this region (Maissen et al., 2024).

## 2.3 Definitions and Assumptions

Some terms require clarification:

- Validation vs testing: *Validation* (e.g. leave-one-out or ten-fold cross-validation) refers to evaluating the model with the training data, i.e. the predictions of snow instability, whereas for *testing* the model, external data (GPS track points, avalanche observations) will be drawn on.
- SNOWPACK vs snowpack: *SNOWPACK* (in capital letters) refers to the model with the same name, whereas *snowpack* refers to the physical layering of the snow.

## 2.4 The four Winters 2019/20-2022/23

Data from four winters is used to train, validate and test the model. The following subsections describe these winters. They focus on temperature, snow, avalanches and accidents.

### 2.4.1 Winter 2019/20: Warm and low in Danger

The following paragraphs summarise the information in German found in Trachsel et al. (2020): The winter of 2019/20 contains the second warmest period from November to March since the start of the measurements in 1864. The average temperature of each month deviates strongly from the long-term mean (1991-2020). While the temperatures were much lower in November 2019, they were much warmer during the rest of the winter, not considering some bad weather periods.

In high elevations, snowfall started in October and continued in November. Due to the heavy snowfalls, the snow depths were above average at the end of November in high elevations in the west, at the Main Alpine Ridge and south of the latter. The second snowfall period started in the days before Christmas and led to large amounts of new snow in the south, the west and along the northern flank of the Alps. January 2020 was characterized by little snowfall. It rained at the beginning of February, and shortly after, a storm brought snowfall to low elevations. The rain diminished the snow depths at low and middle elevations. Repeated snowfalls characterized the rest of the month. The third intensive snowfall period started at the beginning of March.

This period also brought stormy winds and, later on, rain. The rest of March was relatively dry. As a measure against the Covid-19 pandemic, ski resorts closed on 13 March 2020. April and May brought warm temperatures and sunny days.

The first large avalanches were observed in November 2019. In the second snowfall period before Christmas, there were many large and very large avalanches. In January 2020, however, the little snowfall led to low danger levels for a few days in a row, which is very untypical for this time of the year, according to the authors. At the beginning of February, rain triggered many wet-snow and glide-snow avalanches. The rain and storm led to a high danger level in the west and north. Many medium and large, but also very large wet avalanches, some also dry, were observed. Towards the end of February, the danger level decreased. The winter comeback at the beginning of March brought a lot of dry, later on also wet-snow avalanches. 11 March was the day with the most avalanches of the winter (almost 450).

During the winter of 2019/20, the lowest danger level occurred almost twice as often as in the long-term mean. The winter was less avalanche prone than the previous ten winters. Seven people were killed in or by avalanches off-piste, far fewer than the 20-year average of 22 victims.

### 2.4.2 Winter 2020/21: Warm and with persistent weak Layers

The following paragraphs summarise the information in German found in Zweifel et al. (2021): The second winter in the data set was warmer than the long-term mean. However, October and January temperatures were below average, while November, December, and February temperatures were above, and March was in the range of the mean. April and May were rather cold. In February, winds from the south brought record temperatures and Sahara dust, which accelerated the snow melt on south-facing slopes.

Snowfall started as early as October at mid to high elevations in the south and the east of Switzerland. November was dry. The intensive snowfall periods were at the beginning of December, in the middle and at the end of January, and in mid-March. Snowfall reached the low elevations in January, March and April. In December, snow fell in the south and the Inneralpine regions and later in the west and the north. At the beginning of January, precipitation alternated between snow and rain. From mid-January to the start of February, snow fell repeatedly and heavily. During this snowfall period, most of the snow fell at the Northern Alpine Ridge (4-5 m), but also the Central Plateau and Jura were covered in snow. In mid-March, the winter comeback brought snowfall at low elevations in the north and west and heavy snowfall at high elevations. Until May, snowfall reached low elevations a few times.

The first avalanches were registered in October. At the end of November, the snow cover was unfavourable for future snowfall. This weak layer persisted in the snowpack and often characterized the avalanche situation, together with the new snow and wind slabs. The danger level was considerable for quite a while in a widespread area. The danger level high was reached

a few times in December, for an entire week in January and at the beginning of February. The day with the highest avalanche activity was 28 January 2021 (1770 avalanches). At the end of January, a few large to very large avalanches were observed, damaging land and forest. At the southern flank of the Alps, the snowpack layering was more favourable, leading to much fewer avalanches. The warm temperatures in February led to wet-snow and glide-snow avalanches, sometimes of large dimension due to the thick snow cover. The danger level dropped at the beginning of March and increased again with the snowfall in the middle of the month, reaching the level high.

Throughout the winter of 2020/21, danger levels 3 (considerable) and 4 (high) were declared more often than on average, while the other levels were in the range of the long-term mean. 32 people were killed in or by avalanches, many more than the 20-year mean of 22. One accident occurred in the Jura, where the last deadly accident dates back to 1991.

### 2.4.3 Winter 2021/22: Warm and short

The following paragraphs summarise the information in German found in Pielmeier et al. (2023): The temperatures in the winter of 2021/22 were significantly higher than on average, especially on the southern flank of the Alps, where it was extremely warm and dry. In the north, the main snowfalls in December and February resulted in an average winter precipitation. In contrast, January and March 2022 were very dry and sunny. Spring was poor in precipitation, very sunny and warm.

The first snow fell in the first half of November at high elevations. Snowfall reached middle elevations at the end of November. More snowfall followed at the beginning of December, especially in the west and north and in the Prealps, the Jura and the Sotto Ceneri. The rest of December was dry and warm. At the end of the month, precipitation fell as rain up to 2800 m a.s.l. In January, a lack of snow became apparent in the south. Winter storms and abundant snowfall periods characterized February, except in the south, where only little precipitation fell. March was poor in precipitation. The next snowfall in the north occurred at the beginning of April and in the south at high elevations at the end of April. May was again much drier and warmer than the long-term mean, accelerating the melt of the already thin snow cover at high elevations.

The snow cover from autumn was a weak base when the heavy snowfall in December arrived. New snow, wind slabs and persistent weak layers led to a high danger level at the beginning of December. Natural avalanches were widespread, and humans easily triggered avalanches. In some places, the abundant new snow covered the weak layers sufficiently so that they could not be triggered anymore by humans. Glide-snow avalanches were registered towards the end of December due to rain. Some of them were very large and reached the valley bottom. Not many avalanches were registered in January as the snowpack stabilized, and there was less snow than on average. The heavy snowfall periods and winter storms in February led to a high danger level lasting several days. During this period, most of the dry-snow avalanches were registered.

The highest avalanche activity was recorded on 3 February 2022, with almost 600 avalanches. The danger level remained considerable and sometimes reached the level high due to repeated snow- or rainfall and persistent weak layers. The danger level decreased only at the end of the month. During March, the moistening of the snowpack increased, leading to glide-snow avalanches during the day. The snow melt accelerated due to Sahara dust in March. The snowfall at the beginning of April led to a high danger level in the west and south. However, it could not compensate for the lack of snow this winter.

In this winter, the avalanche situation was more favourable than on average. 14 avalanche victims were registered off-piste, far fewer than the 20-year average of 21 victims.

### 2.4.4 Winter 2022/23: Warm and scarce in Precipitation

The following paragraphs summarise the information in German found in Pielmeier et al. (2024): The winter of 2022/23 was considerably warmer than the long-term mean. It was preceded by a warm summer. Even in October and November, the temperatures were significantly above average. In the south, it was very dry in autumn. Only from mid-November to mid-December, as well as from mid-January to mid-February, it was colder than on average.

The first snow was registered at the beginning of November at high elevations, reaching middle elevations later in the month. Over the entire winter, however, precipitation was far below average, and especially in the south, the drought persisted. Locations at middle elevations were only partly covered in snow. In contrast, snow at low elevations (below 1000 m a.s.l.) was only registered on single days in mid-December, at the end of January, and in March and April. The mean snow depths were considerably below average over the entire winter, except at high elevations in Valais, where they were above average. Between mid-February and mid-March, the snow depth in the Swiss Alps was the lowest since measurements began. Spring brought precipitation above average, at high elevations in the form of snow. The snow depths increased, especially above 2000 m a.s.l. and in the west. However, snow remained scarce in the south in spring. The snow melt accelerated with the warm and sunny days in June, and in most regions, the snow cover was gone two weeks earlier than on average.

The first snow in November led to a low avalanche activity. The snow at middle elevations at the beginning of December increased the avalanche danger level. Some medium and large natural avalanches were registered. In the second half of December, the snow reached the lowlands. At high elevations, the avalanche danger level increased considerably. Just before Christmas, the snow line rose to 2200 m a.s.l. Precipitation moistened the snow pack below the snow line, triggering many glide-snow avalanches. At high elevations, old snow was easily triggered by the overload of new snow, resulting in many dry-snow avalanches. Most of the avalanches occurred in Valais. A few of them were very large and reached the green valley bottom. Two more very active avalanche periods followed in March and April 2023. In March, snow fell on a faceted snow surface. The repeated snowfall and the stormy winds at high elevations increased the danger level to considerable and sometimes even high. The highest dry-snow avalanche

activity was registered in the second half of March. The highest number of avalanches was observed on 12 March 2023 (more than 300 avalanches). Due to the fluctuating snow line, the snowpack was moistened, leading to glide-snow avalanches. Despite the snowfall in March, the snow depths were still below average at the end of the month. In April, the avalanche situation remained critical in regions with precipitation since the weak layers in the old snow were not covered enough by the new snow. The danger levels considerable and high were reached. For the first time this winter, the snow depth reached the long-term average, but only in the north. At the end of April, warm temperatures and rain moistened the snowpack, leading to many wet-snow avalanches. However, these avalanches were relatively small due to the small snow depths. Snowfall in mid-May reached 1800 m a.s.l. and increased the avalanche danger level to considerable at high elevations.

23 people died in avalanche accidents in the winter of 2022/23, a number similar to the 20-year average of 21.

# 3 Data

The interpolation is mainly based on modelled snow instability data at the location of automated weather stations (AWSs) (WSL Institute for Snow and Avalanche Research SLF, 2023c). Out of the four winter's instability data, the first three winters will be used to train the interpolation model (2019/20, 2020/21 and 2021/22), whereas the last winter (2022/23) will be used in addition for the testing. The testing draws on external data: Avalanche observations for high instability and GPS points for low instability. This chapter describes the data, data sources and preparation separately for the interpolation and the testing. The data was preprocessed in R Statistical Software (v4.3.2, R Core Team 2022). The Swiss coordinate system CH1903/LV03 (EPSG: 21781) served as reference coordinate system. Data stemming from a different coordinate system was transformed accordingly.

## 3.1 Interpolation Data

### 3.1.1 Instability Data from Automated Weather Stations (AWSs)

The snowpack instability data at the location of automated weather stations (AWSs) is the primary input for the interpolation model (Mayer et al., 2022) (see also Chapter 1). Snowpack instability, hereafter referred to as instability, is defined as the "[...] sensitivity of the local snowpack to artificial or natural triggers" (Statham et al., 2018, p. 681, cited in Mayer et al., 2022, p. 4593). The higher the instability of the snowpack, the more likely an avalanche is released (Techel et al., 2022). Instability is caused by the interaction of snowpack, terrain and meteorological drivers, which vary over time (Mayer et al., 2022). The instability probability is itself the output of a model chain consisting of SNOWPACK (Lehning et al., 1999) and the instability model developed by Mayer et al. (2022). The model chain is run in nowcast mode with meteorological data at a selection of 118-145 weather stations (depending on the winter) belonging to the Intercantonal Measurement and Information System (IMIS) (WSL Institute for Snow and Avalanche Research SLF, 2023c) as well as on 17 stations that are part of SwissMetNet (SMN), the automatic measurement network of the Federal Office of Meteorology and Climatology (MeteoSwiss) (2023) (see Figure 3.1). The location of the IMIS stations is mostly at flat sites, representing the surrounding area (Mayer et al., 2022). Their elevation corresponds to the elevation of potential avalanche starting zones (Techel et al., 2022). The histogram in Figure 3.2 shows the distribution of the stations' elevations (in m a.s.l.): Most of the stations lie between 2000 and 2500 m a.s.l.

The output of the instability model is, among others, the maximum instability probability ($\rho_{max}$) in the range [0,1], defined as the instability probability of the layer with the highest $\rho_{max}$ value in the snowpack, $\max(\text{prob}_{\text{unstab}})$ (Mayer et al., 2022). A low probability stands for a stable snowpack and a high probability for an unstable snowpack. The layer with the highest instability

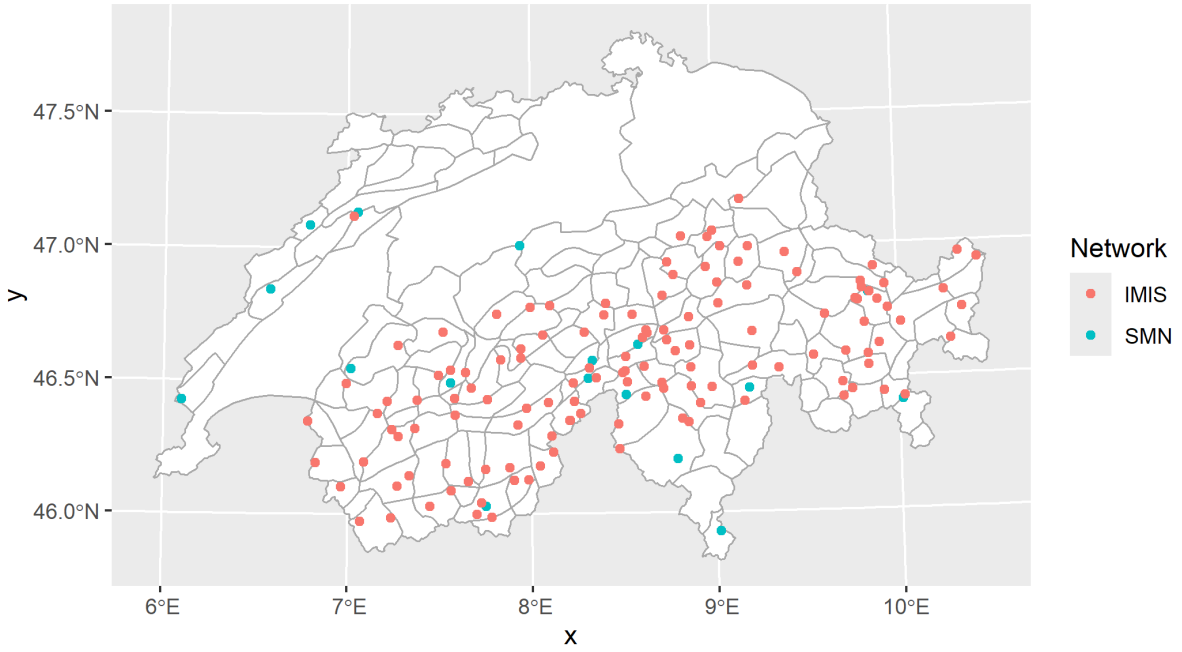


**Figure 3.1:** The location of the AWSs where SNOWPACK and the instability model are run. The colours distinguish the networks the stations belong to. The grey delineation shows the warning regions.

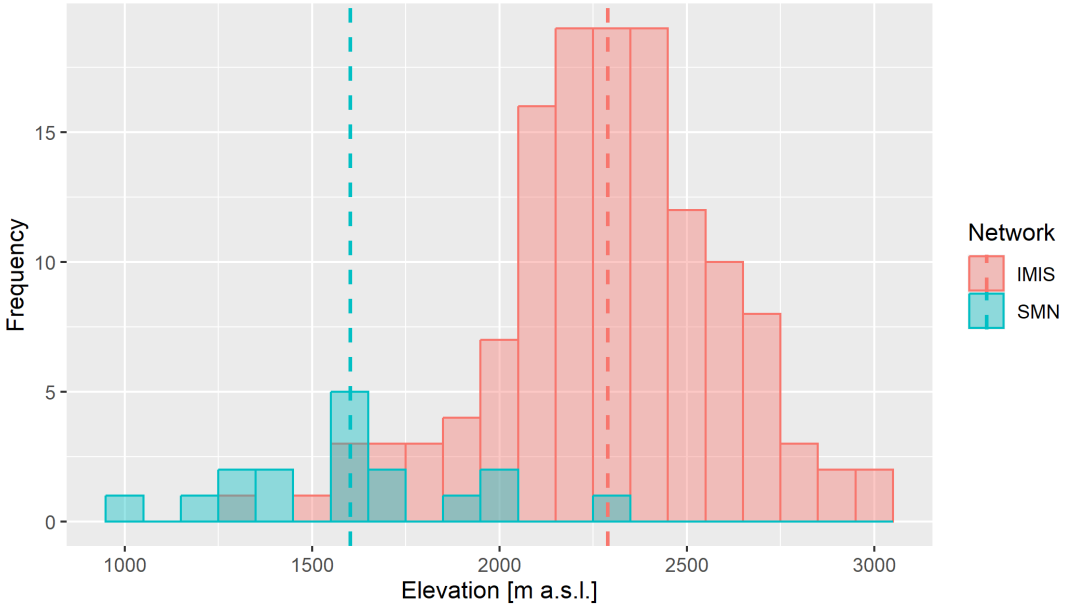


**Figure 3.2:** Histogram of the elevation of the automated weather stations at which the model chain of SNOWPACK and the instability model is run. The colours distinguish the networks the stations belong to; the dashed line indicates the mean.

probability is defined as the weakest layer in the snowpack (Mayer et al., 2022). The $\rho_{max}$ value is calculated at each location of an AWS for each date and the four virtual aspects (N, E, S, W), even if the station is located in a flat area. Table 3.1 shows that the amount of available data varies between the winters. First, due to the increasing number of stations in the IMIS

network over the four winters. Second, some days lack predictions, e.g. 4 and 8-11 April 2023, or some stations have no prediction for a certain day and aspect. Besides the missing data in April, the data of the last winter is without gaps as there is a $\rho_{max}$ value for each station, calendar day and aspect from 16 December 2022 to 10 May 2023, which results in 80'620 data points. For the previous three winters, however, the data set is incomplete in the previously mentioned sense. In total, 18'215 data points are missing from 1 December 2019 to 1 May 2022. Figure 3.3 shows that the amount of data is lower at the beginning and at the end of the winter. When considering the available data points for the first three winters, the minimum $\rho_{max}$ value is 0.011, and the minimum snow depth is 30 cm. Thus, the data set does not contain zeros for the instability probability or snow depth. The 18'215 missing predictions were not added as their $\rho_{max}$ value was unknown. Furthermore, mistakenly adding them with a zero instability probability could bias the model, leading to underestimating the avalanche situation. The predictions for the stations were joined with the coordinates of the stations to georeference the predictions.

**Table 3.1:** The available instability predictions per winter in detail.

| **winter** | **date range** | **number of days** | **max. number of AWS/d** | **number of data points** |
|---|---|---|---|---|
| **2019/20** | 01.12.2019-01.05.2020 | 153 | 118 | 60'157 |
| **2020/21** | 01.12.2020-01.05.2021 | 152 | 118 | 61'532 |
| **2021/22** | 01.12.2021-01.05.2022 | 152 | 122 | 65'659 |
| **2022/23** | 16.12.2022-10.05.2023 | 139 | 145 | 80'620 |
| **total** | | **596** | | **267'608** |

### 3.1.2 Additional Weather Stations at low Elevations and Snow Line Data

Apart from the instability data, the interpolation is based on data from additional weather stations at low elevations (Federal Office of Meteorology and Climatology MeteoSwiss, 2023). These weather stations help to generate a smooth gradient towards the Central Plateau in the north and Ticino in the south. Only stations that measure snow height were considered. Since the instability model (Mayer et al., 2023) is not run at these stations, their instability value was assumed to be zero. To substantiate this assumption, the observed snow line, the elevation at which the continuous snow cover ceases, was additionally used to filter the stations at low elevations. The minimum snowline data set contains the observed minimum elevation of the continuous snow cover for the aspects north and south for specific days and locations. A daily mean snow line elevation was calculated from the snow line for north and south. This mean was used to filter the MeteoSwiss stations as follows: If the elevation of a station was equal to or lower than the mean of the minimum elevation of the continuous snow cover for a particular day, it was assumed that there is no snow and the $\rho_{max}$ value was set to zero. If, on the other hand, its elevation was above the mean, no assumptions about the $\rho_{max}$ value could be made,

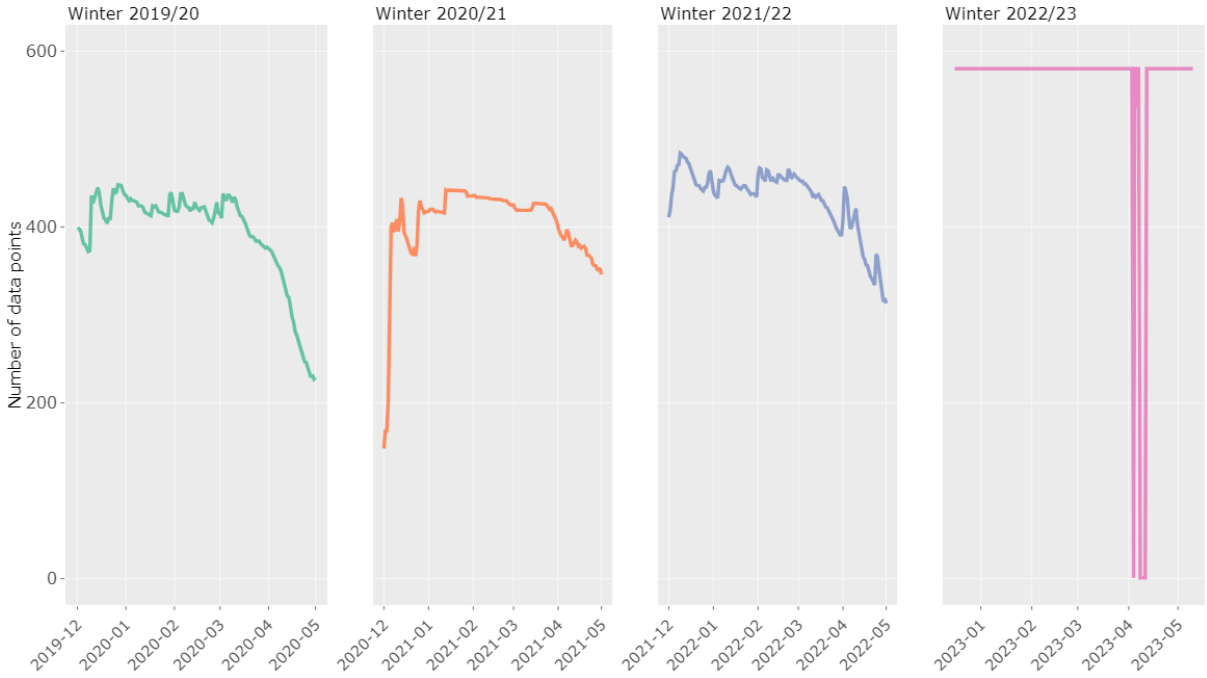


**Figure 3.3:** The varying number of daily data points over the first three winters and the constant number over the last winter. Some days in April 2023 (4, 8-11 April) lack a prediction.

and it was not kept for further modelling. Therefore, all the resulting MeteoSwiss stations had an assumed but robust $\rho_{max}$ value of zero.

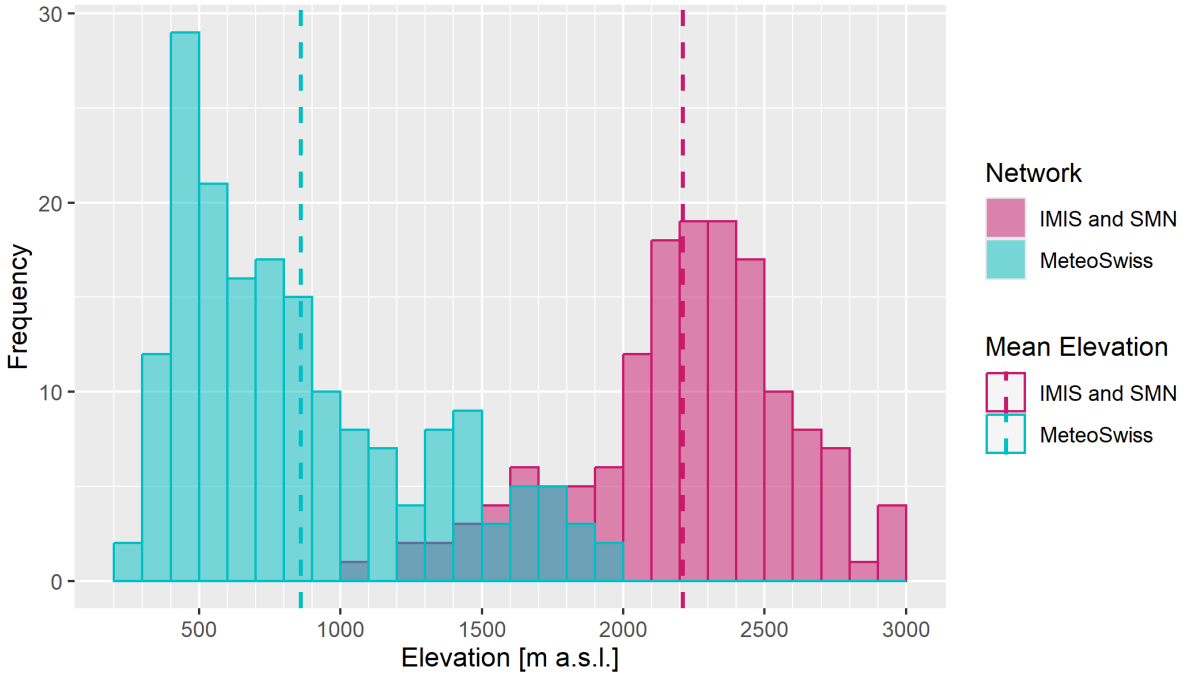


**Figure 3.4:** Histogram of the elevations of all the stations used for the interpolation. The mean elevation of the MeteoSwiss stations is 859 m a.s.l., and the mean for the IMIS and SMN stations is 2211 m a.s.l.

The histogram in Figure 3.4 shows that the MeteoSwiss stations are located mainly at elevations below 1000 m a.s.l. If all or most of the MeteoSwiss stations were included in the model, they could bias the model towards lower elevations and thus lower instability. Since the model targets high elevation locations, only a small sample of the MeteoSwiss stations were included in the model. After filtering with the mean daily snow line, a random spatial sample of 30 of the remaining MeteoSwiss stations was included in the further model development. The sample corresponds to 25% of the 118 respectively 122 AWSs used to train the interpolation model (see Table 3.1). Over the three winters, there are 156 distinct stations in the data set because some stations are no longer operated, and others have been added during this period.

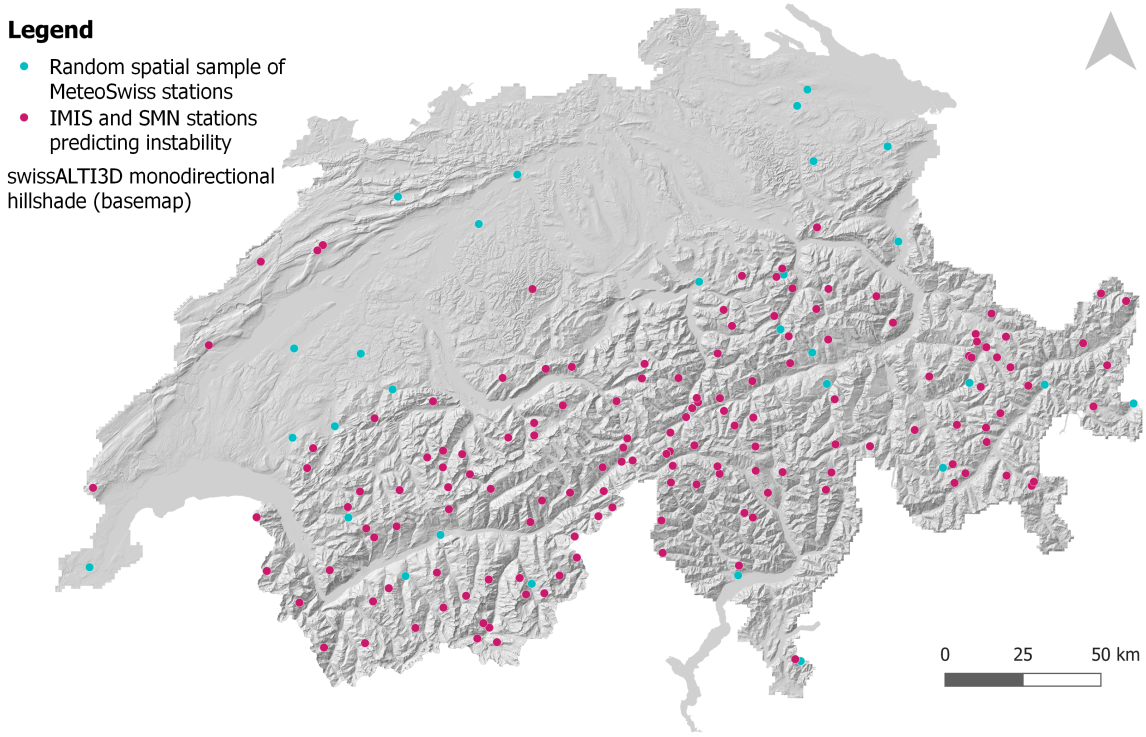


Data sources: Intercantonal Measurement Information System IMIS (2023), Federal Office of Meteorology and Climatology MeteoSwiss (2023).

**Figure 3.5:** Stations used for the interpolation, coloured according to their network, placed on a monodirectional hillshade.

### 3.1.3 Digital Elevation Model (1 km resolution)

A digital elevation model (DEM) with a resolution of 1 km (DEM 1 km) was used to interpolate the instability probabilities. The DEM 1km was derived from a DEM with 250 meters resolution (Federal Office of Topography swisstopo, 2001). The elevation values were aggregated from the resolution of 250 to 1000 meters by taking the mean value. The resolution was chosen to be big enough to consider more than a single slope since the model is not designed to assess small-scale instability. At the same time, however, the resolution should not cover too many valleys, as conditions can vary considerably between valleys.

## 3.2 Test Data

The model was tested with two external data sets: avalanche observations and points from GPS tracks (see Table 3.2). Different digital elevation models (DEM) were used to interpolate the instability probability at the location of this external data. All the data is described hereafter.

**Table 3.2:** Overview of the data used for testing the model.

| **Source** | **Instability (Probability)** | **Uncertainty/Errors** | **Reference** |
|---|---|---|---|
| GPS tracks of backcountry skiers | low (close to 0) | coordinates, just a selection of all the backcountry skiing community | Schmudlach, 2022; 2023 |
| Avalanche observations | high (close to 1) | biased; coordinates, time and snow type may be uncertain | SLF, 2023 |

### 3.2.1 Digital Elevation Model (10 meters resolution)

A digital elevation model (DEM) with a resolution of 10 m (DEM 10 m) was used to process the avalanche observation points (see below). The DEM 10 m was derived from a DEM with a 2 m resolution (Federal Office of Topography swisstopo, 2019). The elevation values were aggregated from 2 to 10 meters by taking the mean value. Additionally, the DEM 10 m was transformed to LV1903 as all the analysis was done in this coordinate system.

### 3.2.2 Grid of the Swiss Alps (1 km resolution)

To compare the distribution of the predicted $\rho_{max}$ values at the location of observed avalanches and GPS points, the model was further run on a grid with a resolution of 1 km covering the Swiss Alps. The grid was created by first selecting the warning regions used by the SLF in their avalanche bulletin (WSL Institute for Snow and Avalanche Research SLF, 2024a), which contained GPS track points or avalanches. The relevant warning regions were then intersected with the DEM 1 km.

### 3.2.3 Avalanche Observations

Avalanches directly indicate instability (Techel et al., 2022). McClung et al. precise that avalanches indicate that "[...] the snow is unstable on the respective slope, and it is most likely unstable on other avalanche paths (similar exposure and elevation)" (2022, p. 181). The

SLF collects information from people who observed avalanches on backcountry activities and uses it to evaluate and improve the information in the avalanche bulletin (WSL Institute for Snow and Avalanche Research SLF, 2024b). Recorded avalanches can thus be attributed an instability probability of 1 and be used to validate high instability probabilities predicted by the model. The avalanche observation data collected and provided by the WSL Institute for Snow and Avalanche Research SLF (2023) contains the release points of observed avalanches. The following properties are recorded for each avalanche: id, coordinates, trigger date, aspect of the starting zone, elevation of the starting zone, moisture type, avalanche size, mean fracture thickness, fracture width and whether the avalanche was triggered remotely. Some of the release points lack an elevation and/or aspect. For these points, the missing information was extracted from a DEM with a resolution of 10 meters (see above). Since the observations are recorded by humans, mainly by rescue services and the public (Techel et al., 2022), they come with uncertainties and contain a bias: Humans only go out if the conditions are not too dangerous (ibid.). Thus, for areas and days with a high avalanche danger, no or fewer avalanches can be observed (ibid.). Observations can only be made if the weather is good enough since fog or heavy snowfall makes it hard to see avalanches. Even if the visibility is good, the recording itself may be inaccurate if one has to estimate the release point of an avalanche on the opposite slope. If the avalanche has already come down, it may be hard to tell how old it is. Furthermore, errors when reporting the avalanche cannot be excluded. Conversely, a lack of avalanche observations for a particular area during a specific time does not necessarily mean no avalanches or no risk, but rather no people around at this time (Grímsdóttir et al., 2006; Techel et al., 2018).

The avalanche release points were preprocessed as follows: The coordinates of the location of the avalanche were transformed from WGS84 to the Swiss Coordinate System LV03 (Federal Office of Topography swisstopo, 2016) to have all data in the same coordinate system. Plotting the data on a map showed that the transformation was correct, but some avalanche observations were outside Switzerland. As the model only works within Switzerland due to the DEM 1 km being available for Swiss territory, these observations were discarded. The avalanche observations were further filtered according to moisture type such that the data set only contained dry avalanches (no wet or unknown moisture type). Additionally, naturally triggered avalanches were excluded to retain only human-triggered avalanches. Furthermore, only avalanches on calendar days for which instability predictions are available could be considered, as the model can only predict if there is an input for that day. Therefore, in the winter of 2022/23, only avalanche observations from 17 December 2022 until 27 April 2023 were considered because instability predictions for the first half of December 2022 and some days in April 2023 are missing.

For the testing, not only the release point was taken into account, but also the avalanche path as described by Winkler et al. (2021): An avalanche trajectory was calculated by assuming that avalanches follow the slope line as water does (R function: *flowPath*). The length of an avalanche was set to a maximum of 60 meters. The points on the trajectory were resampled to an interval of 10 meters, resulting in a maximum of seven points per avalanche. The elevation of each point along the trajectory was extracted from the DEM 10 m. It was further assumed

that the aspect of the points of the avalanche trajectory was the same as for the release point. If the aspect was combined, e.g. NE for northeast, the corresponding row was split into the two main aspects, north and east; all the other values were copied. Table 3.3 shows the number of avalanche observations and trajectory points.

**Table 3.3:** Available avalanche observations and trajectory points per winter in detail.

| winter | date range | number of days with avalanches | number of avalanche release points | number of avalanche trajectory points |
|---|---|---|---|---|
| **2019/20** | 01.12.2019-01.05.2020 | 73 | 340 | 2278 |
| **2020/21** | 01.12.2020-01.05.2021 | 111 | 796 | 5302 |
| **2021/22** | 01.12.2021-01.05.2022 | 95 | 503 | 3321 |
| **2022/23** | 17.12.2022-27.04.2023 | 111 | 661 | 4379 |
| **total** | | **389** | **2300** | **15'280** |

### 3.2.4 Points of GPS Tracks (ARPD)

The Global Positioning System (GPS) points stem from tracks that backcountry skiers recorded in the winters of 2019/20 and 2020/21 and uploaded on at least one of the three online platforms Skitourenguru.ch (Skitourenguru, 2024a), Gipfelbuch.ch (Bergportal GmbH, 2024) and Camp2Camp.org (Camptocamp Association, 2024). According to its source (Schmudlach, 2023), the GPS points were passed without triggering an avalanche. They thus represent stable terrain and were attributed an instability probability of zero as opposed to the avalanche observations (see Table 3.2). The tracks were collected, preprocessed and cleaned by G. Schmudlach for the Avalanche Risk Property Dataset (ARPD) (ibid.). As part of the ARPD preprocessing, the track points were resampled at an interval of 10 meters (ibid.). Additionally, several properties were calculated for each point, e.g. aspect, elevation, distance to the next ski slope and terrain indicator (ibid.). To avoid drawing conclusions about individual persons, every 20th point of a GPS track was used in this thesis, which leads to a 200-meter interval per track in the present data set. Furthermore, only points further away than 200 meters from a ski slope were considered. This resulted in a sample of 43'120 GPS points. The uncertainties are similar to the ones mentioned for the avalanches: The GPS points are just a small selection of snow sports enthusiasts practising backcountry or off-piste activities (Zhang et al., 2018). Degraeuwe et al. (2024) estimate that 1 out of 2000 actual backcountry travels are contained in the ARPD. Days with nice weather and good conditions attract more people; thus, most GPS points might come from such days and areas. The data set does not contain information about signs of instability that people could have noticed on their way, such as shooting cracks, whumpfs, etc. Shooting cracks indicate locations prone to being triggered by humans (Techel et al., 2022), whumpfs are a "[...] sudden failure of the weak layer due to rapid localised loading manifesting itself by collapse" (Schweizer et al., 2010). We neither know how close they were to triggering an avalanche. Furthermore, two platforms are monolingual, i.e. Gipfelbuch.ch is in German, whereas Camp2Camp.org is in

French. Only skitourenguru.ch has been available in four languages since 2015/16. However, the language of the people who make their tracks available is not recorded (G. Schmudlach, Skitourenguru, personal communication, 5 August 2024). Thus, there is probably bias related to language in the data.

As a first step, the sample was filtered by calendar day: The first tracks were recorded in November 2019 and the last in mid-May 2021, but there are no predictions for these early and late days of the winter season. Only GPS points from 1 December 2019 to 1 May 2020 and from 1 December 2020 to 1 May 2021 were kept. The data set was then filtered by the terrain indicator ($TI$) to keep only points in potential avalanche terrain. According to the ARPD manual, the "$TI$ indicates how suitable a terrain point is to trigger an avalanche" (Schmudlach, 2022, p. 7). The concept of the $TI$ is similar to the Avalanche Terrain Exposure Scale (ATES) used in Parks Canada (Parks Canada, 2024). For each point in the terrain, the $TI$ combines several parameters relevant for avalanches, e.g. the slope angle ($SA$), slope curvature, slope size and forestation into a single indicator (Schmudlach et al., 2018). The $TI$ focuses on avalanches triggered by humans. However, it considers neither current conditions nor alpine difficulties (ibid.). The $TI$ scale distinguishes four classes (see Table 3.4). Since the GPS points were used to validate low instabilities, thus stable terrain, the data was filtered according to a $TI \geq 0.25$, as this is the threshold where avalanche terrain begins (Skitourenguru, 2024b).

One data point with a missing aspect was taken out of the data set. Furthermore, the points were filtered according to their slope angle ($SA$): Only points with a $SA$ equal to or higher than 20° were kept. At a $SA$ of around 20°, the GPS points reach the maximum, while the number of accident points is still low according to Schmudlach (2022). Therefore, the relative risk is also low. However, 20° is still below "the median slope angle of all movement points in avalanche terrain ($TI > 0.25$)" of 25° discovered by Winkler et al. (2021). But as mentioned before, the number of transition points is highest at around 20°, which was the main reason to keep the $SA$ relatively low. After the above filtering, 11'178 GPS points remained. Their aspect given in degrees was converted to the classes N, E, S and W. As with the avalanche trajectory points, GPS points containing a combined aspect, e.g. NE, were split into two data points for each aspect, while the rest of the row was copied. Table 3.5 summarises the data set after the preprocessing. In the following winters, the data collection for the ARPD was not continued.

**Table 3.4:** Description of the four classes of the terrain indicator (*TI*), slightly adapted (Skitourenguru, 2024b).

| Class | Values | Interpretation |
|---|---|---|
| None | 0-25% | No avalanche terrain (Here: Refers to slab avalanches triggered by skiers). |
| Simple | 25-50% | Terrain requires common sense, proper equipment and the discipline to respect avalanche warnings. Simple terrain is usually low avalanche risk, ideal for novices gaining backcountry experience. On days when the Backcountry Avalanche Bulletin is rated high (4) or extreme (5), these trips may not be free from avalanche hazards. You may want to rethink any backcountry travel that has exposure to avalanches. |
| Challenging | 50-75% | Terrain requires skills to recognize and avoid avalanche prone terrain. Big slopes exist on these trips. You must also know how to understand the Backcountry Avalanche Bulletin, perform avalanche self-rescue and be confident in your route-finding skills. You should take a Recreational Avalanche Course prior to travelling in this type of terrain. If you are unsure of your own, or your group's ability to navigate through avalanche terrain, then consider hiring a professional, certified guide. |
| Complex | 75-100% | Terrain demands a strong group with years of critical decision making experience in avalanche terrain. There can be no safe options on these trips, forcing exposure to big slopes. As a minimum, you or someone in your group must have taken an Advanced Recreational Avalanche Course and have several years of backcountry experience. Check the Backcountry Avalanche Bulletin and ensure everyone in your group is up for the task and aware of the risk. This is serious country, not a place to consider unless you are confident in the skills of your group. If you're uncertain, consider hiring a professional, certified guide. |

**Table 3.5:** ARPD: Available calendar days, GPS points and tracks per winter.

| winter | date range | number of calendar days | number of GPS tracks | number of GPS points |
|---|---|---|---|---|
| **2019/20** | 01.12.2019-01.05.2020 | 110 | 440 | 3962 |
| **2020/21** | 01.12.2020-01.05.2021 | 108 | 494 | 4686 |
| **total** | | **218** | **934** | **11'178** |

# 4 Methods

This chapter is divided into three parts: In the first part, the concept of interpolation is summarised. The second part discusses the methods used to build the interpolation model, including its cross-validation. The third part describes the methods for testing the model with external data. The interpolation, the postprocessing and the validation were performed using the R Statistical Software (v4.3.2, R Core Team 2022).

## 4.1 Idea behind Spatial Interpolation

Spatial interpolation is "[...] the prediction of exact values of attributes at unsampled locations from measurements made at control points in the same area" (O'Sullivan et al., 2010, p. 250). In this sense, spatial "[...] interpolation is a type of spatial prediction" (2010, p. 250), as the predicted values usually cannot be confirmed by true values. Burrough et al. (2015, p. 147) add that "[...] the usual objective is to generate a set of predictions on a regular grid." In our case, the modelled snow instability probabilities at the locations of the AWSs (Mayer et al., 2022; WSL Institute for Snow and Avalanche Research SLF, 2023c) are the measurements at control points. These probabilities at point locations are interpolated over a grid covering the Swiss Alps. All spatial interpolation methods rely on spatial autocorrelation being present in the data (O'Sullivan et al., 2010), which Burrough et al. (2015) define by objects closer to each being generally more similar than objects further away. This echoes Tobler's "first law of geography: everything is related to everything else, but near things are more related than distant things" (Tobler, 1970, p. 236). However, the interpolation methods differ in that they make different use of the measurements at control points and thus lead to different results (O'Sullivan et al., 2010).

## 4.2 Applied Interpolation Methods

A basic $k$ nearest neighbours ($knn$) method was applied for the first interpolation. Although it was assumed from the beginning that this method would be too coarse for mountainous terrain such as the Swiss Alps, resulting in a "[...] 'blocky' or stepped estimate of the underlying field" (ibid., p. 274). However, it gives a first impression and serves as a lower bound for more complex interpolation methods. As a second method, ordinary kriging ($OK$) was applied. $OK$ is a univariate kriging method assuming a constant trend, i.e. a constant mean, for the instability probability prediction (Chilès et al., 2012; Li et al., 2014). The two methods were not validated with external data; they were only qualitatively assessed using the interpolation maps for some dates and aspects. Due to their inadequacy (see Chapter 5), kriging with external drift ($KED$), a multivariate version of kriging, was applied to interpolate the snow instability probability (Li et al., 2014; O'Sullivan et al., 2010). Elevation served as an additional variable, the so-called

drift. This third method was not clear from the beginning, but the result of a more extended evaluation, see the decision tree in Figure 4.2. The three methods were applied to the four aspects separately to find out if one model fits all aspects. The three methods and proceedings are described in detail in the following subsections.

### 4.2.1 *K* nearest Neighbours (*knn*)

*K* nearest neighbours (*knn*) interpolation uses a local spatial average based on the $k$ nearest neighbouring control points (O'Sullivan et al., 2010). Neighbourhood is defined as "[...] a geographically localised area" (Grekousis, 2020, p. 27), and it is based on the assumption that control points within the neighbourhood have more influence on the point to predict than control points outside. The neighbourhood is specified by the number of nearest neighbours $k$ to consider for the prediction. Using a fixed number of neighbouring points instead of a fixed radius has the advantage that the effective radius varies according to the density of the points (O'Sullivan et al., 2010): The denser the points, the smaller the effective radius and vice versa. The number of $k$, in turn, determines the nature of the interpolation surface: The higher the number of $k$, the smoother and more homogeneous the surface – at the risk of information loss. "Eventually, when all control points in the study region are included, this is identical to the simple average" (ibid., p. 274). A low $k$ results in abrupt transitions between the control points, especially if the control points are not distributed equally over the study area (Li et al., 2014). In addition to the number of neighbours $k$, the *knn* interpolation can be weighted by a kernel function to capture the intensity of the neighbourhood relationships, resulting in a weighted nearest neighbours interpolation (Grekousis, 2020).

In contrast to kriging, which will be treated in the next section, *knn* is a deterministic method "[...] in the sense that once the method and any necessary controlling parameters are set, only one solution surface is possible" (O'Sullivan et al., 2010, p. 274). Consequently, there is no error estimation and no information about the reliability of the interpolated values (Li et al., 2014). Furthermore, *knn* assumes that the data at any location can be estimated from the nearest control point. This assumption is questioned by some authors when it comes to gradually varying phenomena like precipitation or temperature (Burrough et al., 2015). They argue that the distribution of the observations and not the phenomenon itself will dominate the interpolation (ibid.).

As a preparation for the *knn* interpolation, the optimal number of $k$ for four different kernel types (rectangular, Epanechnikov, Gaussian, optimal) was determined by calculating the mean squared error (*MSE*) with leave-one-out cross-validation ($LOOCV$). In $LOOCV$, a single control point is removed at a time, and its value is predicted using all the other control points as input for the interpolation (Holbert, 2024). The input variables for the prediction of the $\rho_{max}$ value were the coordinates ($x$ and $y$) and the elevation [m a.s.l.] leading to the formula: $\rho_{max} \sim x + y + elevation$. The $\rho_{max}$ values were not transformed for the *knn*. Since the predicted

$\rho_{max}$ values are the average of their $k$ nearest neighbours, they will be within the range of [0,1].

The *LOOCV* of the *knn* interpolation showed that the differences between the different kernel types are minimal and that the optimal value for $k$ is 5 (see Figure 4.1). The rectangular kernel type being equal to the unweighted *knn* interpolation (uniform distribution), it was decided to use this nearest neighbour method with $k = 5$.

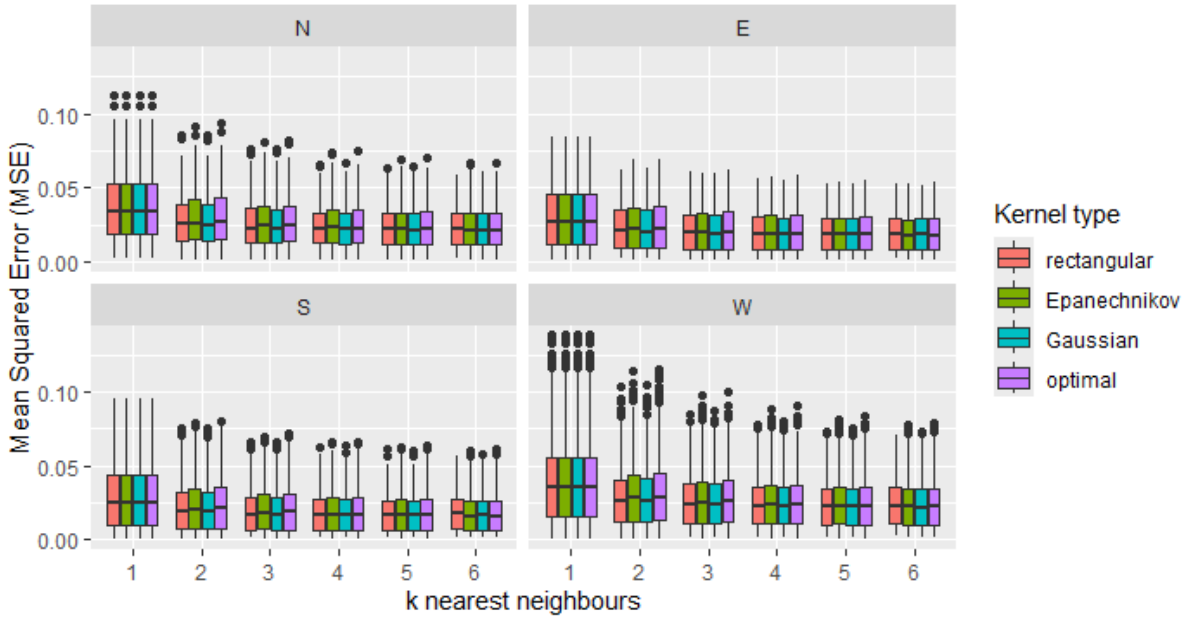


**Figure 4.1:** Mean Squared Error (MSE) for different numbers of nearest neighbours $k$ and different kernel types. The interpolation is based on coordinates and elevation and was calculated with data from the three winters of 2019/20-2021/22.

The predicted $\rho_{max}$ values were interpolated with *knn* on a 1 km x 1 km grid. For a few days and aspects, the predicted instabilities were mapped. The method was validated visually on these maps.

### 4.2.2 Kriging

Kriging is "interpolation with geostatistics" and was named after a South African mining engineer, D. G. Krige (Burrough et al., 2015, p. 172). In contrast to *knn*, kriging belongs to the family of the stochastic methods, which "[...] incorporate the concept of randomness and provide both estimations (i.e. deterministic part) and associated errors (stochastic part, i.e. uncertainties represented as estimated variances)" (Li et al., 2014, p. 175). Kriging uses "[...] the control point data as a sample to find optimum values for the weights of the data values included in the interpolation of each unknown location" (O'Sullivan et al., 2010, p. 295). The interpolation function is optimised to predict the value at an unknown location without bias and with minimum variance, a best linear unbiased estimate (BLUE) (Burrough et al., 2015; Li et al., 2014; Oliver et al., 2014). In contrast to simple methods such as *knn*, it can be used if an

attribute is irregularly distributed over space and the sample's density highly varies (Burrough et al., 2015).

Several types of kriging exist (O'Sullivan et al., 2010). To determine the most appropriate ones, the instability prediction data was examined according to the proceeding outlined in the decision tree in Figure 4.2, which is based on Li et al. (2014) and O'Sullivan et al. (2010). The numbering of the subchapters starting with "Q" follows the order of the questions in the decision tree.

### Q1: Data Transformation

The first question was whether to transform the instability probabilities [0,1]. Ordinary kriging interpolation without transforming the $\rho_{max}$ values predicted negative $\rho_{max}$ values ([-0.14, 0.84]). This phenomenon, known as undershooting, concerned all elevations, but especially the Central Plateau. In addition, tests for normal distribution, which requires theoretically infinite values, failed. Therefore, $\rho_{max}$ values [0, 1] were logistically transformed as follows:

$$\rho_{\text{maxLogit}} = \log(odds) = \log\left(\frac{\rho_{max}}{1-\rho_{max}}\right) \tag{4.1}$$

The logit transformation is suitable for proportions in the range of [0, 1] and attempts to avoid concentrations at both ends of the range (Burrough et al., 2015). To prevent infinite $\rho_{maxLogit}$ values as $logit(0) = -\infty$, the $\rho_{max}$ values of 0 were adjusted by adding 0.025 before transforming them logistically. There was no $\rho_{max}$ value of 1 in the data; thus, no adjustment was needed. This resulted in a range of the $\rho_{maxLogit}$ values of [-3.7, 3.7], with -3.7 corresponding to 0 ($\rho_{max}$; low instability) and 3.7 to 1 ($\rho_{max}$; high instability).

### Q2: Kriging Method

Three samples with different variability were selected from the training data to determine which kriging method and theoretical variogram function would suit. The variation was determined by calculating the standard deviation (sd) and the interquartile range (IQR) per calendar day and aspect. The standard deviation tells us how the values deviate from the mean, while the IQR is the length of the interval between the first and the third quartile (Stahel, 2002). The IQR is more robust to outliers than the sd and more suitable for skewed data. However, since the aim was to find extreme variation, I combined both to determine the samples (see Figure 4.3).

The first sample contained the calendar days and aspects with the highest variation in the $\rho_{maxLogit}$ values; the second sample the calendar days and aspects with the lowest variation; and the third sample the days and aspects with medium variation. Each sample consisted of 20 data points. The idea behind this sampling strategy was that if the model performs well on days and aspects with high respectively low variability, it also does on the days in between.

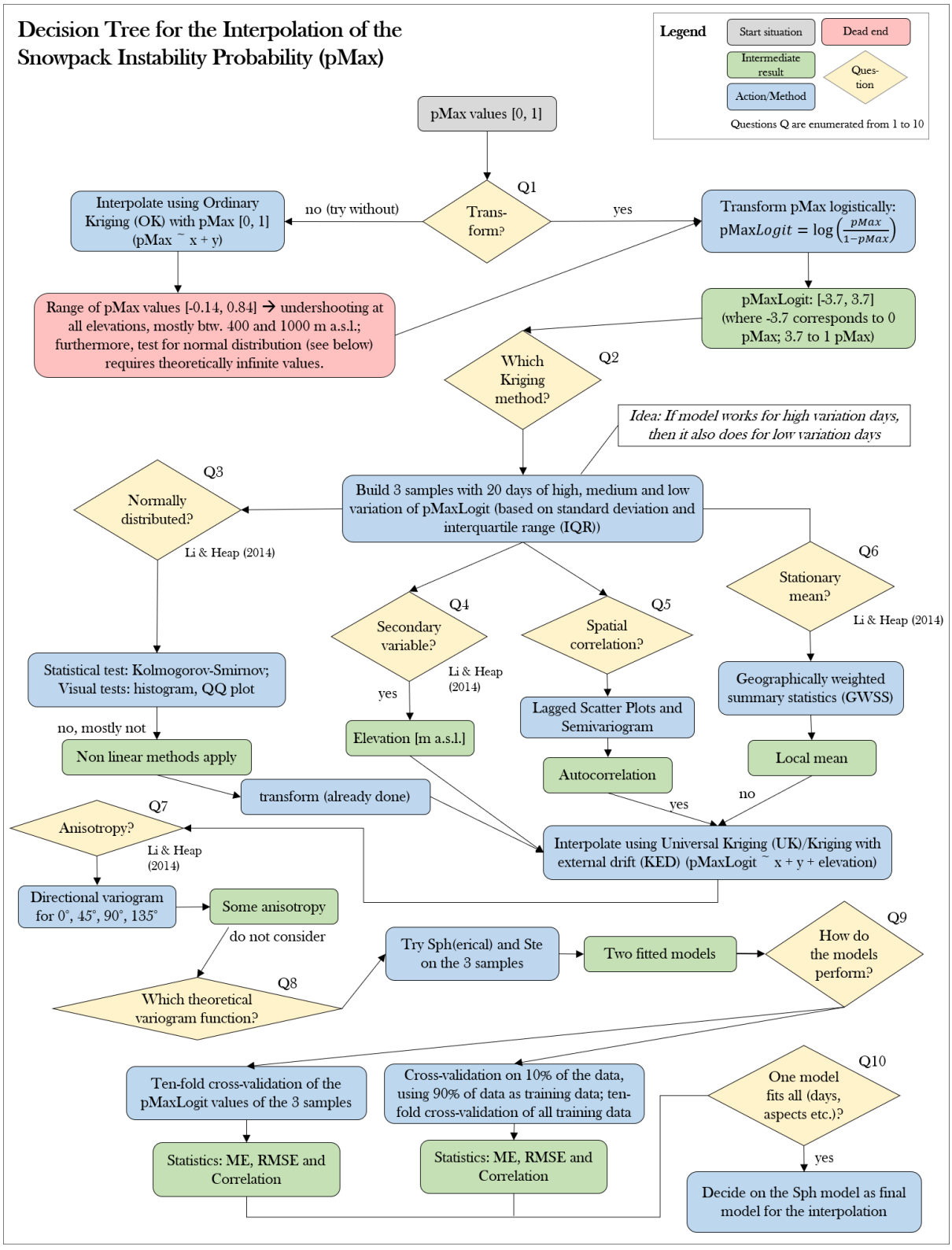


**Figure 4.2:** Decision tree applied to the kriging methods. The Q refers to questions to be answered to determine the method.

The medium sample was used to check how the model performed for values in between. The question regarding the kriging method is answered in Q6.

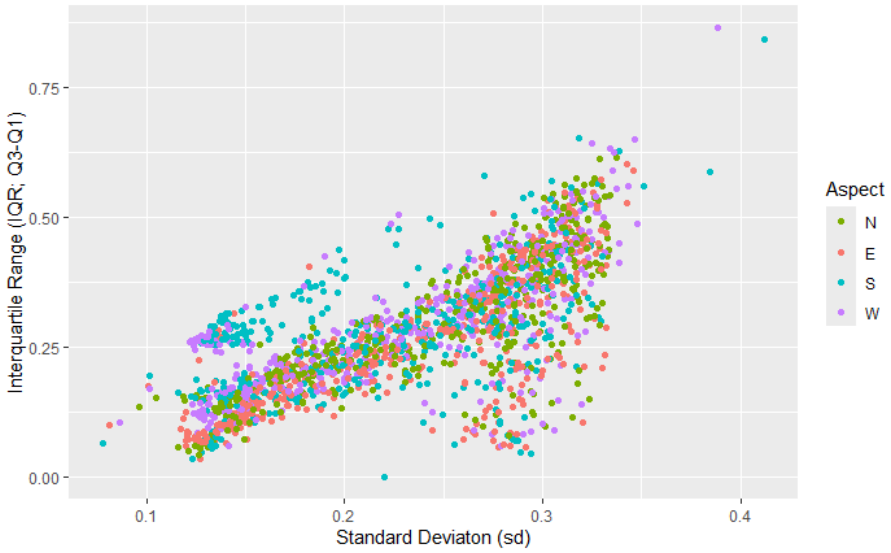


**Figure 4.3:** Interquartile range and the standard deviation per day and aspect of all the $\rho_{maxLogit}$ values of the training data (winter 2019/20-2021/22).

### Q3: Normality

Several tests and checks were performed on the three samples to get closer to a suitable method (Li et al., 2014): After the logit transformation, the Kolmogorov-Smirnov test was applied to test if the data is normally distributed. Furthermore, histograms and quantile-quantile plots (qq plots) were examined. The statistical and visual tests revealed that the three samples are mostly not normally distributed despite the logit transformation.

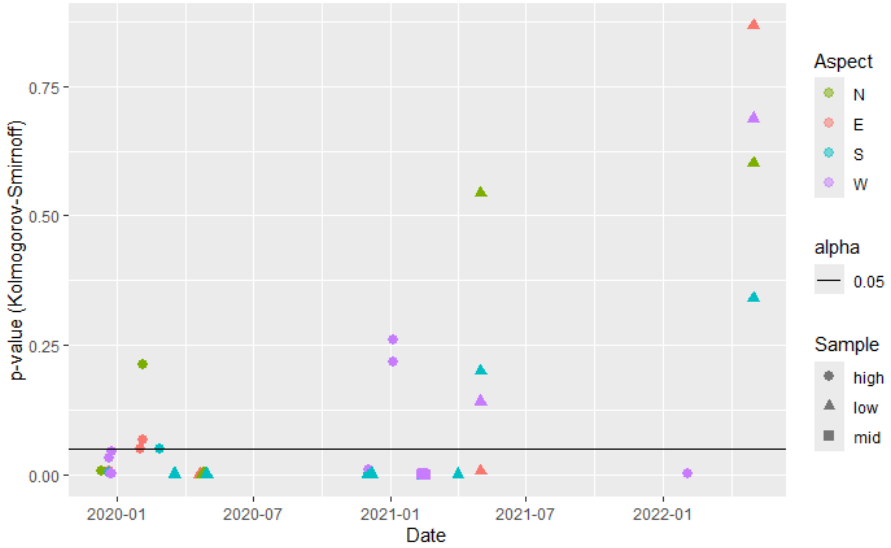


**Figure 4.4:** Testing the $\rho_{maxLogit}$ of the three samples for normality using the Kolmogorov-Smirnov-Test. The p-values of most days and aspects are greater than 0.05; thus, a normal distribution cannot be assumed.

**Q4: Secondary Variable**

In addition to the aspect and the coordinates, a secondary, exhaustively sampled variable may help to increase the interpolation quality (ibid.). Snowfall generally has a positive elevation gradient, i.e. the higher the elevation, the greater precipitation and wind speed (Grímsdóttir et al., 2006; Grünewald et al., 2014). Thus, elevation influences avalanche initiation and affects the avalanche risk (Grímsdóttir et al., 2006; McClung et al., 2022). Furthermore, "[...] the formation of weak layers such as surface hoar is often dependent on forest cover and temperatures, and therefore, on elevation" (Grímsdóttir et al., 2006, p. 129). Thus, elevation is added as a secondary variable to the model.

**Q5: Spatial Autocorrelation**

As mentioned initially in this chapter (see 4.1), spatial autocorrelation is a prerequisite for interpolation. To see if autocorrelation is present, lagged scatter plots were produced for all days and aspects of the three samples. They can be explained as follows: "For a given lag or separation distance, measured values at each location are plotted against measurements from locations separated by that lag" (Holbert, 2024). Elevation was set as the dependent variable. The two lagged scatterplots in Figure 4.5 give an example of the correlation of the $\rho_{maxLogit}$ values.

Most days and aspects of the three samples show a spatial autocorrelation, especially for distances up to 40 km. However, on some days and aspects, no autocorrelation is detectable. Sample variograms were plotted later in the process to prepare for the kriging model. Since they plot the differences in values for pairs of control points against their difference in distance, they also indicate whether spatial autocorrelation is present or not (Burrough et al., 2015; O'Sullivan et al., 2010). The difference on the y-axis is expressed as semivariance $\gamma$, which is half the variance of the differences between the values at the control points (Oliver et al., 2014). The differences in distance are grouped by a lag function of distance (Holbert, 2024). The variograms of the three samples generally show an increase in semivariance with increasing distance, as shown in Figure 4.6.

**Q6: Stationarity**

According to O'Sullivan et al. (2010, p. 107), the idea behind stationarity is that "[...] the rules that govern a process and control the placement of entities, although probabilistic, do not change, or *drift* over space." Like normality, stationarity is part of the theoretical assumptions of geostatistical methods (Burrough et al., 2015). For kriging, however, the "[...] assumption of data stationarity is usually not true" (Li et al., 2014, p. 176). The same authors clarify that the assumption is not strict for some kriging methods, e.g. universal kriging ($UK$) or kriging with external drift ($KED$). Others call it a "second-order stationarity" (O'Sullivan et al., 2010,

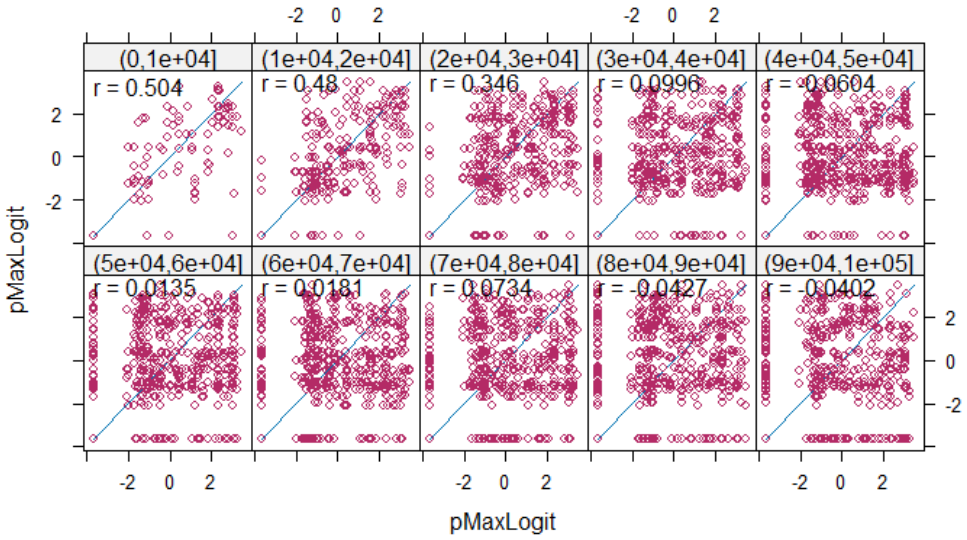


**(a)** Lagged scatterplot for 5 January 2021, aspect W.

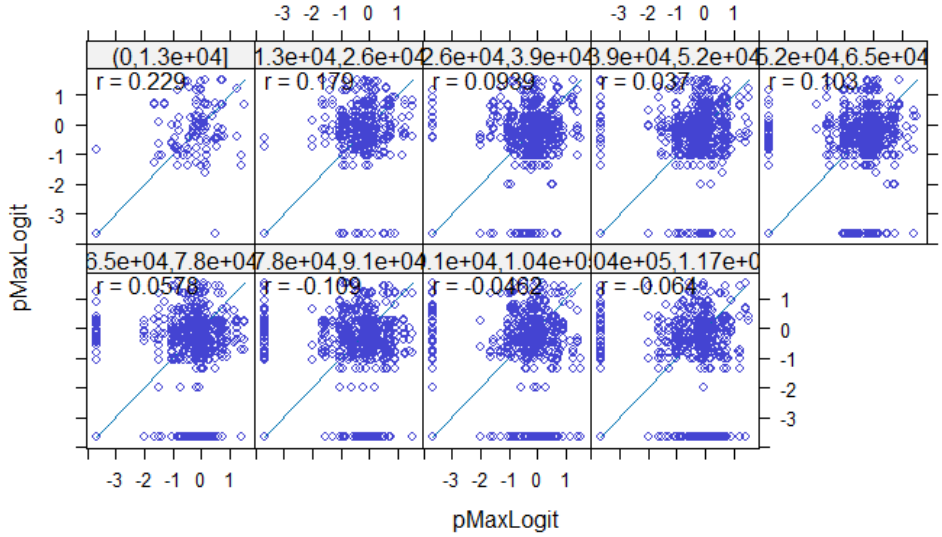


**(b)** Lagged scatterplot for 14 February 2021, aspect W.

**Figure 4.5:** Two examples for a lagged scatterplot, one from the sample with high variation (a) and one from the sample with medium variation (b).

p. 302), which means that the variance only depends on the distance. There is no formal test for stationarity (Oliver et al., 2014). However, geographically weighted summary statistics (GWSS; R function *gwss*, package *GWmodel*) can be calculated for the $\rho_{maxLogit}$ values per day and aspect, and the local variance can be plotted on a map to see whether it varies. Geographically weighted summary statistics are based on a localised mass point distribution (LMPD) calculated by assigning high weights to close observation points and low weights to points further away (Brunsdon et al., 2002). Depending on the day and aspect of the three samples, the local variance changes less or more than in the example in Figure 4.7. Thus, stationarity cannot be assumed.

The non-stationary nature of the phenomenon can further be explained by the topography influencing weather and climate: The dominant air currents from the west bring humid air from the

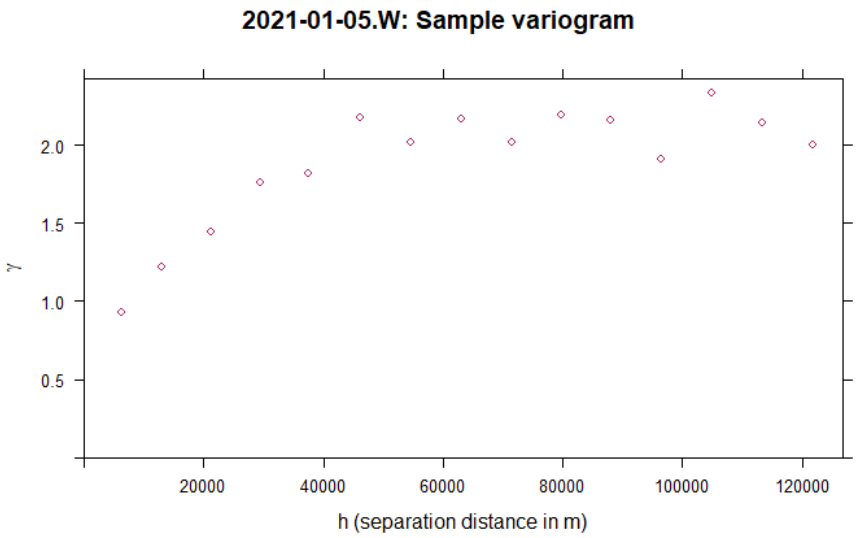


**Figure 4.6:** Sample variogram for 5 January 2021, aspect W, plotting the semivariance $\gamma$ of the point pairs and their separating distance, grouped by a lag function.

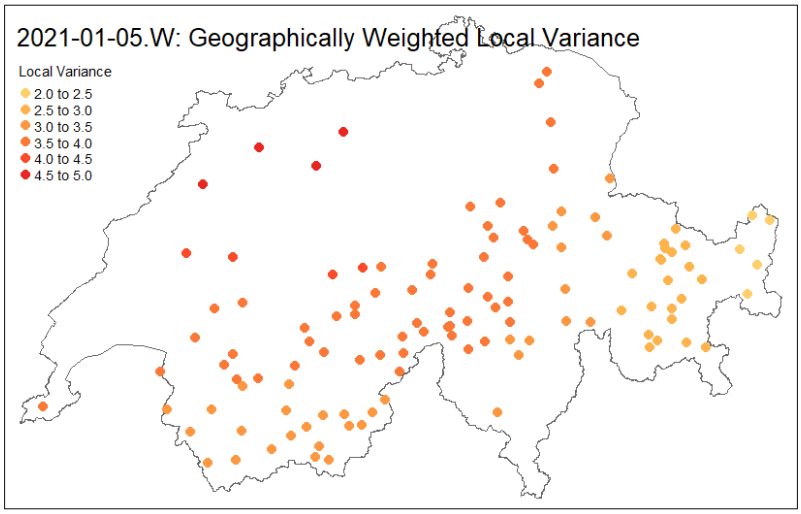


**Figure 4.7:** 5 January 2021, aspect W: Plotting the local variance of the $\rho_{maxLogit}$.

Atlantic to the Alps. During westerly wind conditions, weather activity is considerably greater on the north side of the Alps than on the south side. In contrast, the Alps shield the Inneralpine regions, such as Valais and the Engadin, from precipitation leading to dry conditions (Federal Office of Meteorology and Climatology MeteoSwiss, 2015), whereas abundant precipitation characterises the Prealps (National Centre for Climate Services NCCS, 2021).

The findings of Q3 to Q6 can be summarised as follows: The logit-transformed snow instability probabilities per day and aspect, $\rho_{maxLogit}$, are spatially correlated but neither normally distributed nor stationary in the strict sense. Elevation is a suitable secondary variable available for interpolation. Following the decision tree in Li et al. (2014), kriging with external drift (*KED*) with the elevation as an external drift parameter was applied in the final model. As preparation for *KED*, *OK*, which assumes a constant trend, was touched on.

### Q7: Anisotropy

To check for anisotropy, i.e. "[...] directional effects in the spatial variation of the data" (O'Sullivan et al., 2010, p. 290), a directional variogram was plotted: Point pairs are divided into four plots according to the four axis north-south, northeast-southwest, east-west and southeast-northwest (see Figure 4.8). The directional variograms of the three samples with high, medium and low variation showed no apparent directional effects: On some days and aspects in the high variation sample, there seemed to be an anisotropy; on others, there was not. There were hardly any directional effects in the low and medium variation samples. As the anisotropy was not constant in the three samples, it was not considered in the kriging model.

### Q8: Theoretical Variogram Function

A regular mathematical function, the theoretical model, can summarise the spatial variation (ibid.). Two theoretical variogram functions, spherical (Sph) and Matérn, M. Stein's parameterisation (Ste), were evaluated on the three samples. The function takes as arguments the three parameters partial sill, range and nugget (see Figure 4.9). The nugget indicates the variance at zero distance, which theoretically is also zero because it is the difference between the point and itself (Burrough et al., 2015). However, the nugget can have a positive value as it consists of the "[...] variance of measurement errors combined with that from spatial variation at distances much shorter than the sample spacing, which cannot be resolved" (ibid., p. 174). The sill is the point at which the semivariance reaches its maximum, and the curve of the fitted variogram levels off (O'Sullivan et al., 2010). The partial sill is defined as sill minus the nugget. The range indicates the distance at which the levelling off occurs and the spatial autocorrelation ceases as the variance does not increase anymore with further distance (Burrough et al., 2015). The partial sill, range and nugget for the variogram model were fitted by eye for each day and aspect of the three samples by weighting the maximum semivariance, the maximum distance and the mean semivariance respectively by a factor (see example in Figure 4.10). This resulted in 20 factors for each parameter and theoretical variogram function per sample.

### Q9: Model Performance

The factors for the three parameters of the different fitted functions were then averaged and tried on the three samples to see how the fitted semivariogram matched the experimentally derived points. Additionally, cross-validation was carried out on the three samples separately (R function *cv.krige*, package *gstat*). According to Kohavi (1995, p. 2), "In a $k$-fold cross-validation, [...] the dataset $D$ is randomly split into $k$ mutually exclusive subsets (the folds) $D_1$, $D_2$, ..., $D_k$ of approximately equal size." $K$ was set to ten for all three samples, which means that the model was trained on nine folds and tested on the tenth fold, which was done ten times. After the validation, the logit of the interpolated $\rho_{maxLogit}$ was reversed, and four diagnostic statistics were calculated: the mean error ($ME$), the root mean squared error ($RMSE$) and the correlation

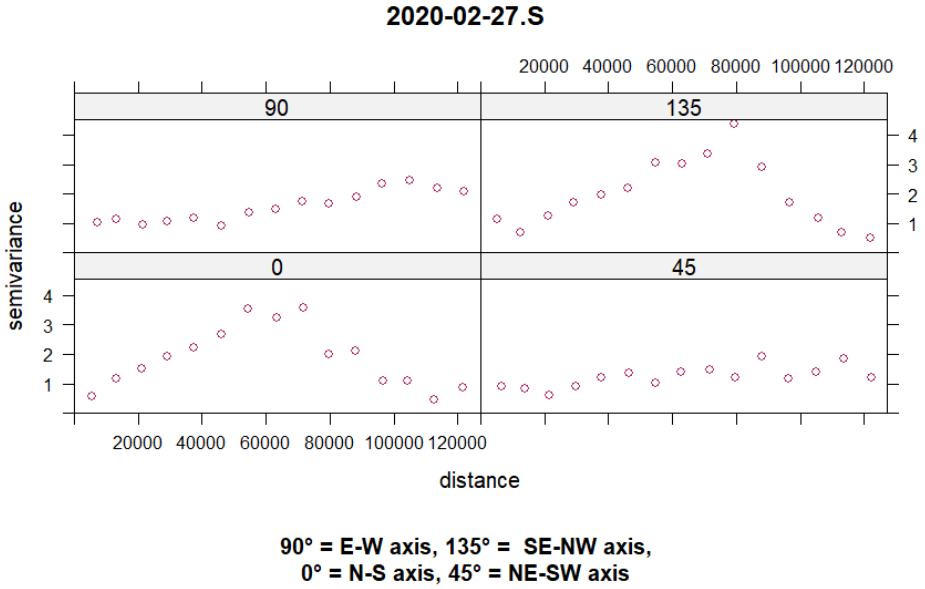


**(a)** Directional variogram for 27 February 2020, aspect S (high variation sample).

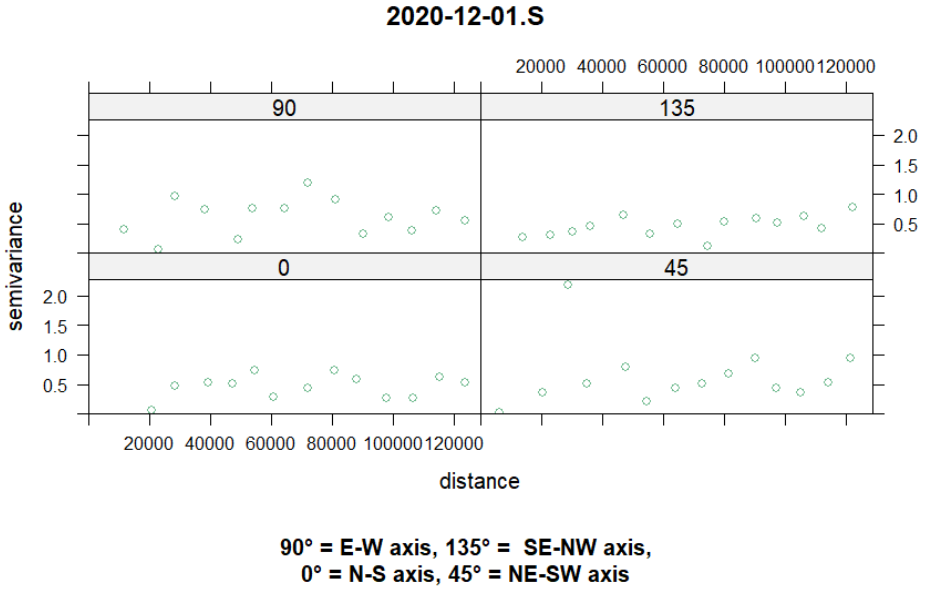


**(b)** Directional variogram for 1 December 2020, aspect S (low variation sample).

**Figure 4.8:** Two examples for a directional variogram, one from the high variation sample (a) and one from the low variation sample (b).

between the observed and the predicted values. As a second validation method, all the training data was randomly split into 90% training and 10% test data and cross-validated. The logit of the interpolated $\rho_{maxLogit}$ was reversed. The residuals, i.e. the delta between observed and predicted $\rho_{max}$ values, were plotted to see if the model over- or underestimates the instability. As a third validation method, a ten-fold cross-validation was performed on all the training data but grouped per aspect. All the results from the methods described in this paragraph can be found in Chapter 5.

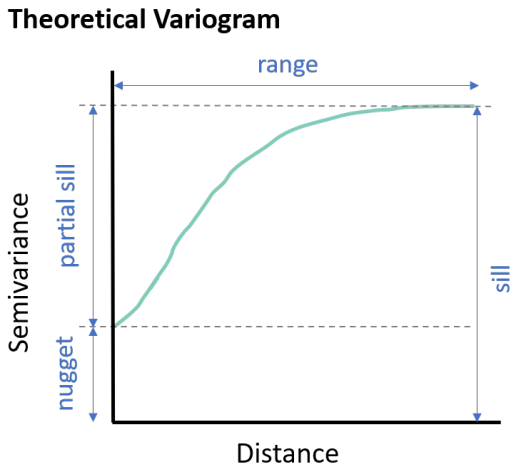


**Figure 4.9:** Theoretical semivariogram showing semivariance, sill, partial sill, range, and the nugget.

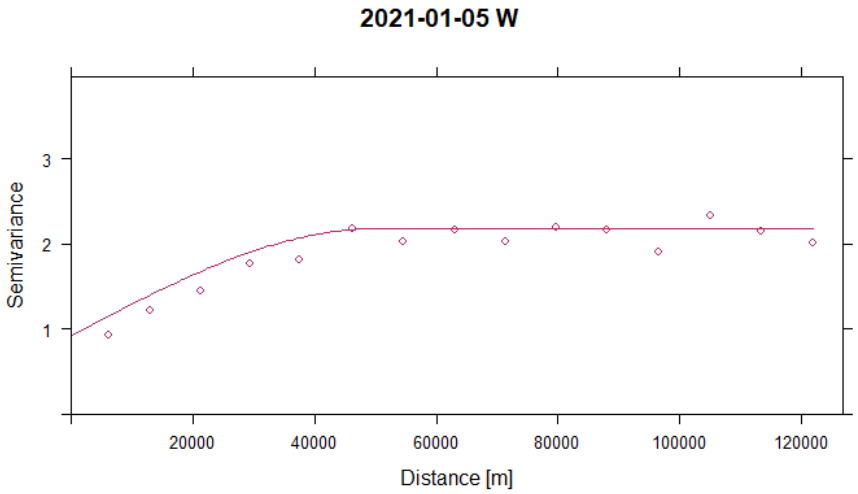


**Figure 4.10:** 5 January 2021, aspect W: Fitting the points of the sample variogram with a weighted spherical variogram function (the model). The following factors were used as weights for the parameters: 0.55 * maximum semivariance for the partial sill, 0.5 * maximum distance for the range and 0.5 * mean semivariance for the nugget.

#### Q10: Final Model

The outcomes of the two validation methods were analysed to determine whether one interpolation model fits all aspects and to determine the final theoretical function and the weighting factors.

### 4.2.3 Challenges and Limitations of Kriging

The different kriging methods and names are not used consistently in the literature, which can be confusing (Hengl et al., 2003). Especially universal kriging ($UK$) and kriging with

external drift (*KED*) are sometimes used equivalently. However, the local trend is modelled as a function of the data coordinates in the former and as a function of secondary data in the latter (Burrough et al., 2015). According to Webster et al. (2007) and O'Sullivan et al. (2010), the selection and fitting of a model should not be underestimated due to several reasons: The quality of the semivariance estimates depends on the number of point pairs. The more pairs used to estimate the semivariance, the more reliable the latter (O'Sullivan et al., 2010). However, at short and long distances, where the estimates are most important to estimate the nugget, range and sill, there are the fewest points and, thus, the least reliable estimates. Additionally, since the distances are binned, there is not a semivariance for every distance, and hence, the function is not continuous (ibid.). In this regard, "the experimental semivariogram can fluctuate greatly from point to point. Sometimes, for example, there is no steady increase in the variance with distance, as is implied by most models" (ibid., p. 300). Fitting by eye, as applied in this thesis, is controversially discussed: Some authors argue that it is something for "experienced workers" (ibid., p. 302). Others claim it to be unreliable (Webster et al., 2007). One argument against the fitting by eye is that one or more parameters of most models are non-linear and can only be determined by iteration (ibid.). Despite these challenges and limitations, kriging has the advantage that "[...] the estimated values have *minimum error* associated with them" (O'Sullivan et al., 2010, p. 309). Additionally, this error can be quantified by calculating its estimation variance (ibid.).

## 4.3 Methods applied for Testing

The interpolation model was tested with avalanche observations, for which an instability probability of 1 was assumed, and points of GPS tracks, where an instability probability of 0 was assumed. The two data sets were prepared similarly to contain points with only one aspect and one elevation information (see Section 3.2). All these points were interpolated, i.e. an instability probability was estimated for all of them. However, they were postprocessed differently: The GPS points that contained a single aspect were kept as such. For the points with a combined aspect, the two separately estimated instability probabilities for the aspect were averaged. For the avalanches, an instability probability was predicted for each point of the trajectory. If a trajectory contained a combined aspect, the average of the predicted $\rho_{max}$ value was taken. The final predicted $\rho_{max}$ value for each observed avalanche was calculated as the mean of the predicted $\rho_{max}$ value of its trajectory points (Winkler et al., 2021).

### 4.3.1 Kernel Density Estimation

In the discussion (see Section 6.5.2), the spatial distribution of avalanches and GPS points will be linked to the model implications. The aim is to find hot spots where the model is tested extensively but also to find out whether there are blind spots, i.e. areas that cannot be tested with the present data. To visualise spatial distribution, kernel density estimation (*KDE*) maps

of the Swiss Alps were produced for each data set and available winter. The same *KDE* input variables were used throughout: A 1 km x 1 km grid, a search radius/bandwidth of 20 km and a quartic/biweight kernel type (default in *kde_hotspot* function, package *sfhotspot*). The bandwidth of 20 km was determined by experimentation (O'Sullivan et al., 2010): It covers big valleys such as the Bedretto. However, it is much smaller than the value calculated by the bandwidth estimator built into the *kde_hotspot* function in R (Venables et al., 2002).

### 4.3.2 Event Ratio

The predicted instability probabilities of the avalanche observations can be related to the ones of the GPS points, respectively, the ones of the Swiss Alps by calculating the event ratio $R$ (Grímsdóttir et al., 2006; Techel et al., 2022; Winkler et al., 2021). The nominator contains the number of events at stake, i.e. the observed human-triggered avalanches; the denominator consists of all the prediction points, which are the avalanche observations *plus* the GPS points:

$$R = \frac{\text{events}}{\text{events} + \text{non-events}} = \frac{\text{observed human-triggered avalanches}}{\text{observed human-triggered avalanches} + \text{GPS points}} \tag{4.2}$$

A similar ratio can be calculated using the same nominator (predicted $\rho_{max}$ values of the observed human-triggered avalanches), but the denominator consists of all the predicted instability points on the 1 km x 1 km grid in the Swiss Alps. The corresponding formula is:

$$R = \frac{\text{events}}{\text{events} + \text{non-events}} = \frac{\text{observed human-triggered avalanches}}{\text{observed human-triggered avalanches} + \text{grid points in the Swiss Alps}} \tag{4.3}$$

In both cases, the ratio $R$ is calculated and plotted for a bin size of 0.05 of the instability probability.

# 5 | Results and Interpretation

This chapter presents the results of the different interpolation methods by distinguishing again between validation and testing results. After the results of the $k$ nearest neighbours (*knn*) and ordinary kriging (*OK*) interpolation, which are assessed visually, the kriging with external drift (*KED*) model is validated. It resumes at Q9 in the decision tree outlined in Chapter 4 and ends with the decision for a final model. The testing part is structured according to the data used: avalanche observations for high probabilities of instabilities and points from GPS tracks for low probabilities. The results from testing with the observed avalanches (see Section 5.3) are first analysed over the four winters before examining single avalanches from each winter in detail. The results of the testing with the GPS points only concern two winters (see Section 5.4). To conclude, the two different data sets are combined and compared in event ratio plots.

## 5.1 Validation of the *knn* Model

Figure 5.1 gives an example of the *knn* interpolation for four days and aspects. We can see that the interpolation is relatively coarse, assigning a low instability probability to the big valleys. The smaller or more narrow valleys are hardly distinguishable. The transition of the instability from low to high elevations can be abrupt, e.g. in the case of the Rhone Valley on 7 February 2022, for the aspects north and east. High instability areas, even for the aspect north, stabilise surprisingly quickly, e.g. within two days. The maps further show that if the density of control points is low, as in the Central Plateau, the interpolated values do not vary anymore (Grekousis, 2020).

## 5.2 Validation of the Kriging Models

### 5.2.1 Ordinary Kriging (*OK*)

The interpolation with ordinary kriging (*OK*) as illustrated for a single day and aspect in Figure 5.2 is even coarser than the *knn* maps since the elevation was not considered. Instead, a constant mean was assumed. The *OK* map shows an abrupt transition from low (in blue) over medium (yellow) to high instability (in red). Due to its coarseness, the *OK* method will not be pursued further.

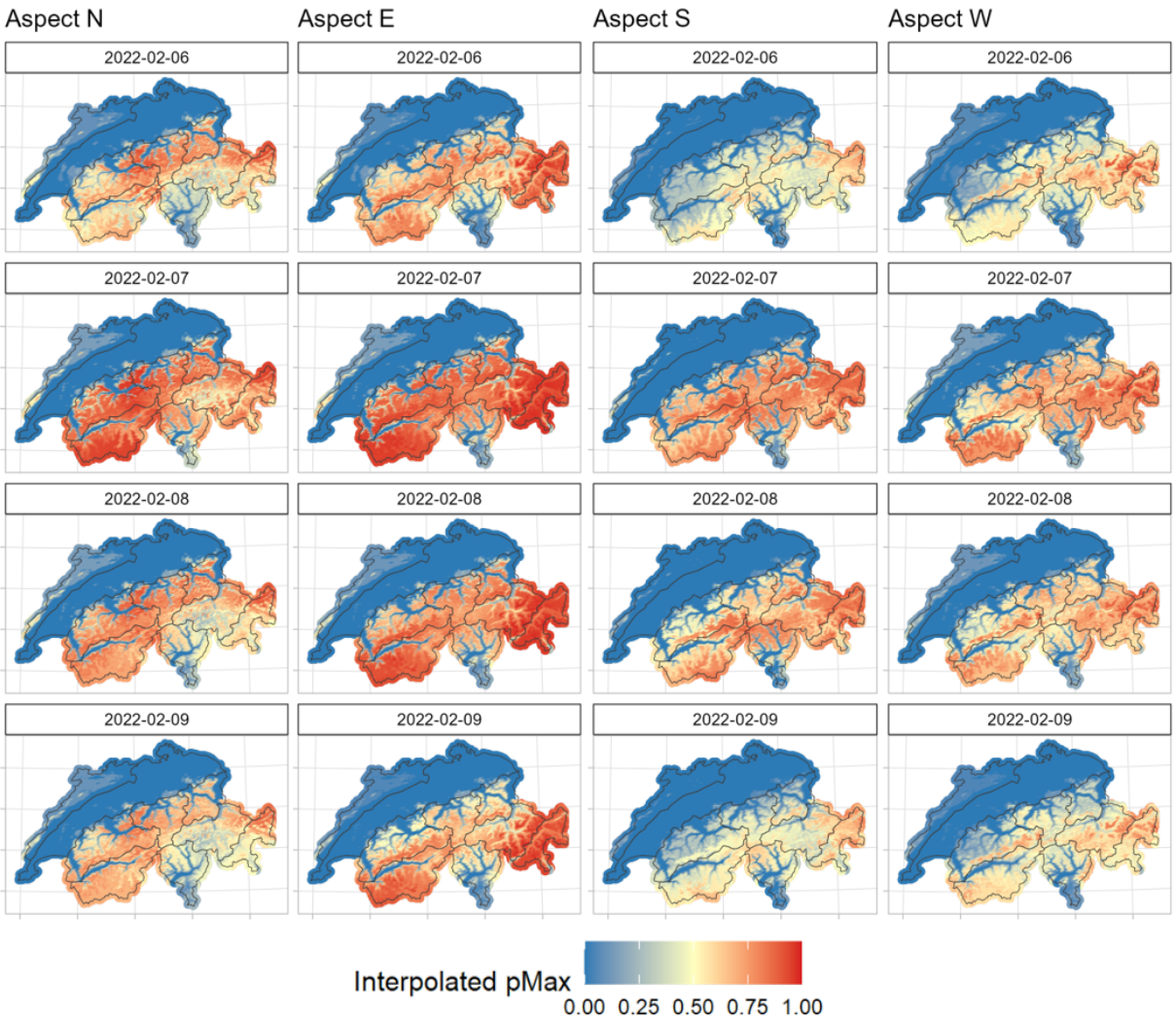


**Figure 5.1:** *knn* interpolation maps for 6 to 9 February 2022. Low $\rho_{max}$ values (blue) stand for a stable snowpack, and high $\rho_{max}$ values (red) for an unstable one.

### 5.2.2 Kriging with External Drift (*KED*)

In Chapter 4, I decided to try two theoretical variogram functions for the *KED* model, the spherical (Sph) and Matérn, M. Stein's parameterisation (Ste). Both use the average factors of the high variation sample as weights. The two functions performed similarly when applied to the three samples with high, medium and low variation. Both could be used for the final model. However, I limit myself to one model and choose the Sph function with the averaged factors of the high variation sample (see Table 5.1). In the following, I thus concentrate on the results of this model.

While the mean error (*ME*) of the Sph model was almost zero for all three samples, the root mean squared error (*RMSE*) and the correlation between observed and predicted values varied depending on the sample (see Figure 5.3). Despite the weights of the high variation sample used for the model, the *RMSE* is higher and more dispersed in the high than in the mid or low sample. For some AWSs (BEV2 in Valletta da Bever or BOG2 in Valle di Bosco Gurin), predicting a

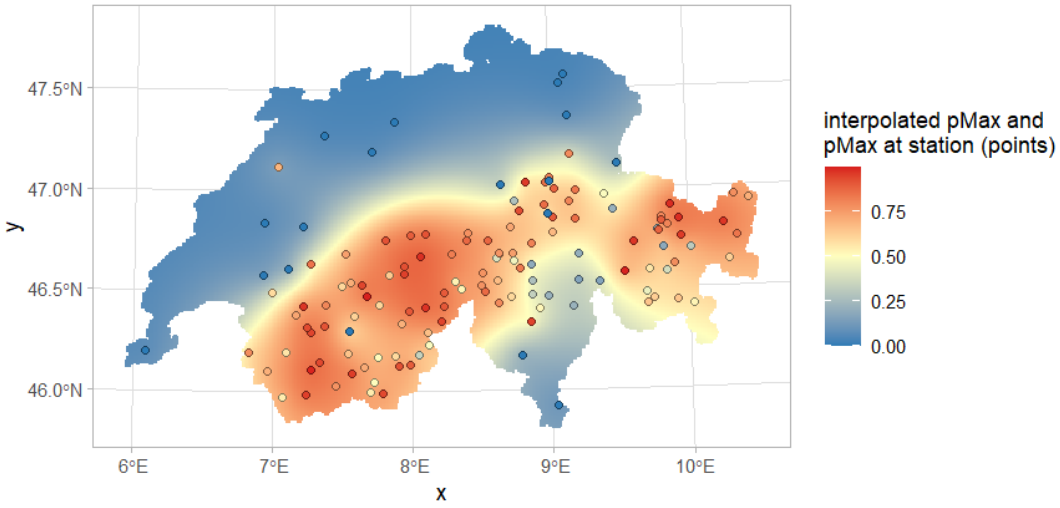


**Figure 5.2:** Interpolation map produced with *OK*. The $\rho_{max}$ value of the AWSs used as input is placed on the interpolation map. However, the stations do not necessarily have the same elevation as the underlying 1 km x 1 km grid cell used for the interpolation.

$\rho_{max}$ value with data from surrounding stations is difficult as they are exposed to strong winds which erode the snowpack simulation (F. Techel, SLF, personal communication, 26 March 2024). However, since the high variation days were captured within this high sample, the two statistics show extreme values in the sense that if the model is applied to other data, the *RMSE* should be in the same range or even lower (see Section 5.2.4). The correlation is relatively high for the high and medium variation samples. However, the second quartile in the low variation sample is lower than in the high and medium samples. The days and aspects contained in this sample could be an explanation for this: The low variation sample contains the 1 May 2021 and 2022, each with the aspects S and W, where the number of AWSs is much smaller than on the days before (38-88 instead of $> 100$). Furthermore, and maybe related to the lower number of AWSs: The observed $\rho_{max}$ values for 1 May 2021 and 2022 range between 0.2 and 0.55, while the predicted ones are all around 0.4. The cross-validation statistics for the three samples using the Ste model can be found in the Appendix; see Figure A.1.

### 5.2.3 Cross-Validation: 90/10 Train-Test Split (all Training Data)

The performance of the interpolation model was evaluated with cross-validation on all the training data by applying a 90/10 train-test split as described in Chapter 4. The histogram of the

**Table 5.1:** Determined values and factors/weights for parameters of the final model.

| **parameter** | **value** | **factor** |
|---|---|---|
| partial sill | max(semivariance) | 0.5375 |
| range | max(distance) | 0.4100 |
| nugget | mean(semivariance) | 0.4900 |

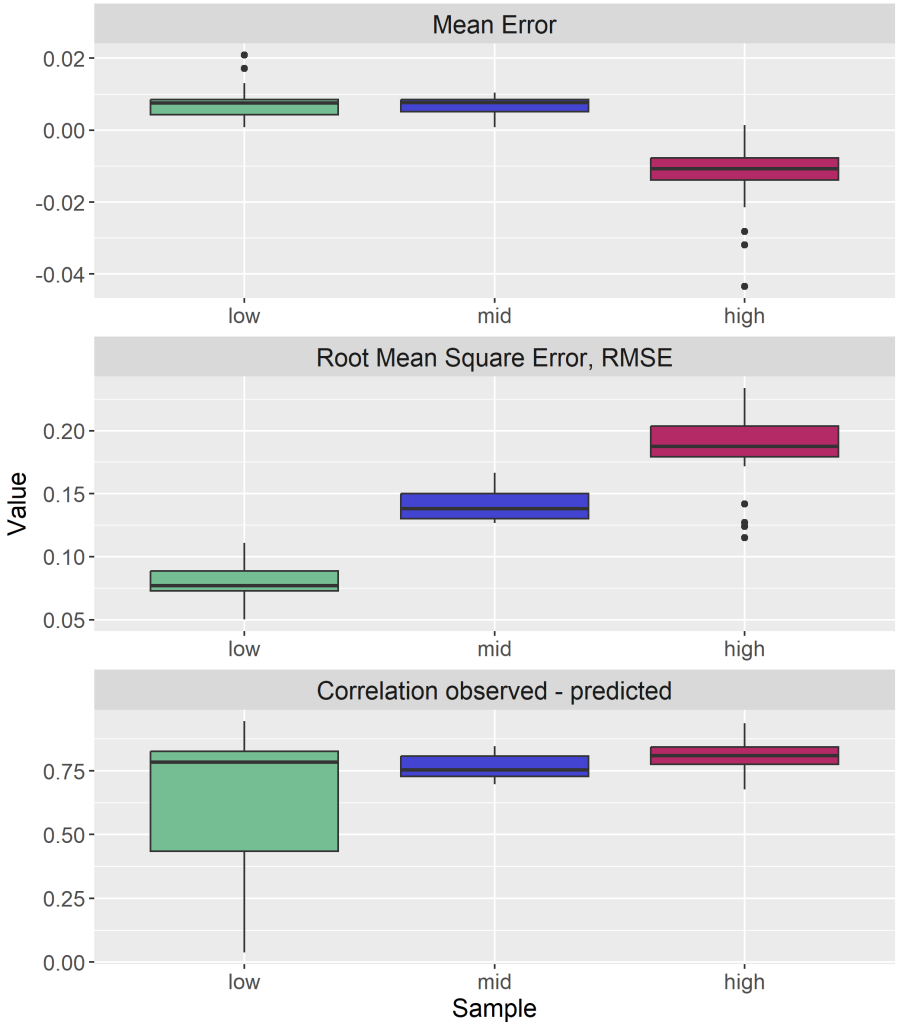


**Figure 5.3:** Boxplots of the cross-validation statistics for the spherical model, grouped by sample (low, medium and high variation).

residuals of the cross-validation, grouped by aspect (see Figure 5.4), shows that the width of the distribution is the same. The *RMSE* of the four aspects is also very similar: 0.16 for N and W; 0.15 for E and S. Thus, the prediction is equally good for all aspects.

### 5.2.4 Ten-Fold Cross-Validation (all Training Data)

The ten-fold cross-validation of all the training data resulted in similar results for all the aspects (see Figure 5.5): Generally, the mean error (*ME*) is around 0. Thus, the predictions are not biased (Holbert, 2024). The root mean squared error (*RMSE*) is between 0.1 and 0.2. Compared to the *RMSE* of the high, medium and low variation sample, the *RMSE* did not increase. The correlation between the observed and predicted instability is high (around 0.7-0.8). We can see that some days and aspects from the sample with low variation are now – taking into account all the training data – to be considered outliers.

When plotting the root mean squared error (*RMSE*) over time according to winter and aspect

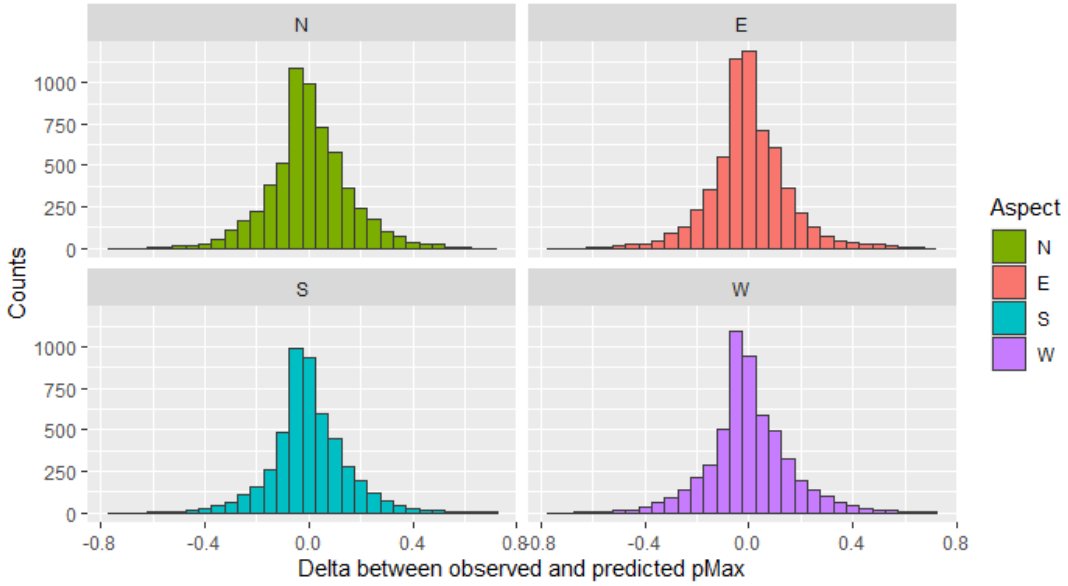


**Figure 5.4:** Residuals from the cross-validation with the 90/10 train-test split of the Sph model, plotted according to aspect. The total number of data points is 22'405; the numbers according to aspect are N 5982, E 6063, S 4932 and W 5428.

(see Figure A.2), we observe that it varies more depending on the date than on the aspect, and it decreases towards spring in the three winters. Due to these findings, it is reasonable to use the same parameterisation for the four aspects.

## 5.3 Testing the Model with Avalanche Observations

The model was tested with four winters of avalanche observations. As the instability predictions at the location of the weather stations from the first three winters were used to train the model and to predict the instability at the location of the avalanches, only the last winter can be considered entirely unseen by the model.

When comparing the frequency of the predicted $\rho_{max}$ values at the location of the observed avalanches (see Figure 5.6), the pattern of the four winters is similar despite the different number of observed avalanches per winter. The model has not seen the data from the last winter but predicts a similar distribution of avalanches as in the training winters, which suggests that there is no overfitting. All four histograms are negatively skewed, i.e. with increasing $\rho_{max}$ value, more avalanches were observed. However, at the highest $\rho_{max}$ values, the number of avalanches decreases sharply. Possible reasons can be found in Chapter 6. The most avalanches were observed in the winter of 2020/21: Almost 800, compared to 340, 503 and 661 in the other three winters. In this winter, the increase in the number of observed avalanches with higher $\rho_{max}$ values is most pronounced. Winter 2020/21 stands out as well when looking at the combined boxplot (see Figure 5.7): It shows higher Q1, median and Q3 values for the $\rho_{max}$ values of the observed avalanches. All in all, the four boxplots are very consistent. Therefore, the model

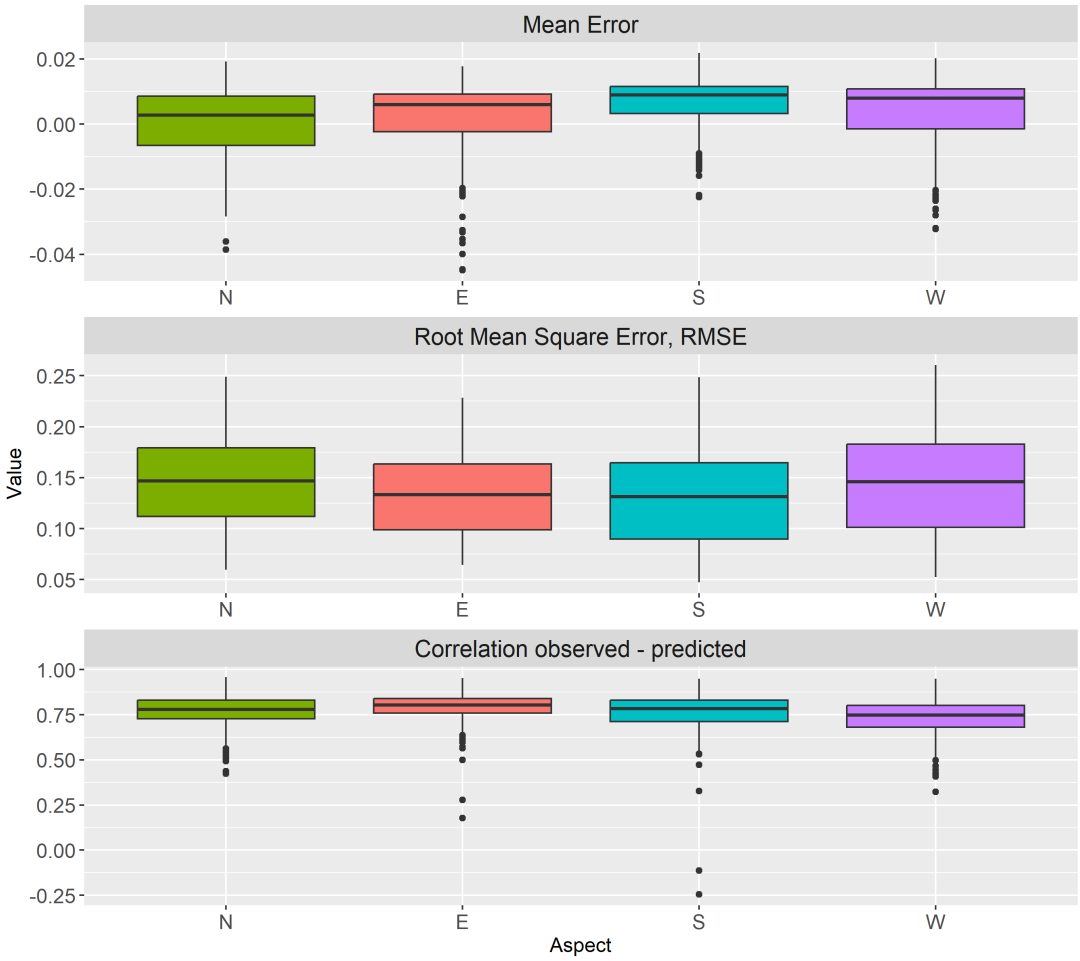


**Figure 5.5:** Boxplots of the ten-fold cross-validation statistics of all the training data for the Sph model, grouped by aspect.

predicts reasonable instability values for most avalanches, and its performance is consistent even on unseen data, as in the winter of 2022/23.

The four winters are also consistent regarding the elevation of the observed avalanches (see Figure 5.8). The interquartile range and the median hardly differ between the four winters. The median elevation over the four winters is between 2350 and 2470 m a.s.l. Furthermore, this boxplot reveals that avalanches can occur at all elevations but are concentrated between 2100 and 2700 m a.s.l.

Coming back to the histogram and the boxplot of the predicted $\rho_{max}$ values of all four winters (see Figures 5.6 and 5.7), we see that for some of the observed avalanches, a very low instability was predicted. They occurred in a terrain that can be classified as relatively stable. In the following, these avalanches are analysed for each winter. A $\rho_{max}$ value of 0.2 or lower was taken as a threshold to filter out the avalanches. This resulted in 15 avalanches, eleven of which were size one and four were size two. For better readability, only a few of the corresponding figures can be found in this chapter, while the majority was moved to the Appendix A.3.


**Figure 5.6:** Histogram of the predicted instability at the location of observed avalanches for the four winters.

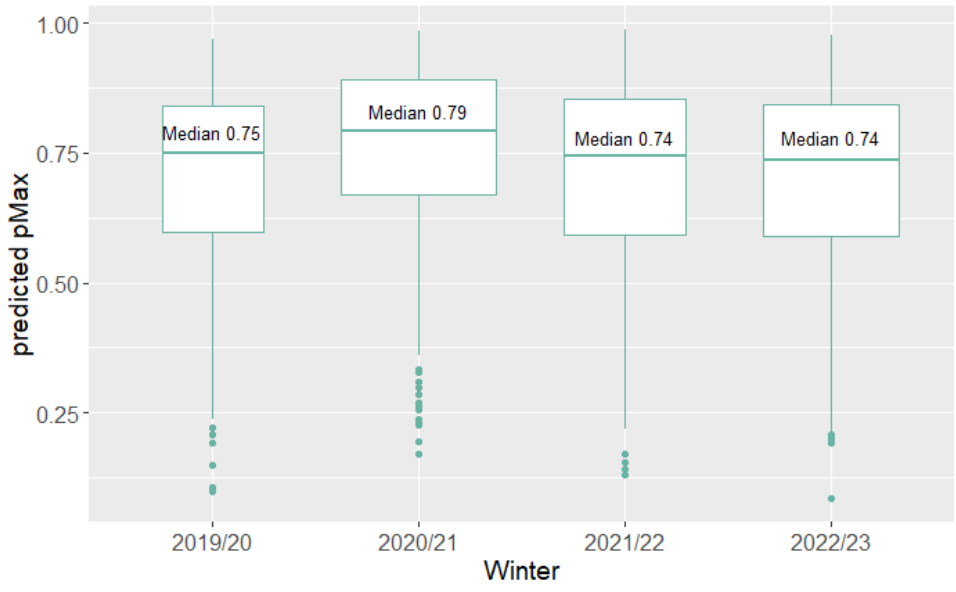


**Figure 5.7:** Boxplot of the predicted instability at the location of observed avalanches for the four winters. The width of the boxes is proportional to the square root of the number of observations per winter.

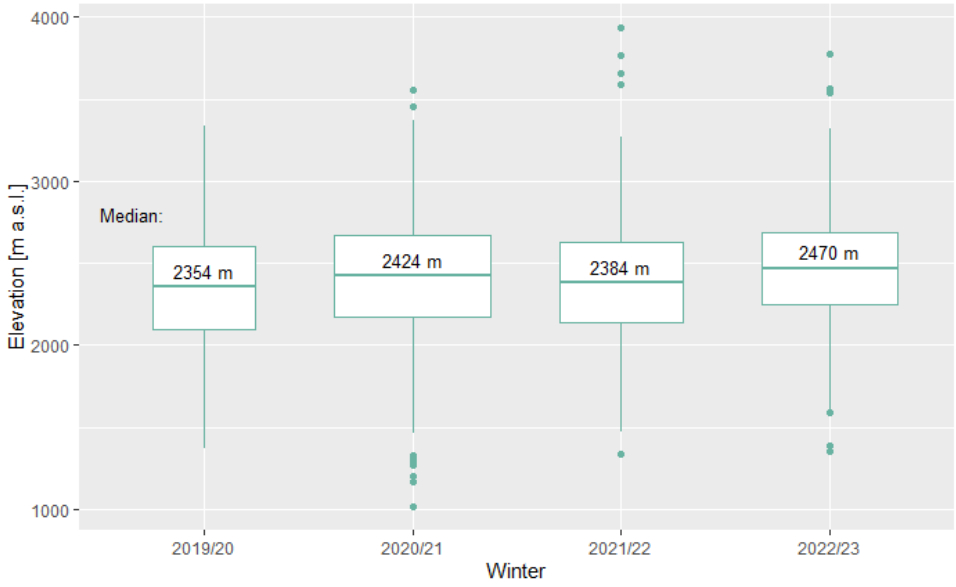


**Figure 5.8:** Boxplot of the elevation at the location of observed avalanches for the four winters. The width of the boxes is proportional to the square root of the number of observations per winter.

### 5.3.1 Winter 2019/20

In the first winter, a $\rho_{max}$ value of 0.2 or smaller was predicted for five avalanches. Their $\rho_{max}$ values range from 0.10 to 0.19, and their locations are all below an elevation of 1930 m a.s.l. The avalanche with the lowest $\rho_{max}$ value (0.1) was triggered on 15 January 2020 to the east of Gurschenstock in the Unteralp Valley, close to Andermatt (coordinates: 692377.6, 162891.4), aspect north. The slope angle is between 30° and 35° according to the map of the slope classes over 30° (Federal Office of Topography swisstopo, 2023b), thus avalanche terrain as Figure 5.9 shows. For the surrounding stations, relatively low $\rho_{max}$ values were predicted for that date and aspect (see Figure 5.10). The avalanche is mentioned in the weekly report of the SLF from 10 to 16 January 2020 as the only human-triggered dry-snow avalanche in those days (WSL Institute for Snow and Avalanche Research SLF, 2020). The low predicted $\rho_{max}$ value of the avalanche could be explained by the elevation of the avalanche (1754 m), which is lower than all the surrounding stations. If their already low $\rho_{max}$ values were interpolated respectively downscaled to 1754 m, the location of the avalanche ends up with an even lower $\rho_{max}$ value than the surrounding stations. In this case, an error in the data processing or model setup can be ruled out.

For the same date, but with a northeast slope aspect, another avalanche was observed just above, at 1808 m a.s.l., with a $\rho_{max}$ value of 0.11. However, the reasoning for the low predicted $\rho_{max}$ value could be the same as for the first avalanche. In this case, an error in the data processing or model setup can also be ruled out.

Two of the remaining three avalanches were observed in the Entschligental on 25 January 2020 but at different elevations and aspects. For these two avalanches, the low predicted $\rho_{max}$ values

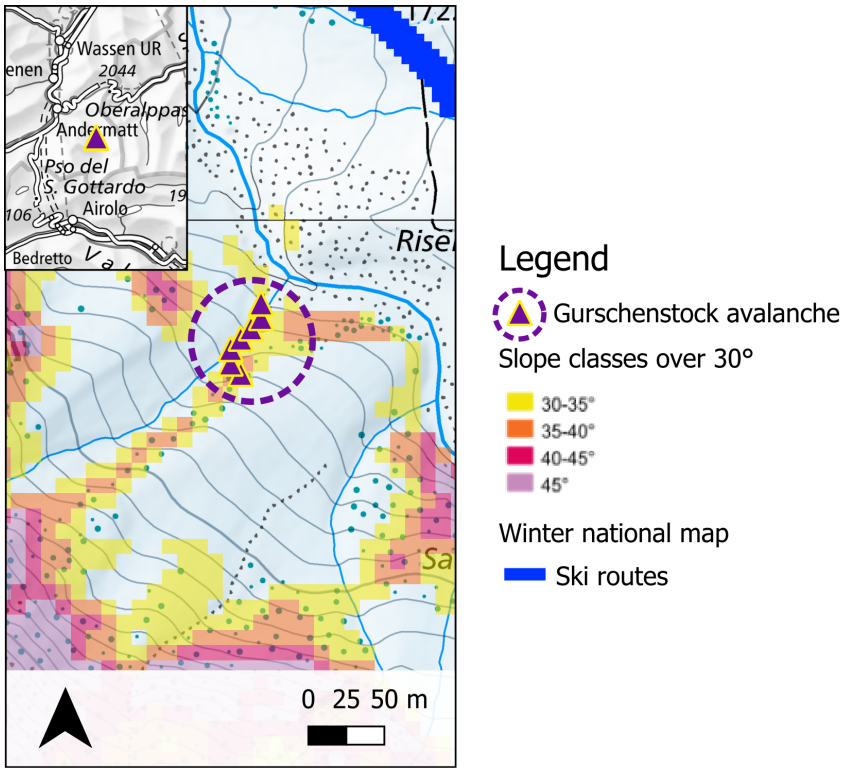


**Figure 5.9:** Location of the trajectory of the avalanche to the east of Gurschenstock in the Unteralp Valley with a very low $\rho_{max}$ value. The main map also contains the ski routes (blue lines) and the slope classes over 30°.

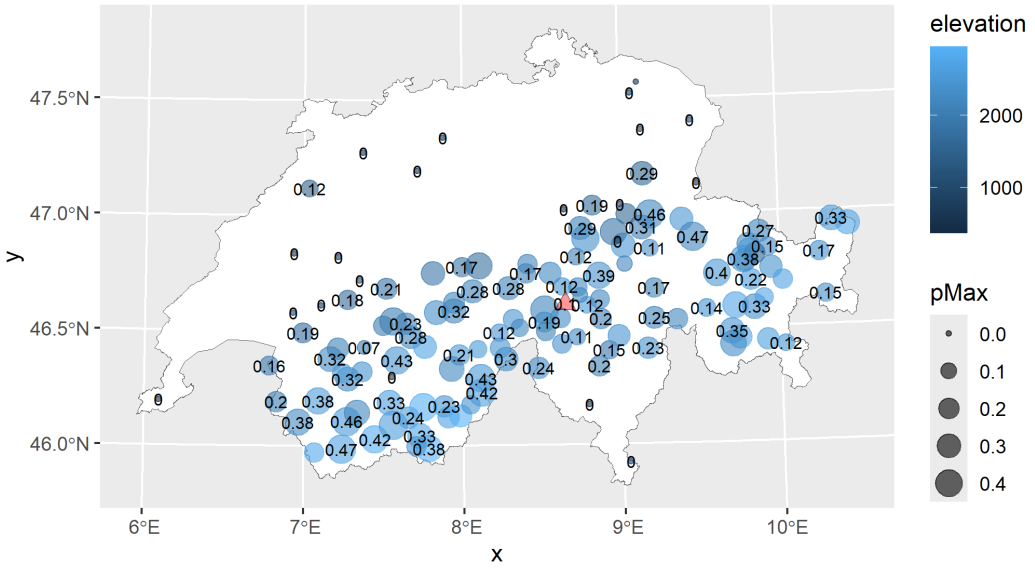


**Figure 5.10:** Instability predictions at the locations of the AWSs for 15 January 2020, aspect N. The red triangle locates the Gurschenstock avalanche.

(0.1 and 0.19) could also be explained by the relatively low $\rho_{max}$ values at the surrounding stations, which are located at higher elevations. In this case, an error in the data processing or model setup can also be ruled out.

The last of the five avalanches with a low predicted $\rho_{max}$ value was observed on 11 January 2020 ($\rho_{max}$ of 0.15, aspect north) on Lake Sils (coordinates: 777632.8, 144021.6). Hence, there must have been an error in reporting the observed avalanche.

### 5.3.2 Winter 2020/21

In the second winter, a $\rho_{max} \leq 0.2$ was predicted for three avalanches. Their $\rho_{max}$ values range from 0.17 to 0.19. Their elevations are below 2070 m a.s.l. On 27 January 2021, an avalanche was observed at 1313 m a.s.l. between Hasenmatt and Gitziflue close to Solothurn. Avalanches in the Jura are seldom: Only 6 out of the total 2300 avalanches observed in the four winters are located in the Jura. Furthermore, there are not enough stations in this area for the model to make a reliable prediction.

The second avalanche, with a predicted $\rho_{max}$ value of 0.17, was observed on 10 January 2021 at an elevation of 1687 m in the region Schwäfelberg in the Bernese Alps (coordinates: 598862.8, 172262.7). The release point of the avalanche is not in typical avalanche terrain, but further up (starting at around 1720 m), the slope angle is between 30° and 35° (Federal Office of Topography swisstopo, 2023b). It could be a remotely triggered avalanche where the release point was estimated. Another difficulty for this avalanche is its location at the border of the Alps to the Central Plateau. Not many stations are available in the direction of the Central Plateau (to the west, north and northeast). The closest ones in this direction all have a zero $\rho_{max}$ value. Most stations to the east and south have a $\rho_{max}$ value smaller than 0.3. There is no clear pattern for the latter, i.e. the $\rho_{max}$ value does not necessarily increase with elevation.

The third avalanche, with a $\rho_{max}$ value of 0.19, was observed close to Simplonpass (coordinates: 643542.8, 120942.0) at an elevation of 2069 m, aspect east. It is located in typical avalanche terrain, with a slope angle between 35° and 40° (ibid.). At the surrounding stations, a $\rho_{max}$ value of 0.3 to 0.4 was predicted. However, all these stations are at higher elevations than the avalanche. Therefore, the predicted $\rho_{max}$ value of this avalanche was also downscaled. According to the dataset, the avalanche was triggered remotely. In this case, an error in the data processing or model setup can also be ruled out.

### 5.3.3 Winter 2021/22

Five avalanches had a predicted $\rho_{max}$ value of 0.2 or smaller in the third winter. Their $\rho_{max}$ values range from 0.13 to 0.17. They are all located at an elevation below 1780 m. The avalanche with the lowest $\rho_{max}$ value (0.13) was released on 12 March 2022 and is located in the area called Loch, close to Elm, at an elevation of 1624 m, with aspect northwest (coordinates: 728886.4, 193455.5).

The release point is on an official ski touring track (Federal Office of Topography swisstopo, 2023a), and the terrain is very steep, 35°-40° (Federal Office of Topography swisstopo, 2023b). The predicted $\rho_{max}$ for the avalanche is the mean of the trajectory points for the two aspects north and west. A higher $\rho_{max}$ value was predicted at the surrounding stations for the aspect north than for west. Furthermore, the predictions for the $\rho_{max}$ value at the stations with aspect west are still higher than the $\rho_{max}$ of the avalanche. However, the stations are at a higher elevation than the avalanche. Thus, the predicted $\rho_{max}$ value for the avalanche was also downscaled and an error in the data processing or model setup can be ruled out.

The avalanche with the second lowest $\rho_{max}$ value (0.14) was released on 11 March 2022. It is located below the Zanaihörner (coordinates: 751598.4, 202637.2) at an elevation of 1599 m, with aspect north. The terrain is up to 45° steep. At the same date and aspect, but 60 m higher up (1661 m) in terrain that is less than 30° steep (ibid.), another avalanche was observed (coordinates: 751609.1, 202515.1). It had a predicted $\rho_{max}$ value of 0.15. The two avalanches are located at the border of the network of weather stations. The number of stations is thinning out towards the north and northeast. There are two stations close by, one to the northwest at 2469 m at the Wildsee (TAM2), which predicted a $\rho_{max}$ value of 0.48, while the other one (TAM3), which is 300 m lower, only predicted 0.17 for that date and aspect. Thus, the predicted $\rho_{max}$ value of the two avalanches fits into the surrounding AWS pattern.

The third avalanche, in terms of a low $\rho_{max}$ value (0.14), occurred on 13 March 2022 and is located below Piz Tgietschen at an elevation of 1773 m, aspect east (coordinates: 724034.4, 166893.1). The release point is located on an official ski touring track where the slope is less than 30° steep (Federal Office of Topography swisstopo, 2023a,b). However, above the release point, the terrain steepens up. Of the two closest weather stations, one is located at a higher elevation (2064 m), predicting a $\rho_{max}$ value of 0.28, and the other is lower (1245 m), predicting zero. Thus, the predicted $\rho_{max}$ value for the avalanche fits into the surrounding AWS pattern.

The fifth avalanche with a low $\rho_{max}$ value (0.17) in this winter was triggered on 6 March 2022 at an elevation of 1716 m, aspect east, in the area of Guillon, below the Arête du Dardeu (VS) (coordinates: 562451.8, 115571.3). The release point is located in consistently steep terrain of 35°-40° (Federal Office of Topography swisstopo, 2023b). The surrounding stations, most of them at higher elevations ($>$ 2000 m), predicted a $\rho_{max}$ value of 0.31 or higher, except for the station in Les Diablerets (1190 m), which predicted zero instability. Thus, the predicted $\rho_{max}$ value for the avalanche fits into the surrounding AWS pattern.

### 5.3.4 Winter 2022/23

In the last of the four winters, only two avalanches were assigned a low $\rho_{max}$ value. The lowest $\rho_{max}$ value (0.09) stems from an avalanche that occurred on 3 February 2023, with aspect east, between Alt St. Johann and the Chäserrugg just below the rope of the cable car from Espel to Stöfeli (coordinates: 742438.3, 227170.9) at an elevation of 1356 m a.s.l. When looking at

the map (see Figure 5.11), it is a rather unusual location for an avalanche to be triggered as the terrain is not steep (< 30°) and there is a small forest above (Federal Office of Topography swisstopo, 2023b). A possible reason for this low $\rho_{max}$ value could be the low density of AWSs in this area. Another reason could be an error, e.g. in the coordinates, when recording the avalanche. When looking at the predictions of the nearby stations for that date and aspect (see Figure 5.12), we see that at the two closest stations to the avalanche (point in red), a $\rho_{max}$ value of zero was predicted.

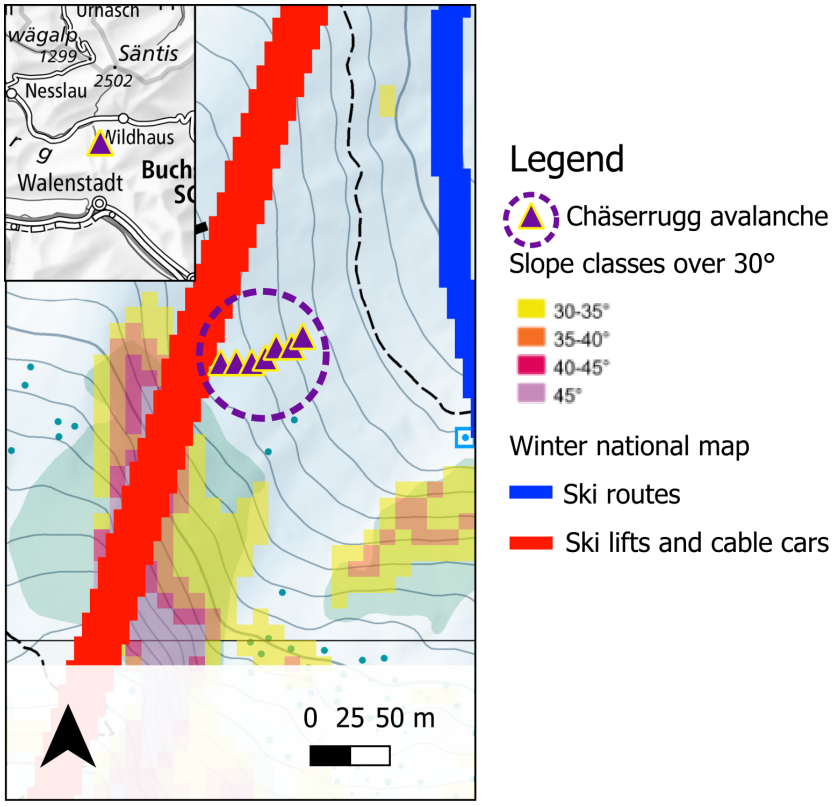


**Figure 5.11:** Location of the trajectory of the avalanche close to Chäserrugg with a very low $\rho_{max}$ value. The main map also contains the ski routes (blue line), the ski lifts and cable cars (red line) and the slope classes over 30°.

When consulting the time series of the $\rho_{max}$ value and the snow height at the station in Amden (AMD2) (see Figure A.3 in the Appendix), the drop to zero in the snow height and the $\rho_{max}$ value on 2 February 2023 comes as a surprise. Possible explanations could be an error in the snow height measurement at the station AMD2, a prediction error of the SNOWPACK model or a combination of both.

The avalanche with the second lowest $\rho_{max}$ value (0.19) was triggered on 13 February 2023 on the northeastern slope of Piz Ault (2454 m), close to the Oberalppass (coordinates: 705580.6, 168418.4). The slope angle at the release point is between 30 and 35° (ibid.). An avalanche in this terrain is possible (see Figure A.4 in the Appendix). A $\rho_{max}$ value of 0.35 or higher was predicted at all the surrounding stations except one. However, for the closest station to the avalanche, PUZ2, in the area of Puzzeta sura in the community of Medel, a $\rho_{max}$ value of zero is predicted for this date and aspect (see Figure A.5 in the Appendix). This could explain the

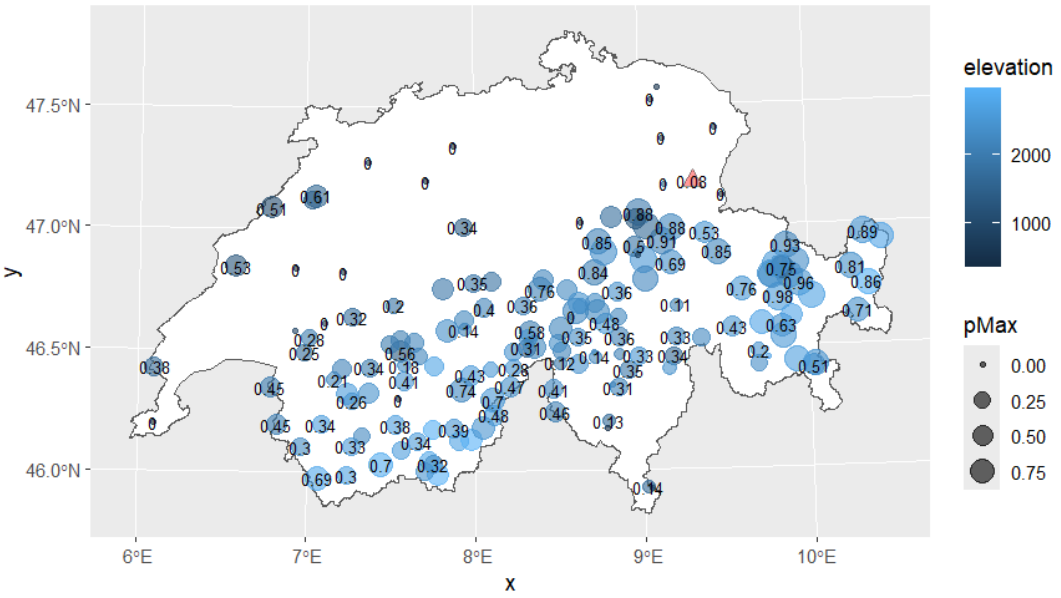


**Figure 5.12:** Instability predictions at the locations of the AWSs for 3 February 2023, aspect E. The red triangle locates the Chäserrugg avalanche.

low $\rho_{max}$ value of the avalanche. As for the station in Amden (AMD2), the time series of the station PUZ2 (see Figure A.6 in the Appendix) indicate a sudden drop in the snow height and the $\rho_{max}$ value at the date of the avalanche.

### 5.3.5 Similarities and Differences between the Winters

Regarding the avalanches with a $\rho_{max}$ value of 0.2 or lower, they share some characteristics: Most of them fit into the general pattern of the predicted $\rho_{max}$ values at the surrounding stations. Thus, they do not question the model's performance in general. Often, they are concentrated around a week or ten days, except for the winter of 2020/21. Even if they are concentrated timewise, they do not cluster spatially, i.e. the low predicted $\rho_{max}$ cannot be explained by one or a few defective stations. Yet, the low predicted $\rho_{max}$ values can be found mostly between 1000 and 2000 m a.s.l.; there is just one avalanche with a low predicted $\rho_{max}$ value above 2000 m (at 2069 m). Other reasons for a low $\rho_{max}$ value of an avalanche are errors when recording the avalanches, as it may be challenging to determine the exact location, especially for remotely triggered avalanches, where the release point is far from the observer. Other explanations for low $\rho_{max}$ values at the location of an avalanche could be errors in the snow height measurement, in the snowpack simulation and thus in the prediction of the $\rho_{max}$ value at an AWS. For others, the reasoning is more complex, e.g. avalanches at the border of the Central Plateau to the Prealps, where the model had difficulties predicting instability. It turned out that the winters with the most avalanches (2020/21 and 2022/23) had the fewest avalanches with low $\rho_{max}$ values. It would be worth investigating whether there is a relation between the number of available data points as input, the number of avalanches, and the number of avalanches with a predicted $\rho_{max}$ value of 0.2 or smaller. However, to do so, data from more winters is necessary.

## 5.4 Testing the Model with GPS Points (ARPD)

The model was tested with GPS points recorded during the winters of 2019/20 and 2020/21 and stemming from the Avalanche Risk Property Dataset (ARPD) (Schmudlach, 2022). It must be remembered that the instability predictions at the location of the weather stations from the first three winters were used to train the model and again to predict the instability at the location of the GPS points. However, the model did not see the GPS points before the testing. The predicted instability probabilities at the location of the GPS points of the two winters show several similarities. The boxplot of the slope angles (starting at 20° due to the filtering applied) (see Figure 5.13) shows a very similar median of 28° for both winters. The interquartile range ends before 35°. I thus deduce that backcountry skiers prefer less steep, safer terrain and that their behaviour is defensive. In both winters, the outliers start around 45°. In the first winter, they reach higher slope angles than in the second winter. The points with slope angles $\geq 45°$ are outliers in Figure 5.13 as these points are too steep for most people. Some are located in or between steep rock walls, which could hint at GPS location problems.

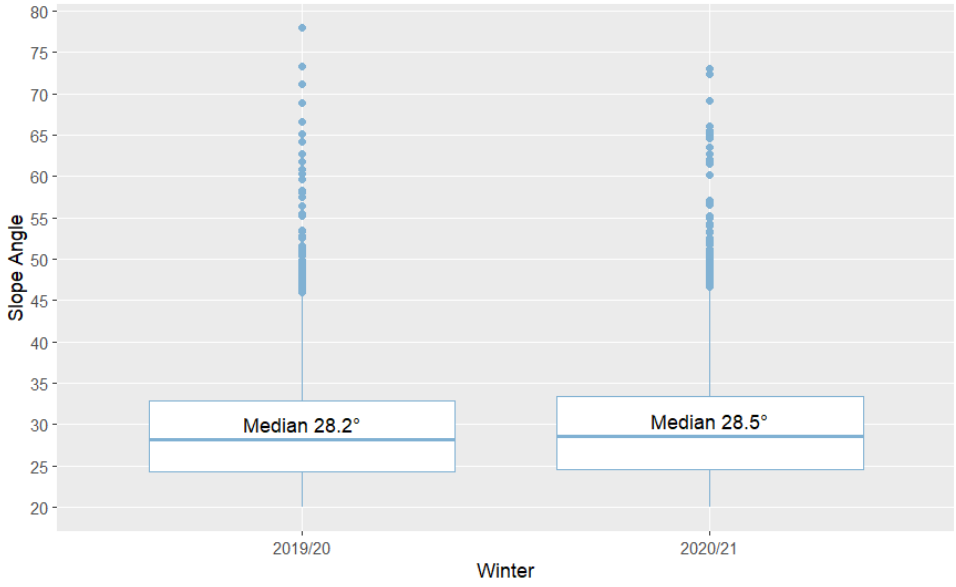


**Figure 5.13:** Boxplot of the slope angles of the GPS points of the two winters.

Similarities can also be found in the boxplot of the $\rho_{max}$ values in Figure 5.14: In both winters, 75% of the GPS points have a predicted $\rho_{max}$ value $\leq 0.52$. The distribution of the predicted pMax is independent of the winter, with quartiles differing by at most 0.02. Thus, the majority of the people are defensive out in the backcountry.

When looking at the histogram of the predicted $\rho_{max}$ values (see Figure 5.15), both winters show a positive skew: The counts rise steeply until the maximum at 0.23 (winter 2019/20; please note that the bar at a predicted $\rho_{max}$ of 0.17 has just one count less than the one at 0.23) respectively 0.25 (winter 2020/21) and then they decrease slowly until 1, showing some local maxima in both years.

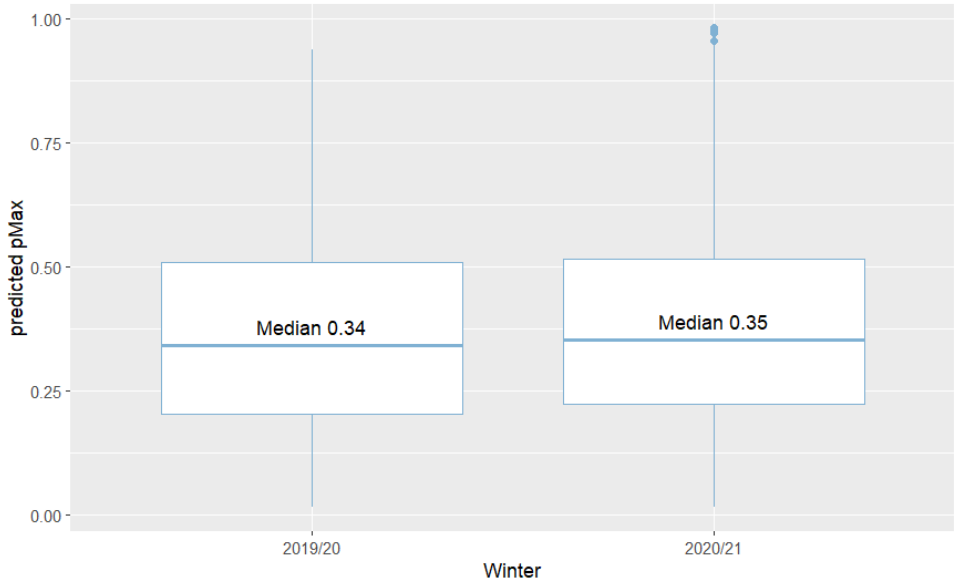


**Figure 5.14:** Boxplot of the predicted $\rho_{max}$ values at the location of GPS points: winter 2019/20 vs winter 2020/21.

When plotting the variability grouped by aspect, the two winters are again very similar regarding the median and spread of their predicted $\rho_{max}$ values (see Figure 5.16). Generally, the predicted $\rho_{max}$ values for slope aspects southeast, south, southwest, west and northwest have a lower median and cover lower instability probabilities than the other aspects. The difference between the aspects is more pronounced in the second winter (2020/21) than in the first.

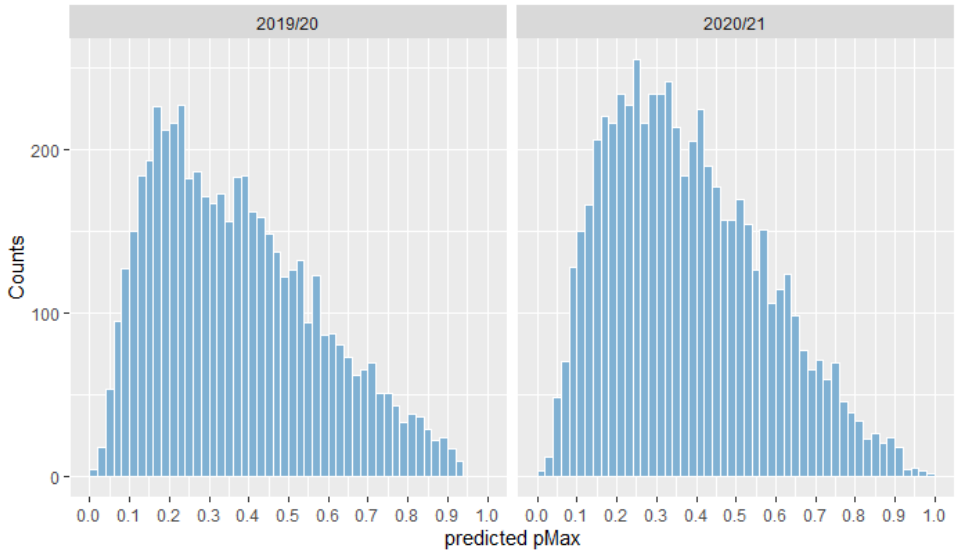


**Figure 5.15:** Histogram of the predicted $\rho_{max}$ values for the first two winters (2019/20 and 2020/21) at the location of the GPS points (filtered according to $TI > 0.25$ and $SA \geq 20$).

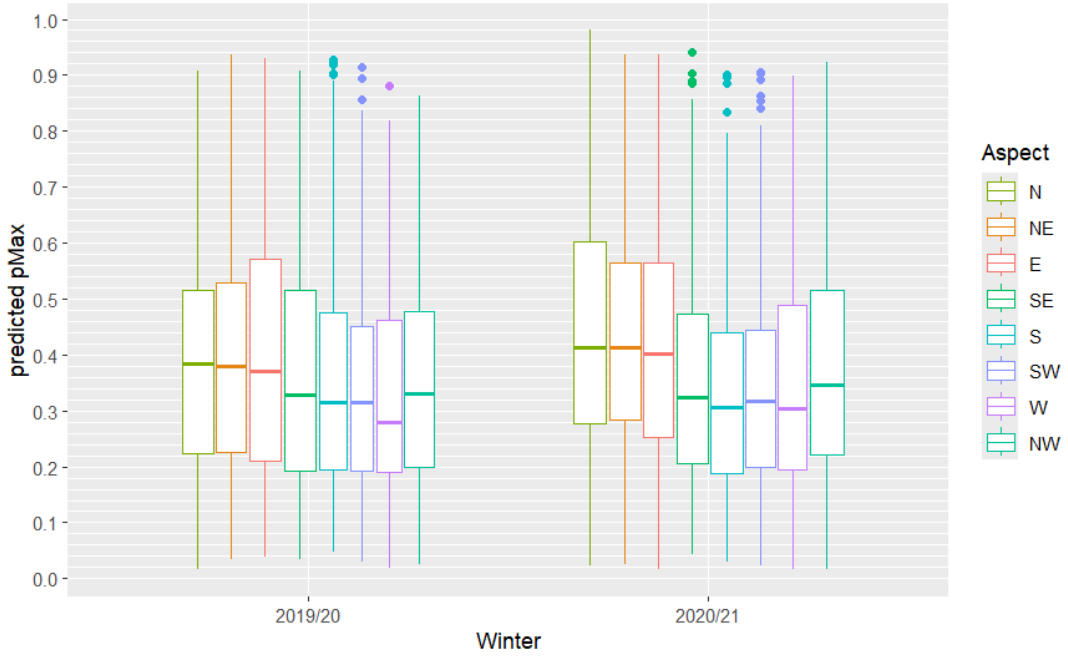


**Figure 5.16:** Boxplot of the predicted $\rho_{max}$ values at the location of GPS points, grouped by winter and aspect.

## 5.5 Running the Model on the Swiss Alps

To set the predicted $\rho_{max}$ values of the avalanche observations and the GPS points in relation to the terrain, the model was run on a grid (1 km x 1 km) covering the Swiss Alps. In the following, the predicted $\rho_{max}$ values of the four winters will first be compared in terms of their distribution and frequency. Later, the interpolated maps will be described qualitatively to discern patterns.

### 5.5.1 Comparison of the four Winters

The histogram of the $\rho_{max}$ values of the predicted points in the Swiss Alps (see Figure 5.17) contains much more data than the avalanche observations or the GPS points, resulting in smoother histograms. They are positively skewed and very similar in shape. Again, the winter of 2020/21 is an exception due to the slight rise in the frequency of high $\rho_{max}$ values (0.85-0.95). The tail of this distribution is thus heavy. Since the amount of data points in the Swiss Alps is the same in the four winters, the heavy tail in winter 2020/21 goes along with the lowest maximum of 1.3 million $\rho_{max}$ values between 0.02 and 0.04, while the first winter (2019/20) has the highest maximum ($>$ 1.9 million). The other two winters reach a maximum of 1.5 respectively 1.6 million.

The boxplot grouped by winter (see Figure 5.18) shows that the predicted $\rho_{max}$ values spread over the full range [0,1]. While the $\rho_{max}$ values close to 0 are part of the first quarter, the values from 0.75 to 1 can be either part of the fourth quarter (e.g. all winters, aspect E) or be

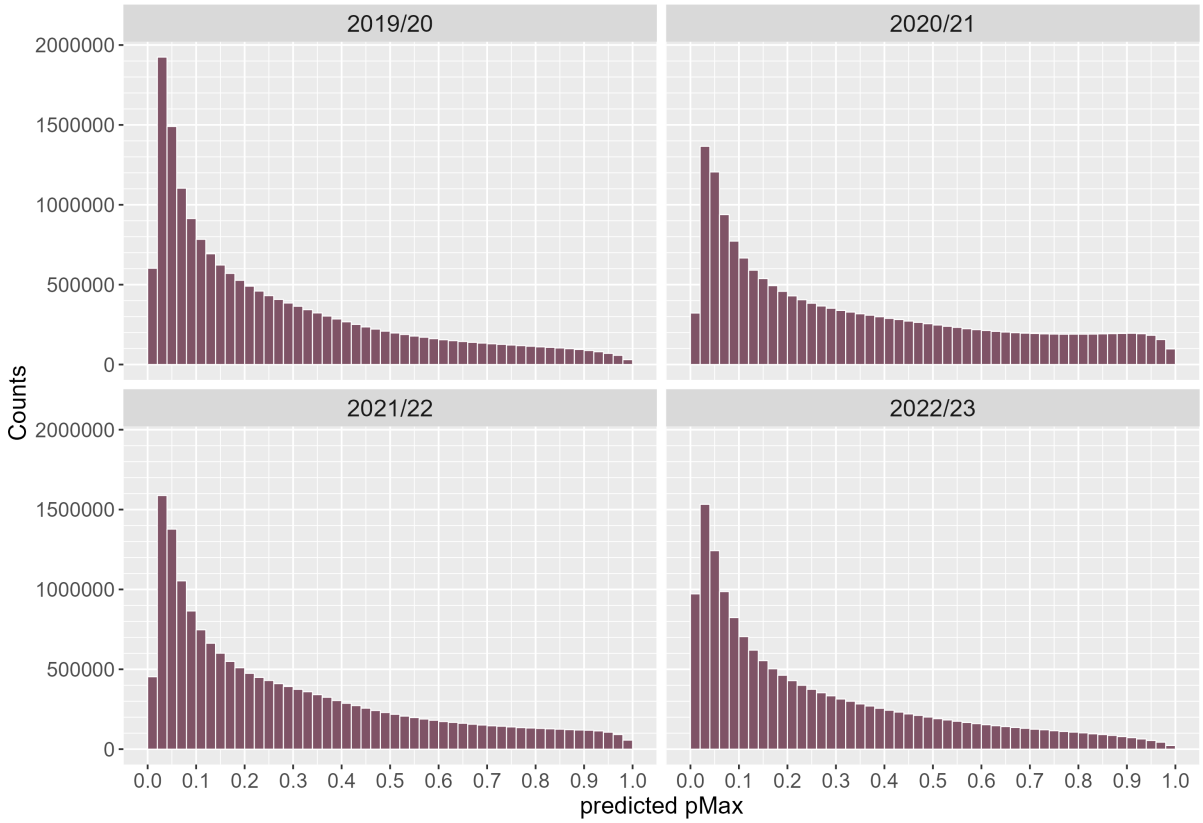


**Figure 5.17:** Histogram of the predicted $\rho_{max}$ value for points in the Swiss Alps (1 km x 1 km grid) for the four winters.

considered outliers depending on the year and aspect (e.g. in the winter of 2019/2020, there are outliers for aspects S and W) (see Figure 5.19). The third quarter ends below a $\rho_{max}$ value of 0.5 in all the winters except in the winter of 2020/21, which shows a higher variability. It is also the most unstable winter in terms of the highest overall median and the widest interquartile range. However, despite its heavy tail in the histogram, it does not contain outliers as opposed to the other winters. The most stable winters, i.e. the ones having the lowest median $\rho_{max}$ over all aspects, are the first (2019/20) and last winter (2022/23).

### 5.5.2 Qualitative Description based on Interpolation Maps

For each winter, information from the interpolation map per month and aspect can be discerned. A sample of the maps can be found in Figure 5.20. A web link to all the interpolation maps can be found in the Appendix (A.5). The maps do not only depict a winter but also reveal patterns and peculiarities of the interpolation model. These will be described afterwards based on the findings for all the winters.

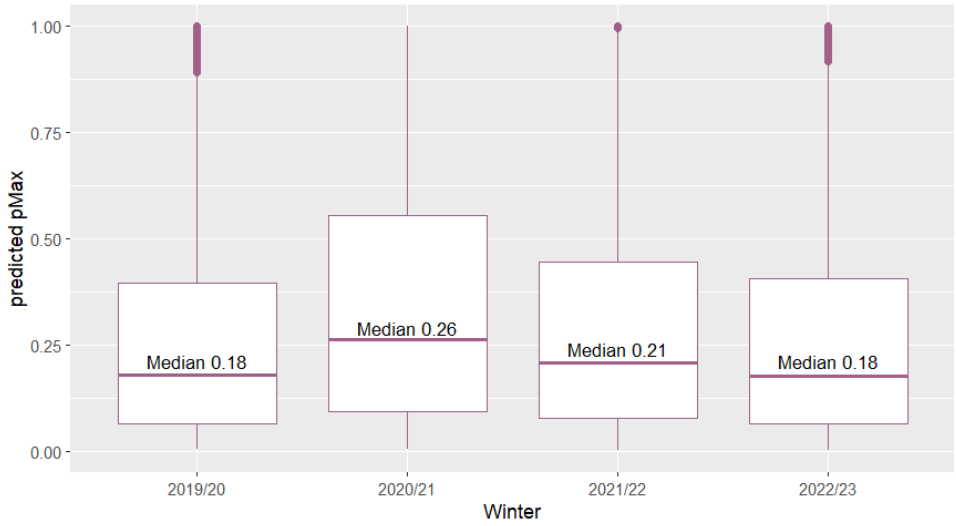


**Figure 5.18:** Boxplot of the predicted $\rho_{max}$ value in the Swiss Alps for the four winters.

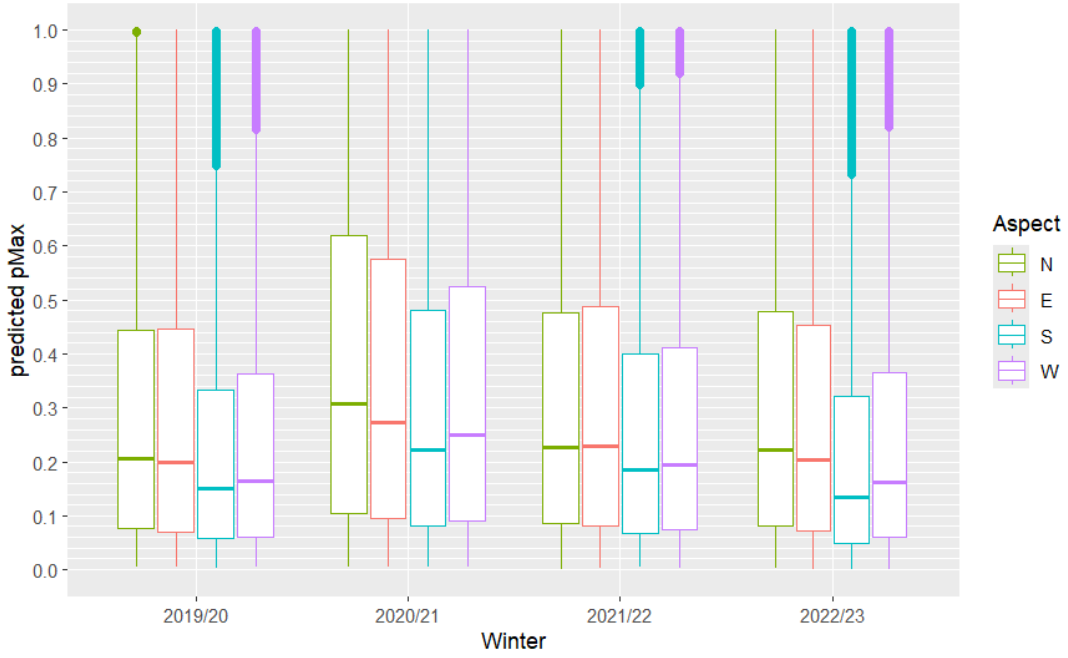


**Figure 5.19:** Boxplot of the predicted $\rho_{max}$ value per aspect for the points in the Swiss Alps for the four winters.

### Winter 2019/20

The interpolation maps show that snowpack instability was high at the beginning of December 2019 for all aspects in Valais and some areas of the Western part of the northern flank. The snowpack is slightly unstable in the Central Part of the northern flank and the Grisons. It is stable towards the Central Plateau and middle and southern Ticino. The situation stabilises more quickly at east- and south-facing slopes until 10 December, when the instability increases again in areas already unstable at the beginning of the month. The instability now seems to be more comprehensive. It stays high until 28 December and then slowly decreases, again quicker

on the east- and south-facing slopes than on the other slopes. The areas around Zermatt and Grindelwald remain unstable throughout December. In January 2020, the instability of all aspects decreases every day until 18 January when it slightly increases and then decreases until 28 January. Again, the increase and decrease are more salient for the aspects north, east and west than for south. At the end of the month, the instability is very high throughout the northern and southern flanks (all parts) and the Grisons. In February 2020, the instability varies slightly: once it increases, once it decreases. The instability hot spots in Zermatt and Grindelwald remain for the aspects north and east. During March 2020, the instability generally decreases for all aspects. While the situation on north-facing slopes seems a bit more unstable, the daily maps for the other aspects are very similar. Throughout April 2020, the snowpack stabilises. There is a slight decrease in stability on some days and at some locations. In the areas around Zermatt and around Grindelwald, instability remains high. The interpolation maps of 1 May 2021 for the aspects east, south and west are quite different, i.e. much more unstable, but also spatially more homogeneous than the maps of the day before for the corresponding aspect. This phenomenon could be explained by the lower number of AWSs serving as input for the interpolation (see Figure 3.3): On 30 April 2020, there were 108 input points for the aspect east, 45 for south and 56 for west. On 1 May 2020, they drop to 79 (east), 18 (south) and 28 (west). The data points for the aspect north also drop from 133 to 104 in the same period, but their number still seems sufficient for the interpolation.

**Winter 2020/21**

In December 2020, instability increases towards the middle of the month at the northern and southern flanks of the Alps (all parts) and in the Grisons. It then slowly decreases and suddenly increases again around Christmas. The aspects south and west stabilise quicker than north and east. At the beginning of January 2021, the instability is still high in Valais, the Bernese Alps, and the Grisons. It decreases until 13 January and stays high throughout the Alps until the end of the month for all aspects. The instability decreases from February until the first days of March 2021, whereas it remains high around Zermatt and Grindelwald. The instability increases again from 8 March on, first around Grindelwald, Zermatt and Martigny (VS), and later in the Grisons and the entire Valais. The maximum instability is reached around the 20 March. After this date, instability decreases again, following the same pattern as before: faster for the aspects south and west than for north and east. April 2021 is characterised by an increase in instability until the middle of the month, followed by a decrease until the end of the month. Again, the areas around Zermatt and Grindelwald remain unstable until 1 May 2021 for the aspect north. The interpolation map of 1 May 2021 is again different for all the aspects, i.e. much coarser than the respective map of the day before due to a drop in the input data for the interpolation (see Figure 3.3).

**Winter 2021/22**

At the beginning of December 2021, instability is already high in some areas in Valais, at the northern flank, in the Grisons, and in the Engadin. Until 12 December, it increases and becomes more comprehensive, to decrease again from 13 December on. Again, the instability at the north- and east-facing slopes changes more slowly than on south- and west-facing slopes. In the last four days of 2021, the instability increases again, especially in Valais and the Western, Central and Eastern parts of the northern flank. In January 2022, the situation stabilises before instability increases again on 8 January. It reaches a maximum around 10 January, then it decreases until the end of the month. Instability is very low for all aspects on 31 January. However, the areas around Grindelwald and Zermatt remain unstable. Instability increases with the change of the month: At the beginning of February 2022, especially the Western and Central parts of the northern flank, as well as the south of Valais, are unstable. Instability varies throughout the month with a clear trend towards lower instability. However, the hot spots remain the same. The stabilisation trend continues throughout March 2022. Only around the middle of the month, the aspects north, east and, to some extent, west show a slight increase in instability in Valais and the Engadin. On 31 March, another increase in instability until the first decade in April 2022 can be noted, especially in Valais. After a decrease, instability increases again on 24 and 25 April at the northern and southern flanks of the Alps. As before, the maps of 1 May 2022 are striking as they are not necessarily lower in instability but more homogeneous, which could be explained by the drop in the number of AWSs (also see Figure 3.3).

**Winter 2022/23**

The last series of interpolation maps begins in mid-December 2022. Instability is already high in Valais, the Western part of the northern flanks and the Grisons. It is higher for the aspects north, east and west than for south. Until the end of 2022, there is first a decrease and then an increase in instability. The range of the variability is higher for the aspects north and east than for south and west. Until 8 January 2023, the instability decreases. Yet, it increases strongly in the days after in Valais, at the northern flank and the Grisons. Towards the end of the month, the instability decreases again, whereas the areas around Zermatt and Grindelwald remain unstable. During February 2023, the instability increases at the northern flank for all aspects in the first decade. It then decreases again. The last days of February show a higher instability, especially for the aspects north, east and west. At the beginning of March 2023, instability remains the same until it increases again on 8 March for the aspects north and east and on the day after for south and west. Until mid-March, the instability remains high, especially for the aspect north. From 17 March on, the instability decreases faster on south- and west-facing than on north- or east-facing slopes. There is another sudden increase for all aspects on 27 March. Throughout April 2023, the instability varies much more for the aspects north and east than for south and west. The change from 30 April to 1 May 2023 is less abrupt as the amount of daily input data is the same throughout this last winter. Until the end of the

data (10 May 2023), we note a stabilisation of the snowpack. Especially the map for the aspect south shows an instability of zero for some days in May for almost the entire Alps. However, on the last day, instability increases again in the areas around Zermatt and Grindelwald for all aspects.

### Findings of the Interpolation Maps

In Figure 5.20, the situation is more stable for the aspect south than north at the start of the four days. But also after the snowfall on 7 February 2022, the situation stabilises faster for the aspect south as the direct heat from the sun stabilises the snowpack in midwinter (McClung et al., 2022). At the same time, north-facing, shady slopes receive little direct heat and lose heat due to long-wave radiation (McClung et al., 2022; Schweizer et al., 2001). West-facing slopes are very exposed to wind in Switzerland as this is the predominant wind direction (Federal Office of

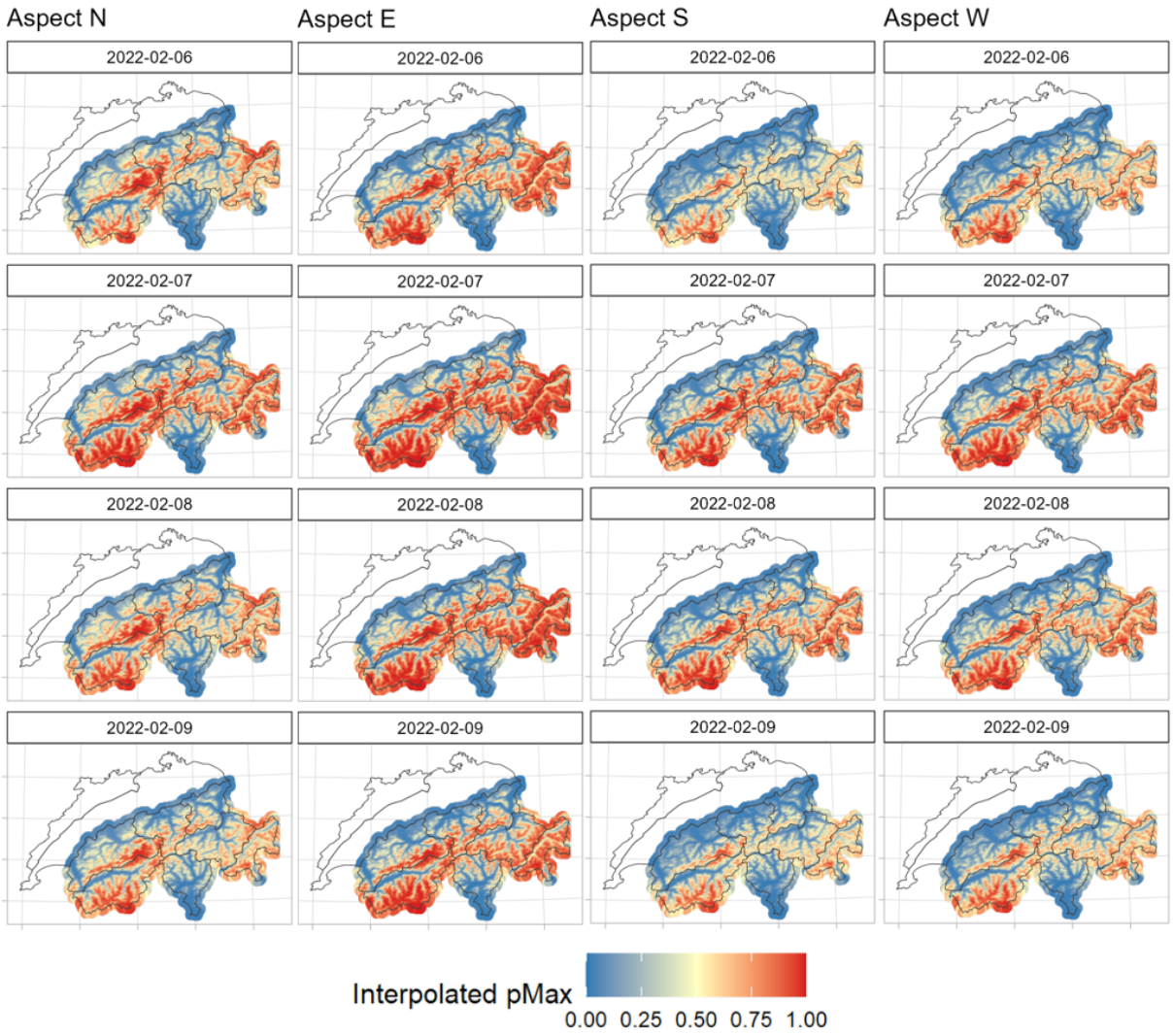


**Figure 5.20:** KED interpolation maps for 6 to 9 February 2022. Low $\rho_{max}$ values stand for a stable snowpack, and high $\rho_{max}$ values for an unstable one.

Meteorology and Climatology MeteoSwiss, 2024), and they can stabilise rather quickly. However, McClung and Schaerer (2022, p. 121) precise: "Wind-exposed slopes are not necessarily safe from avalanches. During calm or periods of light winds, enough snow can accumulate to overload weak layers." Furthermore, we note for Figure 5.20 that the highest instabilities often appear at the highest elevations, e.g. along the Matter and Saas Valley, in the Jungfrau Region and the Engadin (Piz Bernina). Possible reasons are discussed in Chapter 6.

### 5.5.3 Comparison with Avalanche Observations

When comparing the distribution of the $\rho_{max}$ values of the Swiss Alps (Figure 5.18) with the one of the avalanche observations (Figure 5.7), we see that the interquartile range of the two data sets does not overlap: The third quarter of the Swiss Alps $\rho_{max}$ value ends between 0.4 and 0.56. In contrast, the second quarter of the avalanche observations begins at 0.6. Additionally, the differences between the winters are more prominent than those in the avalanche observations. The winter 202/21 stands out in both boxplots, having a higher median. Furthermore, the interquartile range covers higher values. There is also a correspondence between the two data sets for the other winters: The second quarter of winter 2019/20 starts at the same $\rho_{max}$ values as the winters 2021/22 and 2022/23, but its third quarter ends earlier than in the other two years. The third quarter of the winter 2022/23 ends at a lower $\rho_{max}$ value than the third quarter of the winter 2021/22. This pattern is the same for the Swiss Alps as for the avalanche observations.

When comparing the histograms of the points in the Swiss Alps with the avalanche observations, we note that the skewness changes from right in the Swiss Alps to left for the avalanche observations. There is a correspondence between high and low $\rho_{max}$ values and the number of observed avalanches: In the winter of 2020/21, there are more high $\rho_{max}$ values in the Swiss Alps and also more avalanches were observed than in the other winters, whereas in the winter of 2019/20, the most very low $\rho_{max}$ values and the fewest avalanches were observed.

### 5.5.4 Comparison with GPS Points (ARPD)

When comparing the $\rho_{max}$ histogram of the points in the Swiss Alps with the one of the GPS points, we observe the same skewness. In the case of the Swiss Alps, however, the skewness is much more extreme as the increase is higher for very low $\rho_{max}$ values, and the decrease follows much faster. The maximum is reached at different $\rho_{max}$ values: 0.02-0.04 for the Swiss Alps and 0.22-0.24 (2019/20), respectively, 0.24-0.26 (2020/21) for the GPS points. The maximum and median are higher for the GPS points (median of 0.34 and 0.35) than for the Swiss Alps (median of 0.18 and 0.26). This shift to higher $\rho_{max}$ values (maximum and median) could be attributed to filtering the GPS point data according to the terrain indicator and the slope angle. Additionally, skiers might seek a certain steepness when descending.

While the boxplots for the GPS points hardly change from winter 2019/20 to 2020/21, there is a clear difference between the two boxplots for the Swiss Alps. This difference could indicate that despite different winter conditions, the general behaviour of humans only slightly changes. This difference is also visible in the boxplots per winter and aspect (see Figures 5.16 and 5.19). The latter further shows that for both data sets, there is a tendency for higher $\rho_{max}$ values for the aspects north and east and lower $\rho_{max}$ values for south and west (see Section 5.5.2).

## 5.6 Combining the Validation Data

In the histograms in Figures 5.6, 5.15 and 5.17, absolute frequencies were plotted. To relate the avalanches to the GPS points and the points in the Swiss Alps, the proportions of the three variables were calculated per bin of 0.05. Figure 5.21 shows the proportions, i.e. the counts per variable and bin, divided by all the counts of the corresponding variable. Thanks to this normalisation, a bias due to the different sizes of the data sets can be avoided (Techel et al., 2024). The plot only contains data from the first two winters (2019/20 and 2020/21), as the ARPD was not continued after the winter of 2020/21. The median $\rho_{max}$ values of the avalanches (0.75) and GPS points (0.35) are completely different (see Figure 5.21). We observe that 50% of the avalanches occur at instabilities of 0.75 or higher and 87% at instabilities of 0.5 or higher. By contrast, approximately 73% of the GPS points are in terrain with an instability probability of 0.5 or less, and 95% in 0.75 or less. Thus, most of the people (73%) and the

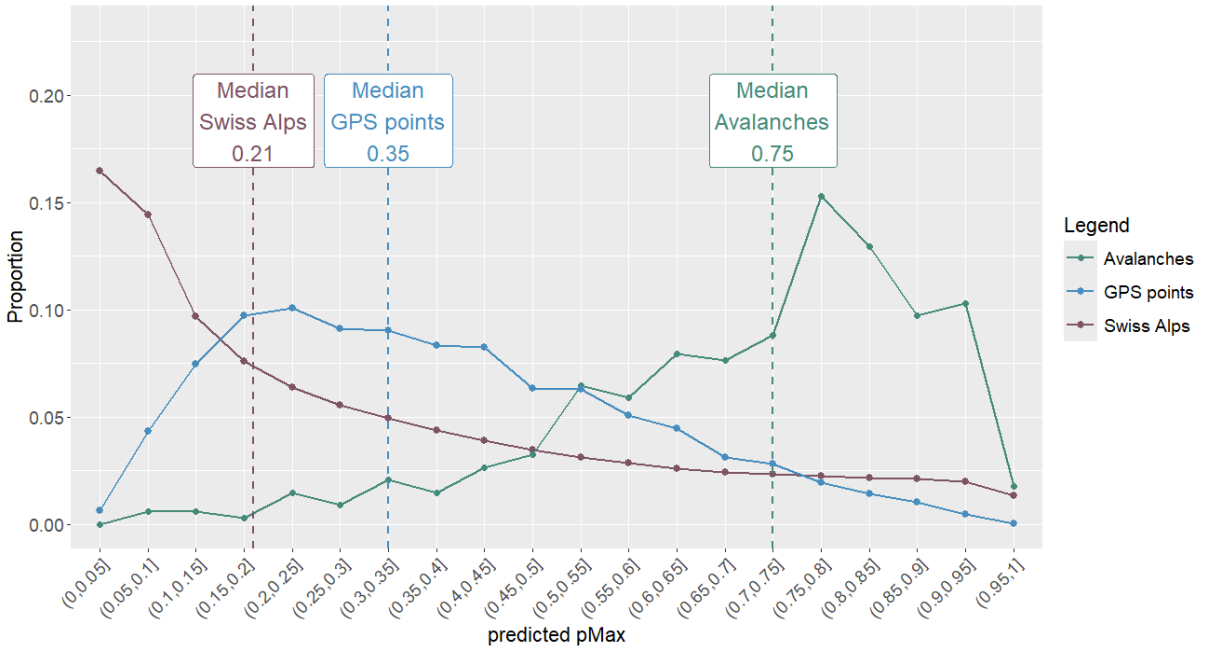


**Figure 5.21:** Proportions of points in the Swiss Alps (purple), GPS points (blue) and avalanche observations (green) for the winters 2019/20 and 2020/21. The proportions are calculated per bin of 0.05.

majority of the avalanches (87%) never meet as people tend to avoid high instabilities during backcountry activities, and avalanches theoretically cannot be triggered at low instabilities. We further observe that the distribution of the avalanches is more concentrated than the one of the GPS points and has a clear peak at a $\rho_{max}$ value of around 0.75.

With 0.21, the median of the Swiss Alps is even lower than the one of the GPS points. Furthermore, 76% of the points on the 1 km x 1 km grid in the Swiss Alps are located in terrain with an instability probability of 0.5 or less, 90% in 0.75 or less. Thus, most of the terrain in the Swiss Alps (averaged over the 1 km x 1 km grid) does not show high instabilities. For very low and low instabilities, there is a discrepancy between the available terrain and what people look for. For high instabilities, there is a discrepancy between the avalanche observations on one side and the available terrain and the GPS points on the other. Thus, human-triggered avalanches are rare since there are not many people out, and there is not much highly unstable terrain in the Swiss Alps.

### 5.6.1 Event Ratios

The discrepancy between avalanche observations and GPS points is further examined with the event ratio $R$ (Equation 4.2), plotted in Figure 5.22. It relates the avalanche observations to human behaviour. The curve can be interpreted as the likelihood of a human triggering an avalanche as a function of $\rho_{max}$. It shows that with increasing $\rho_{max}$ value, the event ratio $R$ increases. Thus, with increasing instability in the snow cover, more avalanches can be triggered and observed. The increase is exponential. The maximum ratio coincides with the highest instability.

Nevertheless, this curve should be interpreted carefully as it only shows a general trend. The number of data points per bin (indicated at the bottom of the points) is low for the first bin, increases strongly, but starts to decrease again after $\rho_{max}$ values of 0.55 because people tend to avoid high instabilities as seen in Figure 5.21. Therefore, the denominator is smaller than for low or medium instabilities. At the same time, the number of avalanches is high up to an instability of 0.95, resulting in a high ratio. The curve is most meaningful where the number of points is high, i.e. at instabilities between 0.15 and 0.65, but there, the likelihood of triggering an avalanche is low. The scale on the y-axis indicates once again how rare human-triggered avalanches are, as the curve does not exceed 0.5. Finally, the avalanches were neither necessarily triggered by the observers nor did avalanches and GPS points spatially overlap.

Human behaviour is less reflected in the event ratio $R$ based on the predicted instabilities in the Swiss Alps according to equation 4.3 (see Figure 5.23). Only the data in the nominator is observed by humans, while the denominator does not have a human component, as the points are based on a grid. The curve of the event ratio $R$ could be interpreted as comparing the avalanche occurrence to a reference distribution. This ratio is calculated with data from the four winters. It diminishes by a factor of approximately 10'000 compared to Figure 5.22. Thus, the scale again indicates how rare avalanches are when considering the actual terrain (Techel

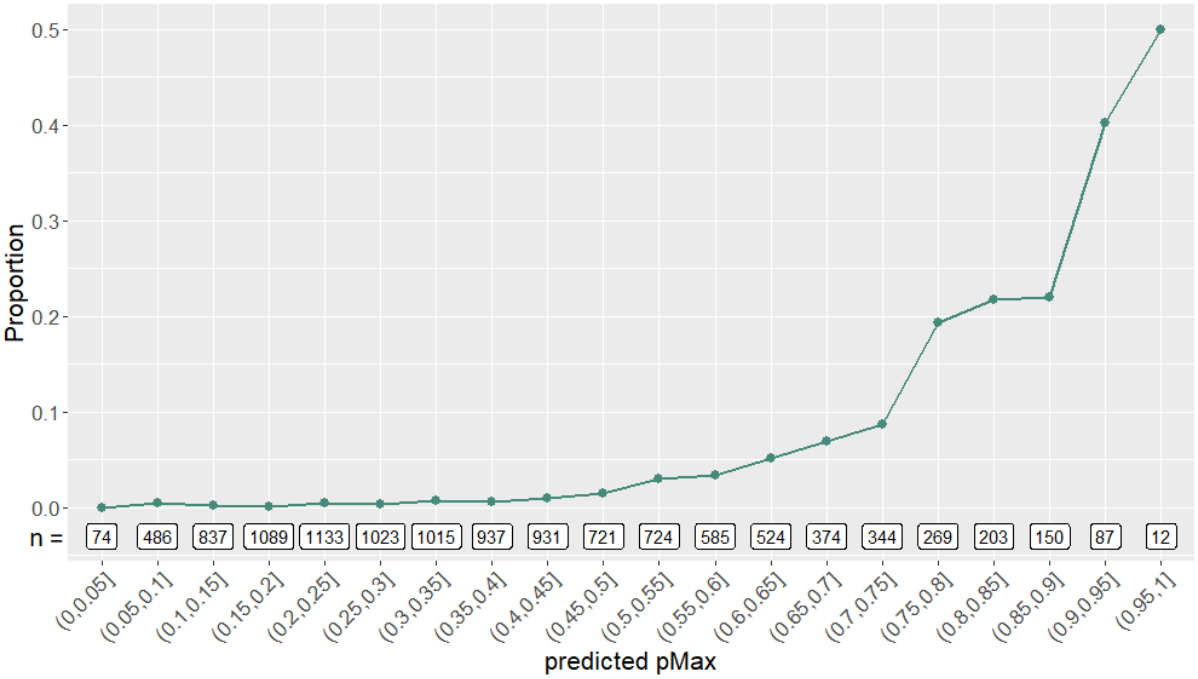


**Figure 5.22:** Proportions of avalanche observations to all prediction points (avalanche observations and GPS points) per bins of 0.05 for the first two winters. The label at the bottom of the points indicates the number of prediction points per bin (denominator).

et al., 2022). The number of data points per bin is highest for the bin with the lowest $\rho_{max}$ values and decreases rapidly, later slowly, until it reaches a minimum at the bin with the highest $\rho_{max}$ value. The increase of the ratio with increasing $\rho_{max}$ values is exponential up to an instability of 0.8, where the ratio reaches its maximum. For higher $\rho_{max}$ values, the ratio is decreasing, respectively, stagnating. Possible reasons for this could be attributed to the topography or the resolution: The terrain is too unstable, respectively too steep for snow to accumulate or for humans to reach and trigger avalanches, which results in a lower nominator and, thus, a lower ratio. Or, due to the coarse resolution of the grid, the instabilities of the points in the Swiss Alps are smoothed, and they mainly span over medium instabilities without touching extreme values. This results in a lower denominator for high instabilities, and the ratio is, therefore, higher.

Both ratios have in common a low number of data points for high instabilities, which results in higher uncertainty. However, the high uncertainty is relativised by the fact that humans hardly access these highly unstable areas (see Figure 5.21).

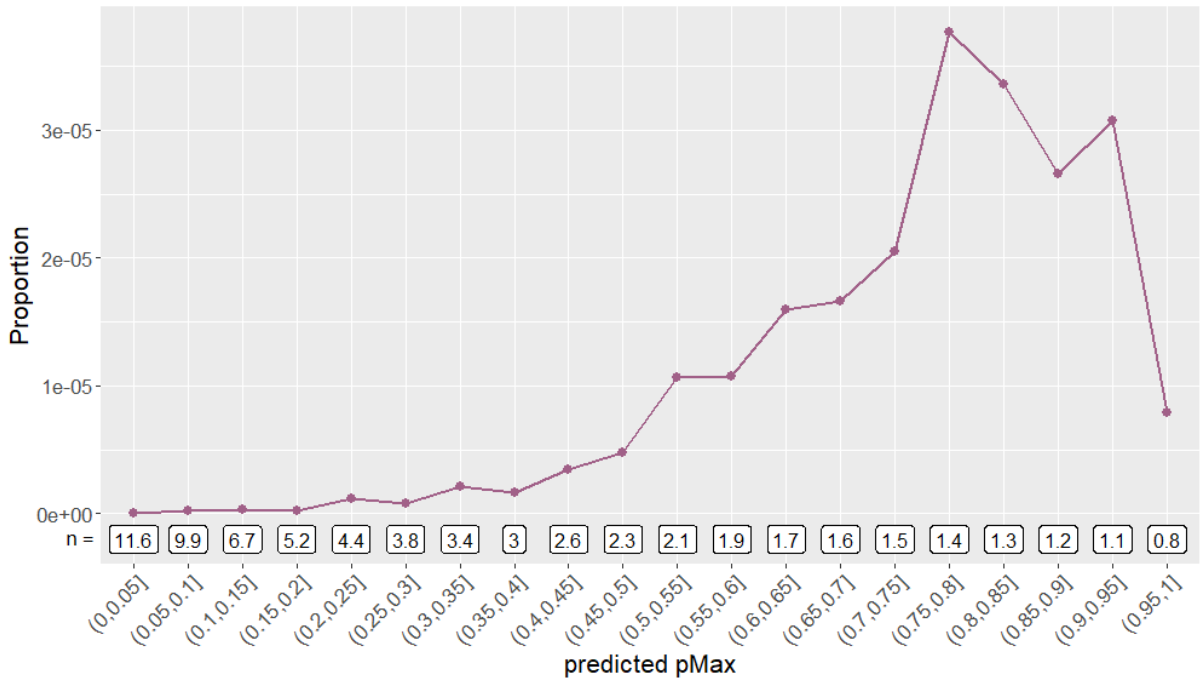


**Figure 5.23:** Proportions of avalanche observations to all the prediction points in the Swiss Alps per bin of 0.05 for all four winters. The label at the bottom of the points indicates the number of prediction points per bin (in millions; denominator).

# 6 | Discussion

In this thesis, I developed and validated an interpolation model for snow instability covering the Swiss Alps. I further tested the model with avalanche observations and GPS points from backcountry activities recorded in the same area. Thus, I addressed the two-fold research gap, i.e. interpolating snow instability at a larger than regional scale and testing the result at the same scale. In the following, I will relate the results to the research questions introduced in Section 1.3, answer them and discuss the limitations of the model, the testing data, and the resulting implications. Finally, I argue to what extent the research gap can now be considered closed. For better readability, the research questions are repeated hereafter. They are answered in the indicated sections.

**Research Questions**

**Part A: Design an interpolation model and validate its performance**

1. How can pointwise, predicted probabilities of instability be interpolated to cover greater areas? Which interpolation methods are suited for this task? What are the challenges and limitations? → **Section 6.1**
2. How can the performance of the model be validated, and how does the model perform? → **Section 6.2**

**Part B: Test the model with external data (avalanche observations, points of backcountry skiing GPS tracks)**

3. How does the model perform when tested with external data? → **Section 6.3**
4. How suitable is the external data for testing high and low probabilities of snow instability? → **Section 6.4**
5. What are the limitations of the testing data and the resulting implications? → **Section 6.5**

## 6.1 Model Design

The first research question concerned the method for interpolating the snowpack instability probability. The following interpolation methods were tested: $k$ nearest neighbours ($knn$), ordinary kriging ($OK$) and kriging with external drift ($KED$). While the first two were assessed only qualitatively with interpolation maps for specific days and aspects and by comparing them to the instability at the AWSs, the latter was also validated quantitatively.

### 6.1.1 Spatial Granularity

As described in Chapter 4, the different methods needed different preparatory steps. For *knn*, the optimal number of neighbours was determined, while for *OK*, the $\rho_{max}$ values had to be logistically transformed. The most complex model in terms of preparation was the one based on *KED*, which followed the approach outlined in Figure 4.2. It turned out that the more elaborate the preparation of a method, the more detailed the resulting interpolation maps.

Figure 6.1 shows that the interpolation maps of *knn* and especially *OK* are very coarse compared to *KED*. *knn* and *OK* cannot adequately represent snow instability in the Alps for different reasons: *knn* assumes that near neighbours are similar. However, weather and snow conditions can vary greatly from one valley to another, even from one slope to the next, due to local factors determining these conditions. *OK* only considers two dimensions (x, y), which is insufficient in mountainous terrain where the elevation varies greatly and influences other phenomena such as temperature, precipitation, and thus the instability of the snowpack.

The *KED* interpolation maps capture the finest granularity: As opposed to *knn* and *OK*, smaller valley bottoms are assigned a lower instability, and the transition from low to high instability is smooth. Compared to the initial description of the four winters (Section 2.4), we note that in general, the daily interpolation maps (see Figure 5.20 and Section A.5) reflect well the major snowfall periods, but also stabilisation processes at different speeds depending on aspect, namely south and west facing slopes stabilising quicker than slopes with aspect north.

### 6.1.2 Number of Stations for Interpolation

Nonetheless, the *KED* interpolation maps reveal some limitations: The transition from 30 April to 1 May in the first three winters illustrates that with fewer stations available for prediction (for the number of available AWSs, see Figure 3.3), the interpolation becomes coarser. The map of 1 May often shows higher instabilities than the one of 30 April without reproducing the usual pattern of areas with high and low instability, e.g. the upper two maps in Figure 6.2. Therefore, I assume that with fewer stations as input, the interpolation becomes coarser, tends to overestimate the instability and is thus less expressive than the maps of the previous days (Maissen et al., 2024). This behaviour further justifies the initial decision to exclude the Jura from the interpolation, as there are not enough stations to produce a reliable interpolation. In the last winter (2022/2023), this deficiency is overcome as the same number of stations is available every day until the end of the season (see Figure 6.2, lower two maps). The instability from 30 April to 1 May 2023 increases due to snowfall (Pielmeier et al., 2024).

The scarcity of AWSs is also noticeable at high elevations: As mentioned in Section 5.5.2, the model often predicts the highest instabilities at the most elevated places in the Swiss Alps, i.e. on the 4000 m peaks in the Matter and Saas valleys, in the Jungfrau Region and around Piz Bernina in the Engadin. As the highest AWS is located at about 3000 m a.s.l. (see Figure 3.4),

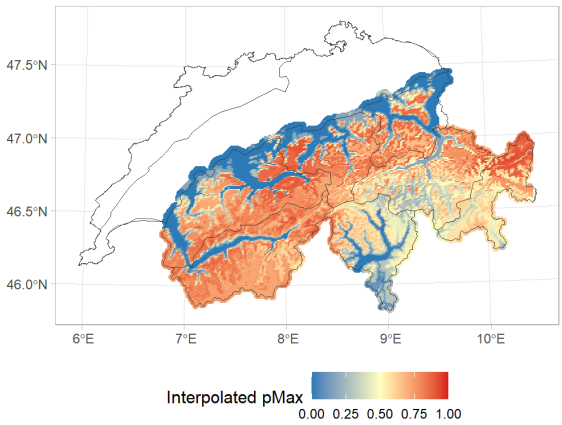


**(a)** $k$ nearest neighbours (*knn*)

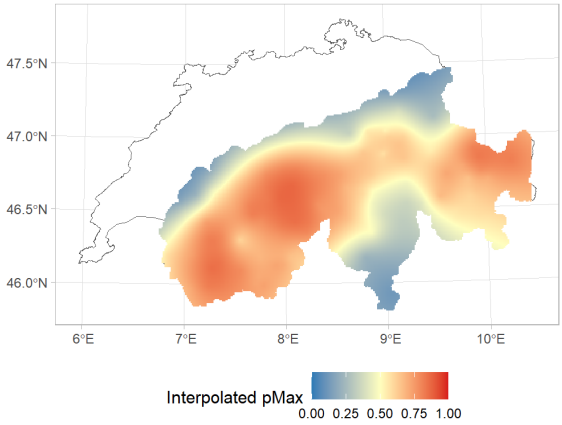


**(b)** Ordinary kriging (*OK*)

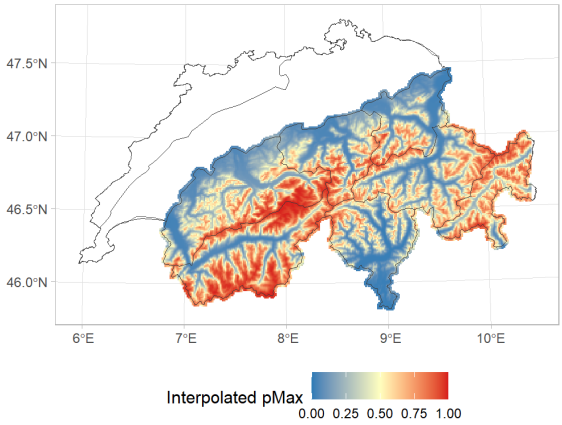


**(c)** Kriging with external drift (*KED*).

**Figure 6.1:** Visual comparison of the interpolation methods for 8 February 2022, aspect N.

there is no input for the interpolation at higher elevations. Thus, above 3000 m, the gradient remains positive without any physical basis, and the model extrapolates (Burrough et al., 2015). This unwanted extrapolation could be avoided by limiting the prediction to a certain elevation or to the $\rho_{max}$ value of the highest AWS.

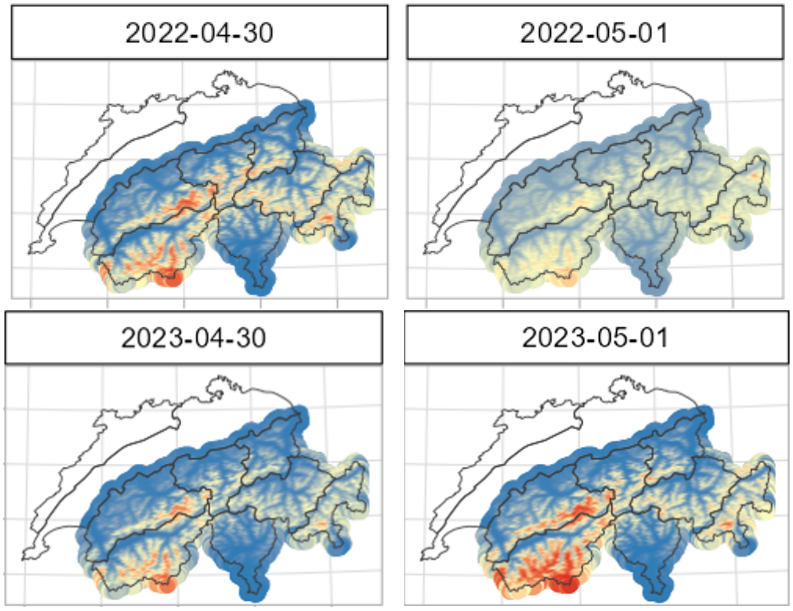


**Figure 6.2:** Transition from 30 April (142 stations) to 1 May (116 stations) in 2022 (figures on top) and 2023 (145 stations on both days; bottom figures), aspect N.

To summarise and answer the first research question, kriging with external drift (*KED*), i.e. with the elevation as an additional variable, is a suitable method to interpolate snow instability from point locations despite some limitations. These are not specific to *KED* but could also concern other interpolation methods. To ensure that the *KED* interpolation values were plausible, the model was validated quantitatively (see Chapter 6.2).

## 6.2 Model Validation

The second research question addressed the model performance. The model was developed based on three samples with a high, medium and low variation in the instability of the snowpack. The idea behind this was to train the model for extreme situations, assuming that it would also be able to deal with more regular situations. The model was validated once in a ten-fold cross-validation with the three samples separately. No distinction was made per aspect. The validation statistics per sample can be found in Figure 5.3. The boxplot in Figure 6.3 combines the validation statistics of the low, medium and high variation samples. It shows a mean error (*ME*) close to 0, a small root mean squared error (*RMSE*) and a high correlation between observed and predicted values.

The model was then validated with all the training data, once in a 90/10 train-test-split and once in a ten-fold cross-validation as described in Section 4.2.2. The cross-validation with the 90/10 train-test split resulted in similar residual histograms for the aspects north, south and west, where the model tends to overestimate the instability (see Figure 5.4). The prediction for the aspect east is better, with a light tendency to overestimate as well (see Figure 5.4, upper right).

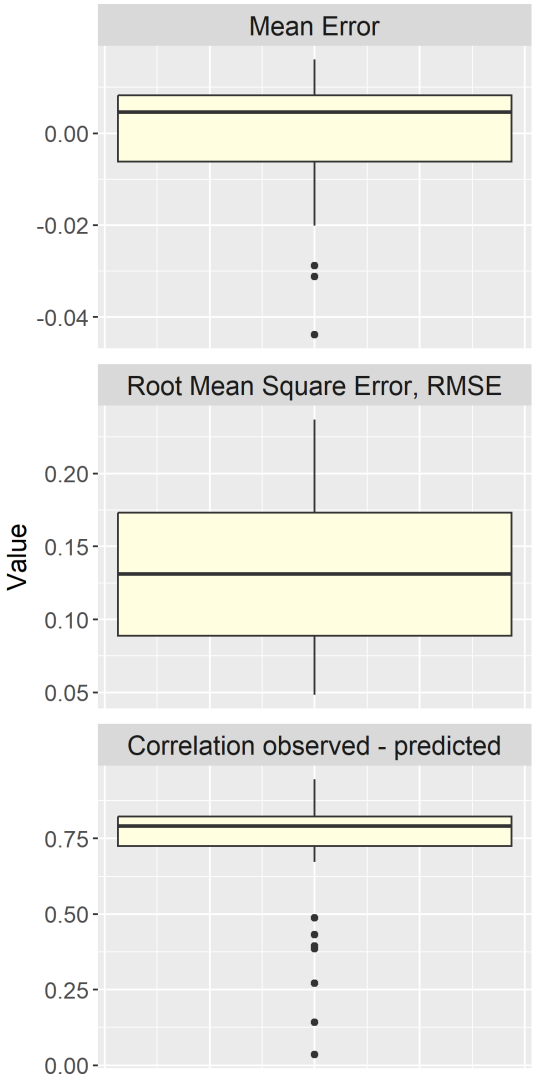


**Figure 6.3:** Boxplot of the ten-fold cross-validation statistics for the spherical model, combining the high, low and medium variation sample.

The ten-fold cross-validation of all the training data showed a high correlation and very small mean error (*ME*) and root mean squared error (*RMSE*) per aspect as shown in Figures 5.5 and A.2. Figure 6.4 shows the combined statistics for all the aspects. When comparing the cross-validation statistics of all the training data (Figure 6.4) with the ones of the three samples (low, medium and high variation; Figure 6.3), we note that the correlation does not decrease and the errors do not increase: The interquartile range remains very similar, but there are more outliers, e.g. for the mean error (*ME*) and the correlation. Hence, the model is robust to the sample used. The very low mean error (*ME*) tells us there is no bias (Holbert, 2024) and the low root mean squared error (*RMSE*) that the interpolation error is very small. To answer the second research question, we note that the model was assessed using different validation methods. The validation statistics are robust and similar for the four aspects. Therefore, I deduce that the model performs well and that the same parameterisation fits all four aspects.

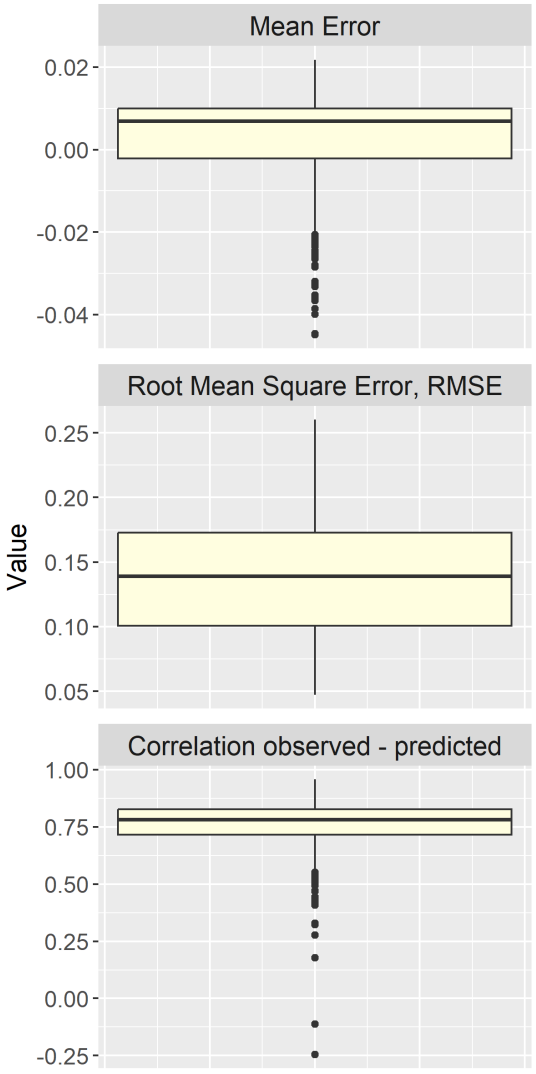


**Figure 6.4:** Boxplot of the cross-validation statistics for the spherical model for all training data.

## 6.3 Testing the Model

The third research question concerned the performance of the model when testing it with external data: As shown in Figure 3.2, the interpolation output, the predicted probability of instability, was compared to avalanche observation and GPS point data, which represent a binary instability probabilities of 1 (unstable) and 0 (stable) respectively.

In Figure 5.21, the proportions of avalanches and GPS points, binned per 0.05 $\rho_{max}$ value, show that the model generally predicts high instability probabilities for avalanches and low probabilities for GPS points. Furthermore, the lower the instability, the more GPS points; the higher the instability, the more avalanches. The latter is even more salient in Figure 5.22, which compares avalanches to GPS points, and in Figure 5.23, which relates avalanches to the natural terrain in the Swiss Alps. In Figure 5.21, the curve of the GPS points rises and falls slowly as backcountry activities follow the terrain that is changing gradually, especially when ascending.

By contrast, human-triggered avalanches occur, e.g. when physical criteria like slope angle, snow height, etc., are met. Thus, this curve shows a steep rise at an instability probability of 0.75, which is in line with the optimal threshold value of 0.77 proposed by Mayer et al. (2022). They classified complete snow profiles in the Swiss Alps with a random forest model as unstable or stable. The model output was compared to a manual assessment of the snow profiles based on an observed stability test and the estimate of local avalanche danger. By comparing contingency tables for different thresholds, they determined the optimal threshold value of 0.77 (Mayer et al., 2022). The smoothness of the curve reflects the number of data points, which is lower for the avalanches, resulting in a more abrupt curve.

To answer the third research question: Most of the predicted instability probabilities for the avalanches and GPS points are reasonable. Thus, the interpolation model generally performs well. However, we noted that the model sometimes predicts low instabilities for avalanches (see Section 5.3.1) and high instabilities for GPS points (see Figure 5.15). Possible reasons as well as specific advantages and characteristics of the two data sets are discussed in the following two Sections (6.4.1 and 6.4.2).

## 6.4 Suitability of the Testing Data

### 6.4.1 Avalanche Observations

In Chapter 3.2, I mentioned that avalanches directly indicate instability (McClung et al., 2022; Techel et al., 2022). The predicted instability probability for the avalanches shows that the higher the instability, the more avalanches are observed (Figure 5.23). However, the maximum number of avalanches does not coincide with the highest predicted instability. Possible explanations are that these highly unstable areas are inaccessible or the terrain is too steep for snow to accumulate. Thus, no avalanche can be triggered.

The median $\rho_{max}$ value of the observed avalanches is between 0.74 and 0.79, depending on the winter (see Figure 5.7). These probabilities seem reasonable as they are not too high; otherwise, nobody could have reached this area and triggered the avalanches. At the same time, they are high enough to be different from the median of the GPS points, which is 0.35 (see Figure 5.21). Furthermore, the median $\rho_{max}$ value of the avalanches is almost congruent with the maximum of the event ratio plot at 0.75-0.8 (see Figure 5.23).

Two additional arguments speak in favour of avalanche observations: They can be triggered at any aspect (see Figure 6.5) and almost any elevation (see Figure 5.8), if the necessary conditions for an avalanche are fulfilled (see Chapter 2). Admittedly, there are fewer avalanches below the tree line, which is between 1650 m and 2450 m a.s.l. in the Swiss Alps (Gehrig-Fasel et al., 2007), as trees or forests can prevent or stop avalanches (Grímsdóttir et al., 2006; McClung et al., 2022).

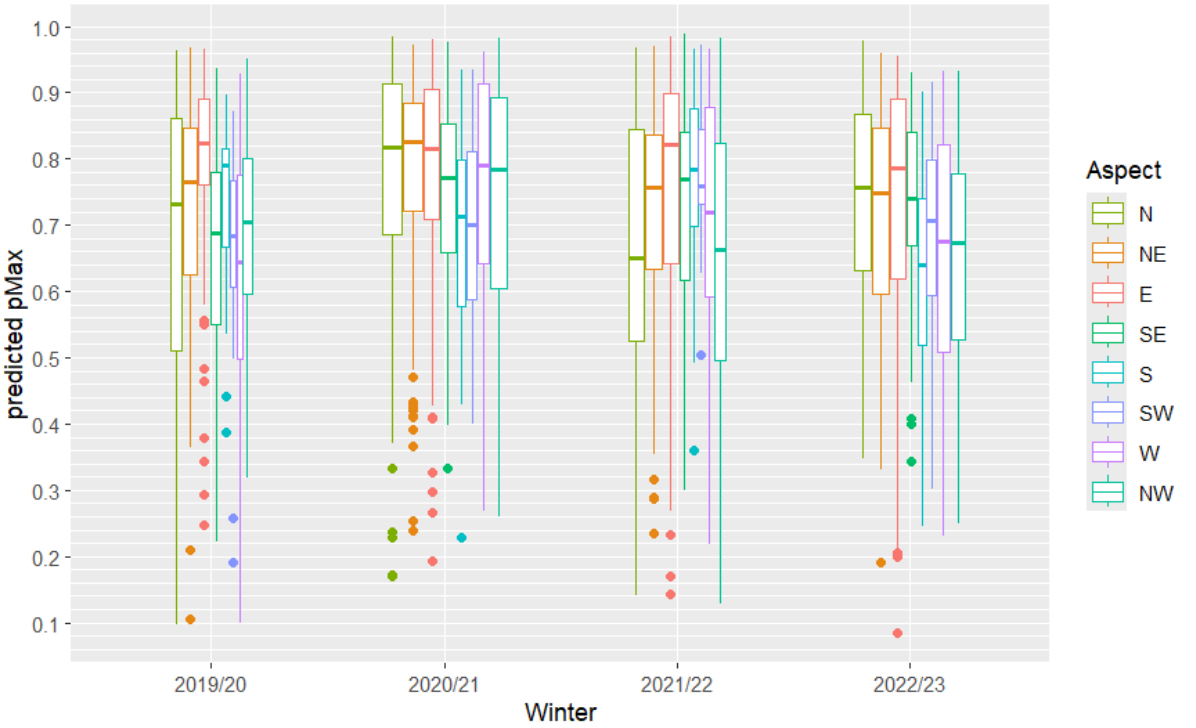


**Figure 6.5:** Boxplot of the aspect of the avalanches, grouped by winter. The width of the boxes is proportional to the square root of the number of observations per aspect.

Finally, avalanches draw attention to locations where the model has difficulties. As mentioned before, for some avalanches, a low instability, thus stable terrain, was predicted (see Figure 5.6). Some of these low instability avalanches occurred in the transition area from the Central Plateau to the Prealps and Alps, where the elevation changes quickly. When testing with the avalanche data, it turned out that the model had difficulties predicting the instability in this transition area. This limitation of the model could be overcome by adding more stations at elevations between 1000 m to 2000 m a.s.l. to the interpolation model input (see Figure 3.4).

A similar effect can be observed towards the eastern border of Switzerland: Stations are relatively scarce. As no stations are further east, the model has difficulties interpolating these areas (see Chapter 5.3). To increase the density, more AWSs from this region could be added to the network by using existing weather stations in this area or Austria or by setting up new AWSs. Another solution would be to limit the extent of the model or to indicate that areas with only a few stations are associated with higher uncertainty.

### 6.4.2 GPS Points (ARPD)

Similar to the avalanches, the GPS points cover all aspects. Their elevation range is even broader than that of the avalanches, starting below 1000 m a.s.l. and reaching over 4000 m a.s.l. As mentioned in Chapter 5.4, the distribution of the predicted $\rho_{max}$ values differs from that of the

avalanche data. The counts decline linearly after a predicted $\rho_{max}$ value of around 0.2. Thus, most backcountry skiers prefer stable terrain.

However, for 5% of the GPS points, an instability probability higher than 0.75 was predicted. As opposed to the avalanches, these GPS points can highlight a limitation of the model, e.g. the model extrapolating the instability probability for a GPS point above 3000 m a.s.l., but they do not necessarily have to (see limitations of the external test data in Section 6.5).

To conclude and answer the fourth research question, avalanche observations and GPS points are suitable for testing the interpolation model despite being strongly influenced by human behaviour. Nevertheless, this influence is known and can thus be considered. Furthermore, the avalanche data revealed some weaknesses in the model setup, which can be addressed in the next version of the model.

## 6.5 Limitations and Implications of the Testing Data

As mentioned, both avalanche data and GPS points reflect human behaviour: where people go, which places they access, how much risk they take, how willing they are to report their activity and events, etc. This behaviour, in turn, has implications for the model testing. To see how the points of the two data sets are distributed, a kernel density estimation (*KDE*) was plotted for each data set and available winter as detailed in Section 4.3.1. The same grid, bandwidth, and kernel type were used to calculate the *KDE*. However, the number of data points varies between the two data sets and between the winters, as listed in Chapter 3. It should be borne in mind that the GPS points and the avalanche observations only represent a small sample: In reality, many more people are outside doing backcountry activities and many more avalanches are triggered. However, only a very small fraction of this activity is captured in our data (Degraeuwe et al., 2024).

Furthermore, the two data sets are linked: For example, more GPS tracks were collected in the winter of 2020/21 than in the other three winters (see Table 3.5). I deduce that in the winter of 2020/21, more people went out, and as a consequence, more avalanches were triggered by humans and recorded (see Table 3.3). The link between the two is also visible in the closeness of the median elevation of avalanches and GPS points: With about 2400 m a.s.l., the median elevation of avalanches (see Figure 5.8) is only slightly higher than the median elevation of the GPS points (2100 m a.s.l., see Figure A.7). Despite being linked, the two data sets are discussed separately regarding their limitations and implications.

### 6.5.1 GPS Points (ARPD)

As mentioned in Section 6.4.2, an instability probability higher than 0.75 was predicted for 5% of the GPS points, which could be explained by reasons inherent to the data instead of the model: A GPS point may not be representative of the area, the person recording the point may have

been close to triggering an avalanche or may have taken measures against the unstable snow cover (e.g. keep a certain distance to other people, ski down the slope one at a time etc.) or the point is located in a busy area (Harvey et al., 2019). Thus, we lack additional but relevant information about the GPS points. Furthermore, an experienced backcountry skier might be able to consider observations in the field and assess the local avalanche danger more accurately than the model. And then, there is another simple reason for a GPS point with a high instability probability: a lucky skier, because human-triggered avalanches are rare (Techel et al., 2022) and not every unstable point triggers an avalanche.

Regarding the distribution of the GPS points (see Figure 6.6), we can see that they are not equally spread over the Swiss Alps. The hot spots are in line with the ones found for the years 2006-2017 (Skitourenguru, 2017). In the winter of 2019/20, the most prominent hot spot is located at the tripoint where the Western part of the northern flanks meets the Central part of the northern and the southern flanks (Goms, Furka, Bedretto). This area received a lot of snow in November and just before Christmas 2019 (Trachsel et al., 2020). The snow heights in the north of Ticino were above the long-term average (ibid.). Furthermore, the area contains different climate regions, one of which usually offers favourable conditions, and the starting points are easily reachable by public transport or car (e.g. Realp or All'Acqua). When looking at the temporal pattern, we can observe that at the beginning of the winter of 2019/20, points were recorded in the Bedretto Valley and towards Furka Pass. In February, March and April 2020, points in the south got scarcer but remained in the north. This could be explained by the dry weather in the south during January and February 2020 and the heavy snowfall at the end of January 2020 at the northern flanks of the Alps (ibid.). The second hot spot, but less salient, in the winter of 2019/20 is located in the Grisons at the border of the Northern and Central Grisons with the Engadin. The snow heights in this area reached or even exceeded the long-term average (1971-2000). Furthermore, the starting points for backcountry activities in this area are at high elevations, which are more favoured in a warm winter like 2019/20, where the snow line varies greatly.

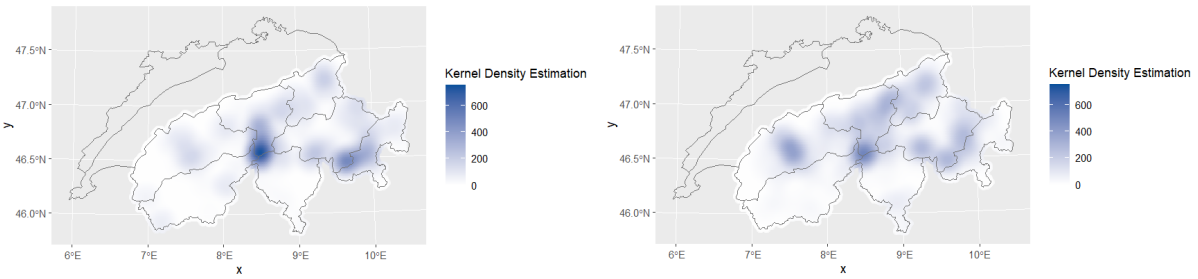


**(a)** Winter 2019/20 **(b)** Winter 2020/21

**Figure 6.6:** Hot spots of the GPS points of the ski touring tracks (based on 1 x 1 km grid, 20 km bandwidth).

The two hot spots from the winter of 2019/20 remain in the following winter but become less pronounced. A hot spot with the same intensity appears in the Western part of the northern flanks. In contrast, less salient hot spots appear at lower elevations, e.g. north of the tripoint (Oberiberg

and Wägital, SZ) and in the Grisons (e.g. around Davos). The points in the second winter are more equally spread than in the first winter. The hot spots are generally congruent with popular backcountry touring regions, e.g. Bedretto, Furka, Engadin, Davos and Iberig/Muotathal SZ.

Nonetheless, there are also more blind spots in the GPS data in the first winter than in the second. They can be found in the Western part of the northern flank (Bernese Alps), Valais and middle and southern Ticino. The blind spots mainly concern the French- and Italian-speaking parts of the Alps. Thus, the blind spots are partly related to culture: The platforms used by the German-speaking community (Gipfelbuch.ch, Bergportal GmbH, 2024; Skitourenguru.ch, Skitourenguru, 2024a) probably provided more data than, e.g. Camp2Camp.org (Camptocamp Association, 2024). In these blind spots, the validation of the low probabilities of snow instability is heavily limited.

### 6.5.2 Avalanche Observations

When looking at the hot spots of the avalanche observations used for the validation of high probabilities of snow instability, we observe that the four winters share similarities and differences: They all have a salient hot spot in the area of Davos, which may not come as a surprise since the SLF is located there. This region has an observer bias since many scientific field experiments are carried out here (Winkler et al., 2021). Unlike the heatmap of the GPS points of 2019/20, the border between the Northern and Central Grisons and the Engadin is not an avalanche observation hot spot. However, in the winters of 2020/21 and 2022/23, more avalanches are observed in this area than in others. Except for the Bedretto Valley, Ticino seems to be a blind spot for avalanches as for the GPS points. Valais, as opposed to the GPS point hot spot, is not a blind spot regarding avalanches: Depending on the winter, quite a few avalanches were observed and reported.

To answer the last research question, I note that avalanche observations and GPS points can be used efficiently to validate high, respectively, low instability probabilities. However, both data sets have blind spots where the validation is spatially limited, and more data is needed for complete validation. Since I am interested in human-triggered avalanches, areas where the GPS point hot spots intersect with the avalanche blind spots and vice versa, are relevant, e.g. the Central part of the northern flank and Valais. As an alternative, other data such as local nowcasts (subjective, local estimate of an observer) and Rutschblock scores could be used for testing the low and high instabilities as it was done by Mayer et al. (2022).

The blind spots do not question the interpolation model as they are not used as model input. They are only partially linked to the model input as AWSs are set up at locations where destructive avalanches can be triggered (WSL Institute for Snow and Avalanche Research SLF, 2023c), thus where people or infrastructure are located.

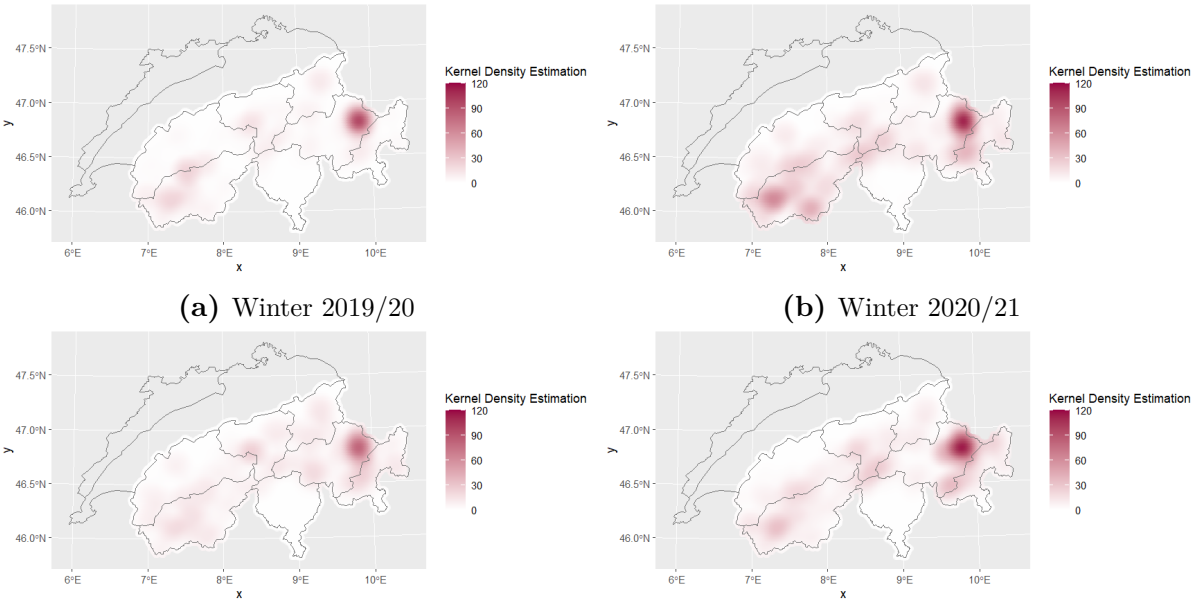


**(a)** Winter 2019/20

**(b)** Winter 2020/21

**(c)** Winter 2021/22

**(d)** Winter 2022/23

**Figure 6.7:** Hot spots of the avalanche observations (based on 1 x 1 km grid, 20 km bandwidth).

# 7 | Conclusions and Further Work

## 7.1 Accomplishments

This thesis tackled the two-fold research gap of interpolating snow instability and testing the model on a larger than regional scale. The model developed for interpolating snow instability in the Swiss Alps on a 1 km x 1 km grid covers an extent larger than a region. The cross-validation showed that the model performs well. The interpolation maps reflected the major snowfall periods. Furthermore, they showed that instability for slope aspects north and east remained longer than for south and west, which is congruent with previous studies (Schweizer et al., 2001).

The testing was done with GPS track points and avalanche observations covering different elevations and aspects. The model generally predicted low instability probabilities for the former and high probabilities for the latter. However, the testing data revealed restrictions regarding space and elevation of the model input data, i.e. the AWSs. As mentioned in Section 6.1, a revised model with additional AWSs at specific locations and elevations could eliminate these restrictions.

In contrast to the interpolation, testing on a supraregional level is more difficult due to the available – or precisely non-existent – data. I can only ensure to cover different geographical regions, elevations, aspects, etc., which I did for the last two (see Figure 5.19). Regarding the coverage of geographical regions, the kernel density estimation revealed blind spots. These blind spots should be analysed further, e.g. whether they contain popular backcountry areas, and addressed accordingly, e.g. by specifically collecting data there. The difficulties I found regarding the testing align with those encountered in previous studies (Reuter et al., 2016; Richter et al., 2021).

I thus conclude that the *KED* model is efficient in the sense that the interpolation model can be run quickly with the available prediction data of the network of AWSs on a 1 km x 1km grid. Additionally, the model is effective as its output provides a reliable spatial overview of snow cover instability that can be consulted in the avalanche forecast process.

## 7.2 Findings

The most important finding is that *KED* interpolation of snow instability works. The output quality of the interpolation model depends on the number and density of available AWSs. A certain number of stations, well distributed at strategic locations covering different elevations and conditions, is needed to reflect the high variation of conditions in the Swiss Alps and produce a solid prediction of the snowpack instability. Furthermore, the model interpolates well as long as there is a physically based input. Outside (or above in terms of elevation), the

model is extrapolating, which results in extreme, somewhat unrealistic values. Despite using the same parametrisation for all aspects, the model is able to capture differences regarding the stabilisation of the snowpack according to aspect. However, the results are not directly transferable to other regions or countries unless there is a well-distributed network of AWSs at which the instability model can be run. As a consequence, the concept and approach should be adapted accordingly.

The model was tested with avalanche observations and GPS points from the Swiss Alps. It was known from the start that humans recorded the data. Therefore, the model focused on instability regarding human-triggered avalanches. Altogether, the testing data was suitable and matched the high, respectively, low instability probabilities. Nevertheless, the spatial distribution of the test data revealed blind spots where the testing was not complete.

## 7.3 Future Directions and Suggestions

Some suggestions for further development have already been mentioned: The model could be revised by capping the instability probability at a specific elevation and adding more AWSs as input to cover the transition area between the Central Plateau and the Prealps. The blind spots in the testing part could be addressed with additional or different data from the four winters or with new data to be collected explicitly for this purpose. It might be worth looking at more than the four winters used as they were all quite warm (see Chapter 2). Even if not all the testing data is available for other winters, the distribution of the predicted $\rho_{max}$ values for an additional winter could still give insights into the model's suitability for more severe winters.

With these corrections and another testing round, the model could be integrated into the operational avalanche forecasting process as follows: The model could be fed once with instability probabilities based on current measurements and once on prognosticated data. The produced nowcast and forecast could be consulted as additional perspectives regarding the overall situation in the Swiss Alps, but also for specific areas where, e.g. observations or other field data are missing. Another suggestion is to expand the model chain over the entire Alps, which would require enough AWSs to cover this extensive area and a close collaboration between the different national avalanche forecasting services.

Lastly, I want to emphasise what the model is not suitable for: It cannot tell whether it is safe to ski a specific slope as it is not designed for such a fine resolution.

# A | Appendix

## A.1 Ten-Fold Cross-Validation (Ste Model)

The following boxplot shows the results of the ten-fold cross-validation on the three samples (with high, medium, and low variation) with the Matérn, M.Stein's parameterisation (Ste) model. The model's parameters were also weighted by the average factors determined by the high variation sample. This model performed slightly worse than the Sph model, so it was not pursued further.

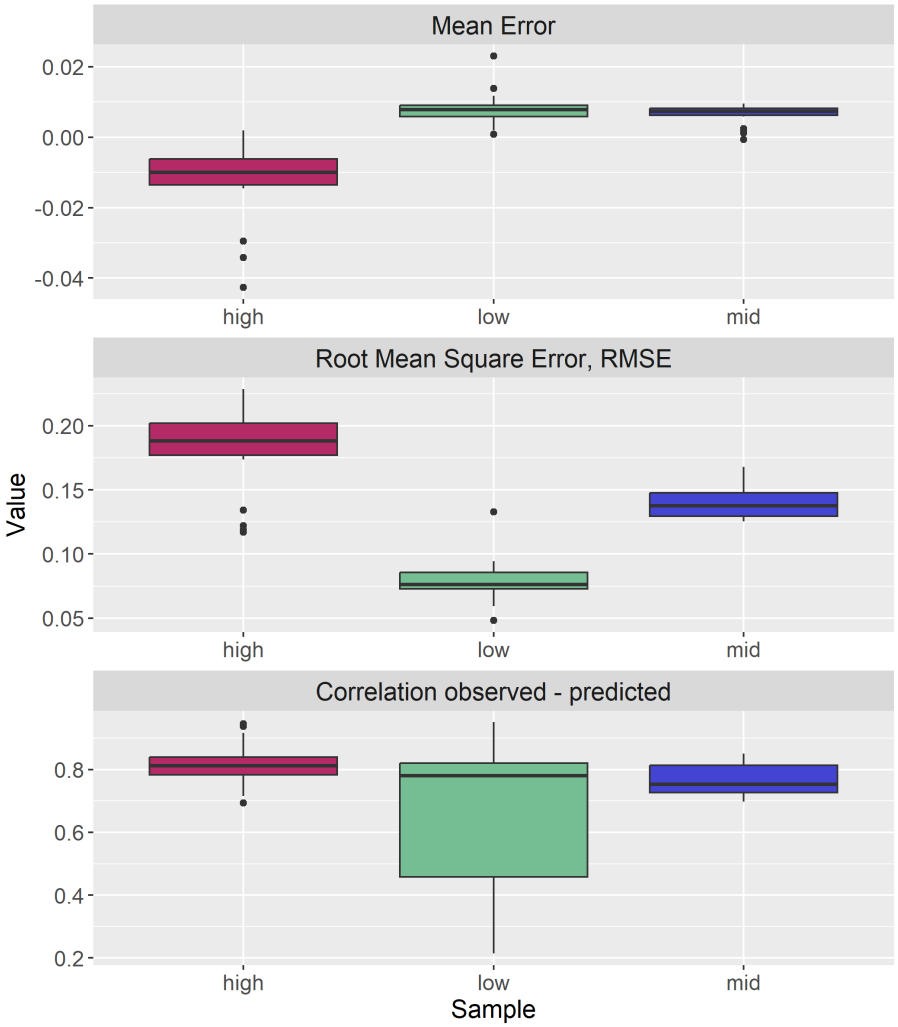


**Figure A.1:** Boxplot of the cross-validation statistics for the Ste model, grouped by sample (low, medium and high variation).

## A.2 Ten-Fold Cross-Validation (Sph Model, all Training Data)

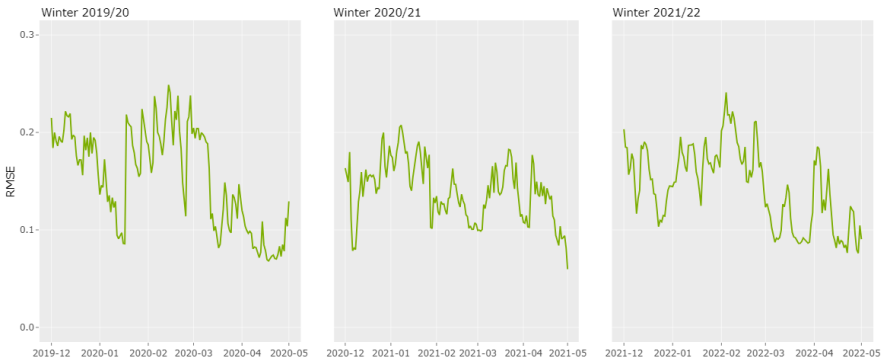


**(a)** North

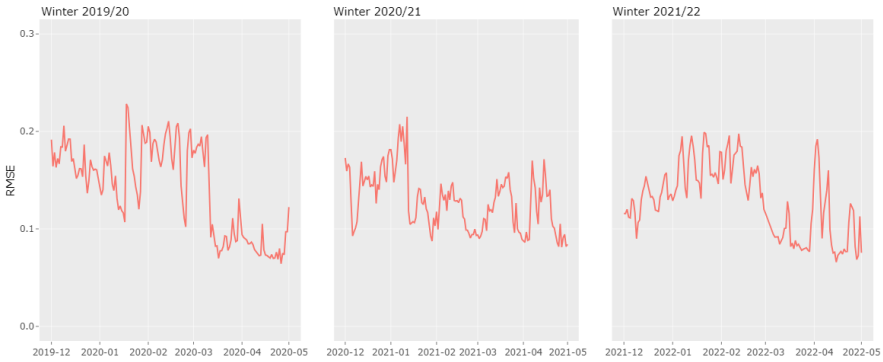


**(b)** East

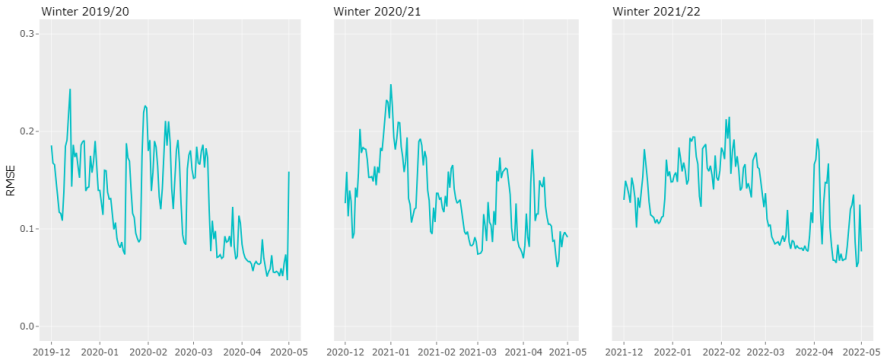


**(c)** South

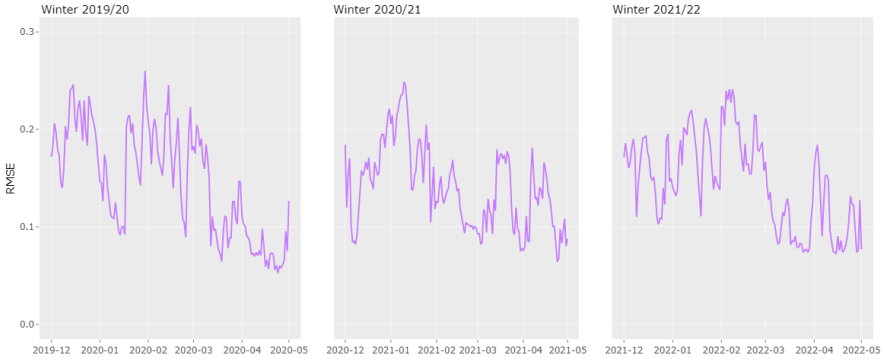


**(d)** West

**Figure A.2:** Root mean squared error (*RMSE*) over time per aspect of all the training data (2019/20-2021/22) in the ten-fold cross-validation.

## A.3 Avalanche Observations

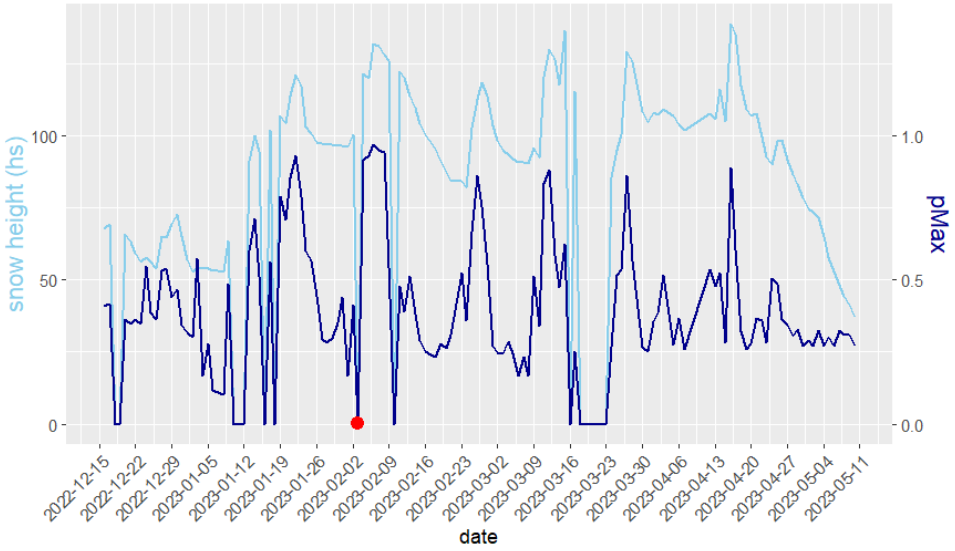


**Figure A.3:** Snow height and pMax value at the station AMD2 in Amden during the winter of 2022/23, aspect E. The red point marks the avalanche date (3 February 2023). This is one of the stations close to the avalanche below Chäserrugg discussed in Section 5.3.1.

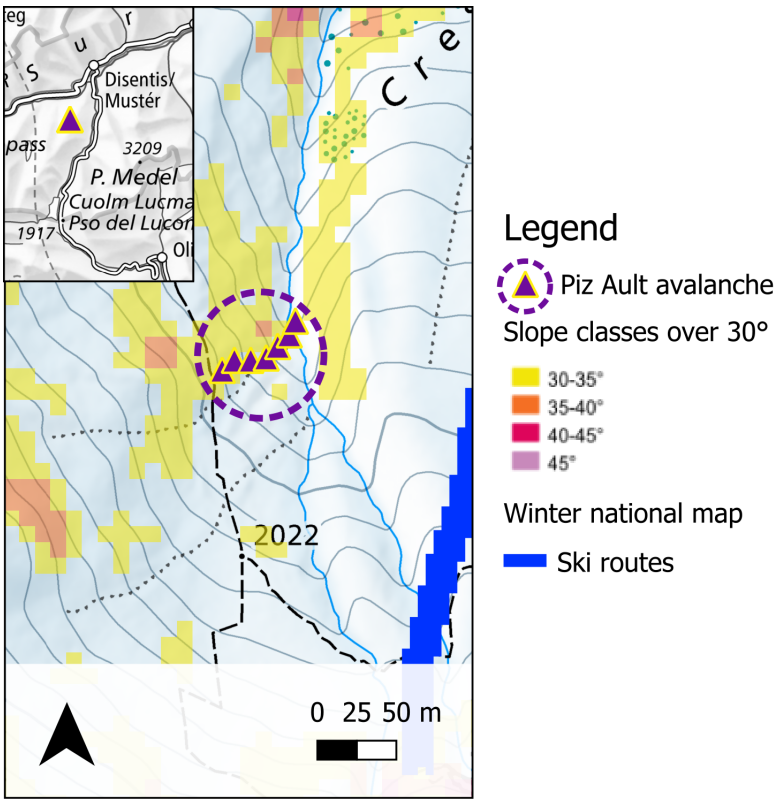


**Figure A.4:** Location of the trajectory of the avalanche below Piz Ault with a low $\rho_{max}$ value in winter 2022/23, aspect NE. The main map also contains the ski routes (blue line) and the slope classes over 30°.

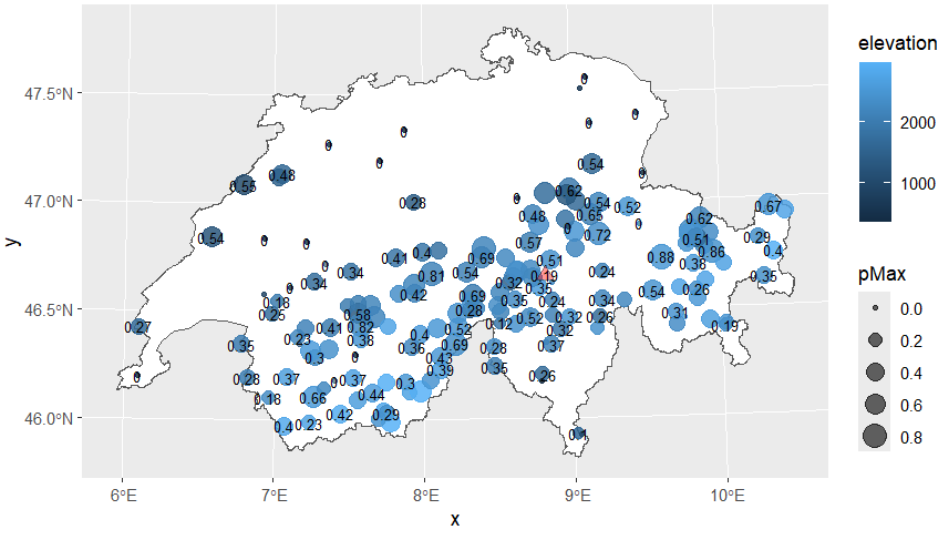


**Figure A.5:** Instability predictions at the locations of the AWSs for 13 February 2023, aspect NE. The red triangle locates the avalanche below Piz Ault.

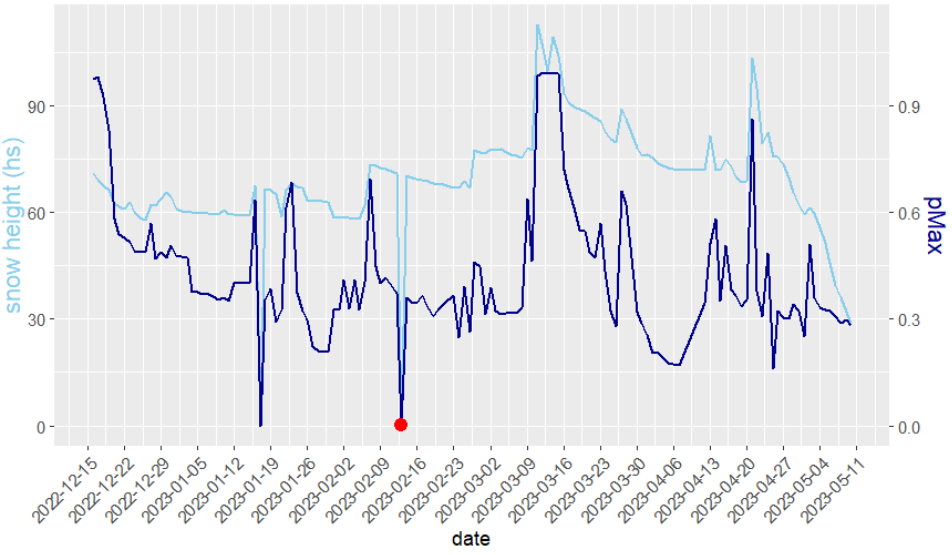


**Figure A.6:** Snow height and pMax value at the station PUZ2 (in Medel Valley) during winter 2022/23, aspect N. The red point marks the avalanche date (13 February 2023). This is one of the stations close to the avalanche on Piz Ault discussed in Section 5.3.1.

## A.4 GPS Points (ARPD)

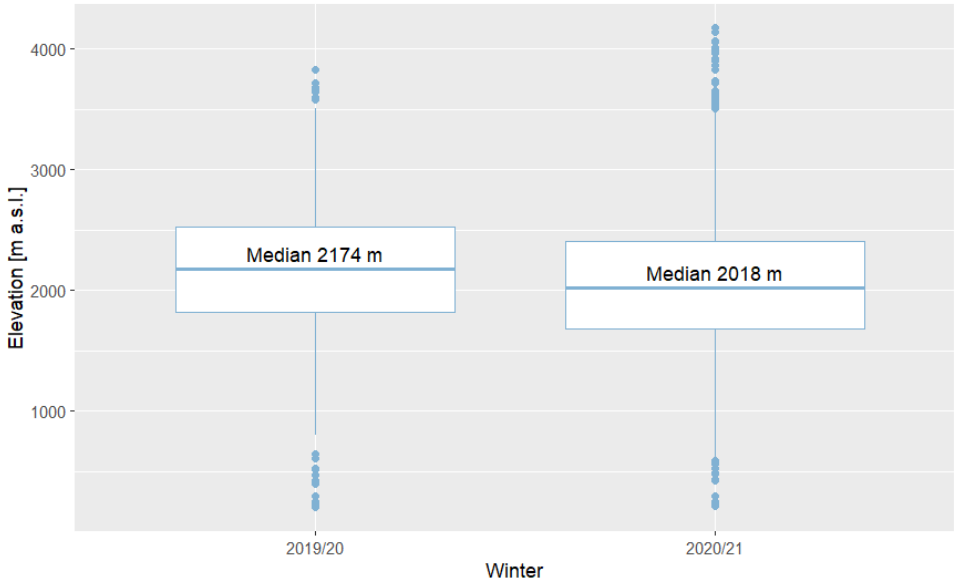


**Figure A.7:** Boxplot of the elevation of the GPS points (terrain indicator ($TI$) $> 0.25$, slope angle $\geq 20°$).

## A.5 Interpolation Maps

The interpolation maps, based on the 1 km x 1 km grid, for each date and aspect (N, E, S, W) for the four winters can be found here: https://tinyurl.com/2dnfktp6

# Bibliography


Badoux, A., N. Andres, F. Techel, and C. Hegg (2016). "Natural hazard fatalities in Switzerland from 1946 to 2015". In: *Natural Hazards and Earth System Sciences* 16.12, pp. 2747–2768. DOI: 10.5194/nhess-16-2747-2016.

Bellaire, S., A. Van Herwijnen, M. Bavay, and J. Schweizer (2018). "Distributed Modelling of Snow Cover Instability at Regional Scale". In: *International Snow Science Workshop*. Innsbruck.

Bergportal GmbH (2024). *Gipfelbuch.ch*. https://www.gipfelbuch.ch (visited on 07/24/2024).

Brun, E., E. Martin, V. Simon, C. Gendre, and C. Coleou (1989). "An energy and mass model of snow cover suitable for operational avalanche forecasting". In: *Journal of Glaciology* 35.121, pp. 333–342. DOI: 10.1017/S0022143000009254.

Brunsdon, C., A. S. Fotheringham, and M. Charlton (11/2002). "Geographically weighted summary statistics - a framework for localised exploratory data analysis". In: *Computers, Environment and Urban Systems* 26.6, pp. 501–524. DOI: 10.1016/S0198-9715(01)00009-6.

Burrough, P.A., R. McDonnell, P. Burrough, R. MacDonnell, and C.D. Lloyd (2015). *Principles of Geographical Information Systems*. eng. Third edition. Oxford: Oxford University Press.

Camptocamp Association (2024). *Camptocamp.org*. https://www.camptocamp.org/articles/106726/fr/camptocamp-association (visited on 07/24/2024).

Chilès, J.-P. and P. Delfiner (2012). "Chapter 3: Kriging". In: *Geostatistics: Modeling Spatial Uncertainty*. 2nd ed. Wiley, pp. 147–237. https://onlinelibrary.wiley.com/doi/book/10.1002/9781118136188.

Degraeuwe, B., G. Schmudlach, K. Winkler, and J. Köhler (05/2024). "SLABS: An improved probabilistic method to assess the avalanche risk on backcountry ski tours". In: *Cold Regions Science and Technology* 221, p. 21. DOI: 10.1016/j.coldregions.2024.104169.

Durand, Y., G. Giraud, E. Brun, L. Mérindol, and E. Martin (1999). "A computer-based system simulating snowpack structures as a tool for regional avalanche forecasting". In: *Journal of Glaciology* 45.151, pp. 469–484. DOI: 10.3189/S0022143000001337.

Federal Department of Foreign Affairs FDFA (2023). *Geography - Facts and Figures*. https://www.eda.admin.ch/aboutswitzerland/en/home/umwelt/geografie/geografie---fakten-und-zahlen.html (visited on 11/14/2023).

Federal Office of Meteorology and Climatology MeteoSwiss (2015). *Typische Wetterlagen im Alpenraum*. Tech. rep. Federal Office of Meteorology and Climatology MeteoSwiss, p. 28.

— (2023). *Measurement values - Automatic weather stations*. https://www.meteoswiss.admin.ch/services-and-publications/applications/measurement-values-and-measuring-networks.html#param=messwerte-lufttemperatur-10min&lang=en (visited on 11/15/2023).

Federal Office of Meteorology and Climatology MeteoSwiss (2024). *The impact of wind*. https://www.meteoswiss.admin.ch/weather/weather-and-climate-from-a-to-z/wind.html (visited on 07/21/2024).

Federal Office of Topography swisstopo (2001). *DHM25 - Matrix Model*. https://www.swisstopo.admin.ch/de/hoehenmodell-dhm25.

— (2016). *Transformation and calculation services*. https://www.swisstopo.admin.ch/en/transformation-calculation-services (visited on 05/17/2024).

— (2019). *Height Model swissALTI3D*. https://www.swisstopo.admin.ch/en/height-model-swissalti3d.

— (2023a). *Ski Routes*. https://www.geocat.ch/geonetwork/srv/ger/catalog.search#/metadata/33090bf2-e8e5-4776-9f64-00d7a6170808.

— (2023b). *Slope classes over 30 degrees*. https://www.geocat.ch/geonetwork/srv/eng/catalog.search#/metadata/77f0637f-8d52-45bc-b824-d6e5719de55b.

Fierz, C. et al. (2009). *The International classification for seasonal snow on the ground*. Tech. rep. Paris: International Association of Cryospheric Sciences, p. 90. https://unesdoc.unesco.org/ark:/48223/pf0000186462.

Gehrig-Fasel, J., A. Guisan, and N.E. Zimmermann (2007). "Tree line shifts in the Swiss Alps: Climate change or land abandonment?" In: *Journal of Vegetation Science* 18.4, pp. 571–582. DOI: 10.1111/j.1654-1103.2007.tb02571.x.

Grekousis, G. (2020). *Spatial Analysis Methods and Practice: Describe – Explore – Explain through GIS*. Cambridge University Press.

Grímsdóttir, H. and D. McClung (2006). "Avalanche Risk During Backcountry Skiing – An Analysis of Risk Factors". In: *Natural Hazards* 39.1, pp. 127–153. DOI: 10.1007/s11069-005-5227-x.

Grünewald, T., Y. Bühler, and M. Lehning (2014). "Elevation dependency of mountain snow depth". In: *Cryosphere* 8.6, pp. 2381–2394. DOI: 10.5194/tc-8-2381-2014.

Harvey, S., H. Rhyner, and J. Schweizer (2019). *Lawinenkunde: Praxiswissen für Einsteiger und Profis zu Gefahren, Risiken und Strategien*. ger. Aktualisierte Neuauflage. Outdoorpraxis. München: Bruckmann.

Heierli, J., P. Gumbsch, and M. Zaiser (2008). "Anticrack Nucleation as Triggering Mechanism for Snow Slab Avalanches". In: *Science* 321.5886, pp. 240–243. DOI: 10.1126/science.1153948.

Hendrick, M. et al. (2023). "Automated prediction of wet-snow avalanche activity in the Swiss Alps". In: *Journal of Glaciology* 50 (1), pp. 1–14. DOI: 10.1017/jog.2023.24.

Hengl, T., G.B.M. Heuvelink, and A. Stein (2003). "Comparison of kriging with external drift and regression-kriging". In: *Technical note, ITC*, p. 17. DOI: 10.1016/S0016-7061(00)00042-2.

Holbert, C. (2024). *Exploratory Spatial Data Analysis and Kriging in R*. https://www.cfholbert.com/blog/esda-kriging/ (visited on 07/11/2024).

Kohavi, R. (1995). "A study of cross-validation and bootstrap for accuracy estimation and model selection". In: *Proceedings of the 14th International Joint Conference on Artificial Intelligence - Volume 2*. IJCAI'95. Montreal, Quebec, Canada: Morgan Kaufmann Publishers Inc., pp. 1137–1143.

Lafaysse, M. et al. (2013). "Toward a new chain of models for avalanche hazard forecasting in French mountain ranges, including low altitude mountains". In: *International Snow Science Workshop, Genoble - Chamonix Mont-Blanc, France*, pp. 162–166. https://arc.lib.montana.edu/snow-science/item.php?id=1741.

Lamprecht, M., R. Bürgi, and H. Stamm (2020). *Sport Schweiz 2020: Sportaktivität und Sportinteresse der Schweizer Bevölkerung*. Tech. rep. Magglingen: Bundesamt für Sport BASPO, p. 64. https://www.baspo.admin.ch/de/sport-schweiz.

Lehning, M., H. Löwe, M. Ryser, and N. Raderschall (07/2008). "Inhomogeneous precipitation distribution and snow transport in steep terrain". In: *Water Resources Research* 44.7. DOI: 10.1029/2007WR006545.

Lehning, M. et al. (1999). "Snowpack model calculations for avalanche warning based upon a new network of weather and snow stations". In: *Cold Regions Science and Technology* 30.1, pp. 145–157. DOI: 10.1016/S0165-232X(99)00022-1.

Li, J. and A.D. Heap (2014). "Spatial interpolation methods applied in the environmental sciences: A review". In: *Environmental Modelling and Software* 53, pp. 173–189. DOI: 10.1016/j.envsoft.2013.12.008.

Maissen, A., F. Techel, and M. Volpi (2024). "A three-stage model pipeline predicting regional avalanche danger in Switzerland (RAvaFcast v1.0.0): a decision-support tool for operational avalanche forecasting". In: *EGUsphere* 2024, pp. 1–34. DOI: 10.5194/egusphere-2023-2948.

Mayer, S., F. Techel, J. Schweizer, and A. Van Herwijnen (2023). "Prediction of natural dry-snow avalanche activity using physics-based snowpack simulations". In: *EGUspere* (April), pp. 1–33. 10.5194/egusphere-2023-646.

Mayer, S., A. Van Herwijnen, F. Techel, and J. Schweizer (2022). "A random forest model to assess snow instability from simulated snow stratigraphy". In: *The Cryosphere* 16.12, pp. 4593–4606. DOI: 10.5194/tc-16-4593-2022.

McClung, D. and P.A. Schaerer (2022). *The avalanche handbook*. 4th edition. Seattle: Mountaineers Books.

Morin, S. et al. (2020). "Application of physical snowpack models in support of operational avalanche hazard forecasting: A status report on current implementations and prospects for the future". In: *Cold Regions Science and Technology* 170 (October 2019), p. 102910. DOI: 10.1016/j.coldregions.2019.102910.

National Centre for Climate Services NCCS (2021). *Pre-Alps: Current climate*. https://www.nccs.admin.ch/nccs/en/home/regions/grossregionen/pre-alps/current-climate.html (visited on 09/09/2024).

National Centre for Meteorological Research (2024). *The SAFRAN-Crocus-MEPRA*. http://www.umr-cnrm.fr/spip.php?article555&lang=en (visited on 09/23/2024).

O'Sullivan, D. and D.J. Unwin (2010). *Geographic Information Analysis: Second Edition*. eng. Ed. by David John Unwin. 2nd ed. Hoboken, N.J: John Wiley & Sons. DOI: 10.1002/9780470549094.

Oliver, M.A. and R. Webster (2014). "A tutorial guide to geostatistics: Computing and modelling variograms and kriging". In: *CATENA* 113, pp. 56–69. DOI: 10.1016/j.catena.2013.09.006.

Parks Canada (2024). *Avalanche terrain ratings - Mountain safety*. https://parks.canada.ca/pn-np/mtn/securiteenmontagne-mountainsafety/avalanche/echelle-ratings (visited on 05/01/2024).

Pérez-Guillén, C. et al. (2022). "Data-driven automated predictions of the avalanche danger level for dry-snow conditions in Switzerland". In: *Natural Hazards and Earth System Sciences* 22 (6), pp. 2031–2056. DOI: 10.5194/nhess-22-2031-2022.

Pielmeier, C., B. Zweifel, F. Techel, C. Marty, and T. Stucki (2023). *Schnee und Lawinen in den Schweizer Alpen: Hydrologisches Jahr 2021/22*. Tech. rep. WSL Institute for Snow and Avalanche Research SLF, p. 72.

Pielmeier, C. et al. (2024). *Schnee und Lawinen in den Schweizer Alpen: Hydrologisches Jahr 2022/23*. Tech. rep. WSL Institute for Snow and Avalanche Research SLF, p. 84. DOI: doi.org/10.55419/wsl:36046.

Purves, R. S., K. W. Morrison, G. Moss, and D. S.B. Wright (11/2003). "Nearest neighbours for avalanche forecasting in Scotland-development, verification and optimisation of a model". In: *Cold Regions Science and Technology* 37.3, pp. 343–355. DOI: 10.1016/S0165-232X(03)00075-2.

R Core Team (2022). *R: A Language and Environment for Statistical Computing*. R Foundation for Statistical Computing. Vienna, Austria. https://www.R-project.org/.

Reuter, B. and S. Bellaire (2018). "On Combining Snow Cover and Snow Instability Modelling". In: *International Snow Science Workshop*. Innsbruck.

Reuter, B., B. Richter, and J. Schweizer (2016). "Snow instability patterns at the scale of a small basin". In: *Journal of Geophysical Research: Earth Surface* 121, pp. 257–282. DOI: 10.1002/2015JF003700.

Richter, B., J. Schweizer, M. W. Rotach, and A. Van Herwijnen (2021). "Modeling spatially distributed snow instability at a regional scale using Alpine3D". In: *Journal of Glaciology* 67.266, pp. 1147–1162. DOI: 10.1017/jog.2021.61.

Rousselot, M., Y. Durand, G. Giraud, L. Merindol, and L. Daniel (2010). "Analysis and forecast of extreme new-snow avalanches: A numerical study of the avalanche cycles of February 1999 in France". In: *Journal of Glaciology* 56.199, pp. 758–770. DOI: 10.3189/002214310794457308.

Schirmer, M., M. Lehning, and J. Schweizer (2009). "Statistical forecasting of regional avalanche danger using simulated snow-cover data". In: *Journal of Glaciology* 55.193, pp. 761–768. DOI: 10.3189/002214309790152429.

Schmudlach, G. (2022). *Avalanche Risk Property Dataset (ARPD) User Manual (V3.1.2)*. https://info.skitourenguru.ch/download/data/ARPD_Manual_3.1.2.pdf.

— (2023). *Avalanche Risk Property Dataset (ARPD)*. https://info.skitourenguru.ch/download/data/ARPD_Manual_3.1.2.pdf.

Schmudlach, G., K. Winkler, and J. Köhler (2018). "Quantitative Risk Reduction Method (QRM), a data-driven avalanche risk estimator". In: *International Snow Science Workshop* 1, pp. 1272–1278. https://www.dora.lib4ri.ch/wsl/islandora/object/wsl%3A18926/.

Schweizer, J. (2008). "On the predictability of snow avalanches". In: *Proceedings Whistler 2008 International Snow Science Workshop September 21-27, 2008*, p. 688.

Schweizer, J., P. Bartelt, and A. Van Herwijnen (2021). "Chapter 12 - Snow avalanches". In: *Snow and Ice-Related Hazards, Risks, and Disasters (Second Edition)*. Ed. by W. Haeberli and C. Whiteman. Second Edition. Hazards and Disasters Series. Elsevier, pp. 377–416. DOI: 10.1016/B978-0-12-817129-5.00001-9.

Schweizer, J. and J.B. Jamieson (2010). "Snowpack tests for assessing snow-slope instability". In: *Annals of Glaciology* 51.54, pp. 187–194. DOI: 10.3189/172756410791386652.

Schweizer, J. and M. Lütschg (2001). "Characteristics of human-triggered avalanches". In: *Cold Regions Science and Technology* 33.2. ISSW 2000:International Snow Science Workshop, pp. 147–162. DOI: 10.1016/S0165-232X(01)00037-4.

Skitourenguru (2017). *Jeder GPS-Track, den du aufnimmst und an Skitourenguru schickst, ist wichtig!* https://info.skitourenguru.ch/index.php/news/148-wo-finden-skitouren-statt (visited on 08/05/2024).

— (2024a). *Skitourenguru.ch*. https://www.skitourenguru.ch/ (visited on 07/24/2024).

— (2024b). *Lawinengefahrenkarte*. https://info.skitourenguru.ch/index.php/lawinengefahrenkarte (visited on 05/01/2024).

Stahel, W.A. (2002). *Statistische Datenanalyse*. 4. Auflage. Wiesbaden: Vieweg+Teubner Verlag. DOI: 10.1007/978-3-322-96962-0.

Statham, G. et al. (2018). "A conceptual model of avalanche hazard". In: *Natural Hazards* 90.2, pp. 663–691. DOI: 10.1007/s11069-017-3070-5.

Techel, F., S. Mayer, C. Pérez-Guillén, G. Schmudlach, and K. Winkler (2022). "On the correlation between a sub-level qualifier refining the danger level with observations and models relating to the contributing factors of avalanche danger". In: *Natural Hazards and Earth System Sciences* 22.6, pp. 1911–1930. DOI: 10.5194/nhess-22-1911-2022.

Techel, F. et al. (2018). "Spatial consistency and bias in avalanche forecasts – a case study in the European Alps". In: *Natural Hazards and Earth System Sciences* 18.10, pp. 2697–2716. DOI: 10.5194/nhess-18-2697-2018.

Techel, F. et al. (2024). "Human vs machine - Comparing model predictions and human forecasts of avalanche danger and snow instability in the Swiss Alps". In: *2024 International Snow Science Workshop*, In Prep.

Tobler, W.R. (1970). "A Computer Movie Simulating Urban Growth in the Detroit Region". In: *Economic Geography* 46, pp. 234–240. http://www.jstor.org/stable/143141 (visited on 07/08/2024).

Trachsel, J., B. Zweifel, F. Techel, C. Marty, and T. Stucki (2020). *Schnee und Lawinen in den Schweizer Alpen: Hydrologisches Jahr 2019/20*. Tech. rep. WSL Institute for Snow and Avalanche Research SLF, p. 76. http://e-collection.ethbib.ethz.ch/view/eth:20002?q=winterbericht.

Van Herwijnen, A. et al. (2023). "Data-Driven Models Used in Operational Avalanche Forecasting in Switzerland". In: *International Snow Science Workshop, 8-13 Oct 2023*. https://www.researchgate.net/publication/374530389.

Venables, W.N. and B.D. Ripley (2002). *Modern Applied Statistics with S*. 4th ed. Springer.

Vionnet, V. et al. (2012). "The detailed snowpack scheme Crocus and its implementation in SURFEX v7.2". In: *Geoscientific Model Development* 5.3, pp. 773–791. DOI: 10.5194/gmd-5-773-2012.

Webster, R. and M.A. Oliver (2007). *Geostatistics for Environmental Scientists*. 2nd ed. John Wiley and Sons. DOI: 10.1002/9780470517277.

Winkler, K., G. Schmudlach, B. Degraeuwe, and F. Techel (2021). "On the correlation between the forecast avalanche danger and avalanche risk taken by backcountry skiers in Switzerland". In: *Cold Regions Science and Technology* 188, p. 103299. DOI: 10.1016/j.coldregions.2021.103299.

World Meteorological Organization (WMO) (2017). *Blowing Snow*. https://cloudatlas.wmo.int/en/blowing-snow.html (visited on 09/05/2024).

WSL Institute for Snow and Avalanche Research SLF (2020). *Wochenbericht 10. - 16. Januar 2020*. https://www.slf.ch/de/lawinenbulletin-und-schneesituation/avablog/2019/20/wochenbericht-10-16-januar-2020/ (visited on 09/11/2024).

— (2023a). *Avalanche accidents in Switzerland since 1970/71*. DOI: 10.16904/envidat.411. (Visited on 11/14/2023).

— (2023b). *Avalanche Terrain Maps*. https://content.whiterisk.ch/en/help/maps/avalanche-terrain-maps (visited on 11/14/2023).

— (2023c). *Intercantonal Measurement and Information System IMIS*. DOI: 10.16904/envidat.406. (Visited on 11/14/2023).

— (2023d). *Long-term statistics*. https://www.slf.ch/en/avalanches/destructive-avalanches-and-avalanche-accidents/long-term-statistics/ (visited on 11/14/2023).

— (2024a). *Division into regions*. https://www.slf.ch/en/avalanche-bulletin-and-snow-situation/about-the-avalanche-bulletin/division-into-regions/ (visited on 07/26/2024).

— (2024b). *Observations*. https://www.slf.ch/en/en-lokale-datensatzsammlung/en-inhalt-sommerbulletin/observations/ (visited on 07/26/2024).

— (2024c). *Additional load*. DOI: 10.1007/978-3-642-41714-6_10549. (Visited on 07/29/2024).

Zhang, G. and A.-X. Zhu (2018). "The representativeness and spatial bias of volunteered geographic information: a review". In: *Annals of GIS* 24.3, pp. 151–162. DOI: 10.1080/19475683.2018.1501607.

Zweifel, B., C. Pielmeier, F. Techel, C. Marty, and T. Stucki (2021). *Schnee und Lawinen in den Schweizer Alpen: Hydrologisches Jahr 2020/21*. Tech. rep. WSL Institute for Snow and Avalanche Research SLF, p. 108. http://e-collection.ethbib.ethz.ch/view/eth:20002?q=winterbericht.

# Personal declaration

Personal declaration: I hereby declare that the submitted thesis is the result of my own, independent work. All external sources are explicitly acknowledged in the thesis.

Zurich, 25 September 2024 Katia Soland